

AR-010-444

Ionospheric Effects on Global
Positioning System Receivers

Mark F. Knight, Anthony Finn and
Manuel Cervera

DSTO-RR-0121

] APPROVED FOR PUBLIC RELEASE

© Commonwealth of Australia

DTIC QUALITY INSPECTED 3

DEPARTMENT OF DEFENCE
DEFENCE SCIENCE AND TECHNOLOGY ORGANISATION

Ionospheric Effects on Global Positioning System Receivers

Mark F. Knight

Anthony Finn

**Tactical Surveillance Systems Division
Electronics and Surveillance Research Laboratory**

Manuel Cervera

**Wide Area Surveillance Division
Electronics and Surveillance Research Laboratory**

DSTO-RR-0121

ABSTRACT

This report presents the results of a study conducted under tasks ADL 94/373 and ADA 96/005 into the effects of the ionosphere on Global Positioning System (GPS) receivers. The report focuses on the effects of the disturbed ionosphere on GPS as this phenomenon has the capacity to degrade the accuracy and reliability of both civilian and military GPS receivers. The impact of ionospheric disturbances on the susceptibility of GPS in a potentially hostile electromagnetic environment is also discussed.

RELEASE LIMITATION

Approved for public release

DTIC QUALITY INSPECTED 3

D E P A R T M E N T O F D E F E N C E

DEFENCE SCIENCE AND TECHNOLOGY ORGANISATION

19980430 154

Published by

*DSTO
Electronics and Surveillance Research Laboratory
PO Box 1500
Salisbury South Australia 5108 Australia*

*Telephone: (08) 8259 5555
Fax: (08) 8259 6567
© Commonwealth of Australia 1998
AR-010-444
February 1998*

APPROVED FOR PUBLIC RELEASE

Ionospheric Effects on Global Positioning System Receivers

Executive Summary (U)

This report presents the results of research conducted under tasks ADL 94/373 and ADA 96/005 into the effects of the ionosphere on NAVSTAR Global Positioning System (GPS) receivers in the Australian area of interest.

GPS will become the primary navigation system for the Australian Defence Organisation (ADO) providing accurate position, velocity and time information globally and continuously. The accuracy available from GPS affords the possibility of enhancing many military operations including enroute navigation, target acquisition, weapons delivery, mine warfare, arms caching, channel navigation and coordinated operations etc. GPS acts as a force multiplier by allowing combined operations to be executed with flexibility and precision through the use of a common reference grid and precise position, velocity and time information. The cost effectiveness, accuracy and reliability of GPS will ensure that it eventually becomes an essential part of most military systems, replacing existing, more costly navigation systems.

A factor which has the potential to significantly degrade the accuracy and reliability of GPS is the distortion of the satellite signals as they propagate through the ionosphere. The effects of ionospheric distortion include the introduction of biases and additional noise into measurements of satellite range as well as difficulties in acquiring and maintaining lock on the GPS signals. All of these effects translate into poorer navigational accuracy for the GPS user.

Ionospheric effects can be broadly divided into benign effects and disturbed effects. Benign effects are associated with the undisturbed or background ionosphere and result in errors in the measurement of satellite range. Historically, the benign ionosphere has only been of concern to stand alone, single frequency GPS users. The residual bias after application of the GPS ionospheric delay model was often the largest source of range error for such users. However, with the advent of continuous Selective Availability errors (SA¹) in the early 1990s, the importance of the residual ionospheric bias for single frequency users has been substantially reduced. In addition, techniques such as Differential GPS (DGPS) and Wide Area DGPS have allowed appropriately equipped single frequency users to significantly reduce the ionospheric range bias. Authorised military users, including the ADO, have access to a second GPS frequency (L2) which allows them to virtually eliminate the ionospheric range error without the need for modelling or differential techniques. Consequently, research into the effects of the benign ionosphere on GPS is considered to be of little value to the ADO, apart from the insight it provides into the large scale behaviour of the disturbed ionosphere. Moreover, with the probable advent of a second civilian frequency (L5), the issue will become of little interest to civilian users also.

¹ SA - Intentional degradation in the accuracy of the civilian service to protect against the hostile use of GPS.

Disturbed ionospheric effects are associated with irregularities in the density of the ionosphere. These irregularities produce fluctuations in the amplitude and phase of the GPS signals as they propagate towards the ground. The fluctuations, also referred to as scintillations, introduce noise into the carrier tracking loops of a receiver resulting in degraded carrier phase DGPS performance and noisier velocity estimates. Under extreme conditions, scintillations can also lead to difficulties in acquiring and tracking the GPS signal, particularly for the carrier tracking loop. As scintillations disrupt GPS receivers at the tracking loop level, they cannot be mitigated through the use of multiple frequencies or by differential techniques. The most effective and straightforward mitigation strategy involves simply avoiding the times and locations for which scintillation activity are most likely to be a problem. Scintillation models such as WBMOD (described below) provide predictions of the occurrence and severity of scintillation activity and are therefore very useful for planning operations in areas which may be affected by scintillations. Another mitigation technique involves the automatic detection of scintillation activity on satellite links and, if appropriate, either ignoring or filtering the measurements derived from those links. Alternatively, if the statistical characteristics of the scintillations can be measured by the receiver, it is possible to optimise the bandwidth and order of the tracking loops to minimise the probability of losing lock. This report, and subsequent research, will look mainly at the first mitigation option involving the prediction of scintillation activity using the WBMOD model. The automatic detection of scintillation activity is being investigated by the University of New South Wales, School of Geodesy under a broader project dealing with quality control of GPS measurements.

Scintillation activity cannot be predicted with certainty. However, it is known to occur predominantly within a band from about 20° South to 20° North of the geomagnetic equator. In the Australian longitude sector, this region extends from about 10° South to 30° North of the geographic equator, and so encompasses most of South East Asia. Scintillations show a strong diurnal dependence, being strongest from sunset to local midnight and virtually absent during daylight hours. They are also heavily dependent on the 11 year sunspot cycle and are likely to be at their worst during the next Solar cycle peak near the year 2000. Predictive scintillation models such as the Wide Band scintillation MODEL (WBMOD) make use of information about location, local time, solar activity and geomagnetic activity to model ionospheric irregularities and determine the effects on individual satellite links. One of the activities being carried out under the ionospheric component of the GPS task is the validation, and (if necessary) modification of the WBMOD model for the South East Asian region. This will involve collecting scintillation data from countries such as Indonesia, Malaysia and Papua New Guinea, which are within the equatorial band.

Scintillations are unlikely to affect all of the satellites in a receiver's field of view simultaneously. They will, however, impact on the accuracy of the resulting navigation solution by degrading the geometry of the available constellation. Consequently, the coverage of both the satellites and the irregularities, as well as the intensity of scintillation activity will all contribute to the accuracy of the final solution. Scintillations models such as WBMOD provide predictions of the performance of the individual satellite links allowing the accuracy of the navigation solution to be determined in advance. Preliminary investigations into the probability of complete

outages (ie when there are insufficient satellites to form a navigation solution) suggest that such events are unlikely within the Australian Area of Interest (AAI), except under extreme conditions.

In this report, the results of tests on a tracking loop simulator using simulated scintillation data are discussed. These tests are designed to determine the effects of different levels of scintillation activity on the performance of a single GPS satellite-receiver link. The scintillation models which produce the simulated data are based on parameters provided by the WBMOD model so the data can be assigned specific probabilities of occurrence based on WBMOD. Simulation results suggest that amplitude scintillations generally have less effect than phase scintillations on the carrier tracking loop, but more effect on the code loop. They also show that the carrier loop is the weakest link in a channel which is affected by scintillations. These results suggest that an increase in the bandwidth of the carrier tracking loop in the presence of strong scintillation activity may help to maintain lock on the GPS signal. Conversely, under medium to weak scintillation activity when the receiver is at low risk of losing lock, carrier phase DGPS may gain an advantage by narrowing its tracking loop bandwidth. This will filter the high frequency fluctuations associated with both the phase scintillations and thermal noise. The code loop, on the other hand, is more susceptible to amplitude scintillations and should maintain a narrow bandwidth under all scintillation conditions. Analytical studies of the performance of tracking loops under phase scintillation conditions also show the relationship between the spectral parameters of the scintillations (which can be linked to the WBMOD model) and the loop's susceptibility to loss of lock.

Another effect of scintillations which is considered to be of significant operational interest to the ADO is the possibility that scintillation activity may increase a receiver's susceptibility to jamming. In an environment in which several satellite links have been weakened by scintillation activity, the jammer power needed to force these links to lose lock will be much less. In the report, equations are developed which associate the levels of scintillation activity in terms of the scintillation spectral parameters with the reduced jamming threshold for a GPS receiver carrier tracking loop.

Authors

Mark F. Knight

Tactical Surveillance Systems Division

Mark Knight graduated in 1986 from the University of Adelaide, Department of Electrical and Electronic Engineering with a bachelor's degree in Electrical and Electronic Engineering. He currently works as an engineer with Sensor Application's discipline of Tactical Surveillance Systems Division where his principal interests are the effects of the ionosphere and electromagnetic interference on GPS system performance.

Anthony Finn

Tactical Surveillance Systems Division

Anthony Finn is a Senior Research Scientist with Tactical Surveillance Systems Division and heads the Satellite Navigation section. Since graduating from Cambridge University with his PhD he has worked in the field of HF radio wave propagation within the ionosphere and navigation systems. His current interests include environmental and electromagnetic effects on GPS system performance.

Manuel Cervera

Wide Area Surveillance Division

Manuel Cervera is a Research Scientist working for the Ionospheric Effects Group of Wide Area Surveillance Division. He graduated with a PhD in field of Meteor Physics in the Atmospheric Physics Group of the Department of Physics and Mathematical Physics at the University of Adelaide in 1996. Since working for the Wide Area Surveillance Division, his interests have included the disturbed ionosphere and its effect on trans-ionospheric radio signals.

Contents

1. INTRODUCTION.....	1
2. OVERVIEW OF GPS	2
3. OVERVIEW OF THE IONOSPHERE	6
4. BENIGN IONOSPHERIC EFFECTS ON GPS	9
4.1 Introduction.....	9
4.2 Single Frequency GPS.....	10
4.3 Wide Area Differential GPS	17
5. DISTURBED IONOSPHERIC EFFECTS ON GPS.....	19
5.1 Introduction.....	19
5.2 Morphology of Scintillations.....	19
5.3 Scintillation Models	22
5.3.1 Fresnel-Kirchoff Diffraction model	23
5.3.2 Wide Band Scintillation Model (WBMOD)	27
5.3.3 Synthetic Scintillation Time Series Model (SSTS).....	29
5.4 Impact of Scintillations on GPS	32
5.4.1 GPS System Simulator	32
5.4.2 Simulation Results	34
5.4.3 Preliminary results from the SSTS model.....	39
5.4.4 Additional Comments	40
5.5 Signal Processing Model	42
5.6 Impact of Scintillations on Jamming Immunity	50
5.7 Impact of Scintillations on Navigational Accuracy.....	54
6. CONCLUSIONS.....	59
7. FUTURE DIRECTIONS.....	60
8. ACKNOWLEDGMENTS	62
9. REFERENCES	63

Appendix A - GPS Dual Frequency Ionospheric Correction	67
Appendix B - Ionospheric Delay at GPS Frequencies	68
Appendix C - GPS Single Frequency Ionospheric Model	71
Appendix D - TEC Estimation	73
Appendix E - Error Sources in GPS TEC Estimates.....	77
Appendix F - Fresnel-Kirchoff Diffraction Model	82
Appendix G - Synthetic Scintillation Time Series Model	85

1. Introduction

The 1994 White Paper "Defending Australia" stresses the importance of surveillance to the defence of Australia. An accurate knowledge of the position of military assets is essential for effective surveillance and navigation, as well as many other Australian Defence Organisation (ADO) operations. The NAVSTAR Global Positioning System (GPS) will be the primary navigation system for the ADO providing users with Position, Velocity and Time (PVT), globally and continuously. The positional accuracy of GPS affords the possibility of enhancing many ADO operations, including navigation, surveillance, logistic support, asset management and the targeting and guidance of weapons.

Two positioning services are available from GPS, the Precise Positioning Service (PPS) and the Standard Positioning Service (SPS). The PPS offers an accuracy of 22m (2σ horizontal error) and is available to authorised users only. Access to the PPS is controlled by the United States Department of Defence (US DoD) through a code encryption process known as Anti-Spoofing (AS). Australia has an agreement with the US which allows the ADO access to the PPS. The SPS is available to all users, civilian and military, who have GPS User Equipment (UE). The accuracy available from the SPS is also controlled by the US DoD and can be varied by a process known as Selective Availability (SA). US DoD policy is to maintain the accuracy of the SPS at no worse than 100m (2σ horizontal error) for the next 5 to 10 years unless the strategic situation dictates otherwise. After this period, SA will be turned off and an SPS accuracy of approximately 42m (2σ horizontal) is anticipated.

A factor that can significantly influence the performance of GPS is the distortion of the satellite signals as they propagate through the ionosphere. The effects of ionospheric distortion include the introduction of biases and additional noise into satellite range measurements as well as difficulties in acquiring and maintaining lock on GPS signals. All of these effects translate into a poorer PVT solution for the GPS user.

PPS receivers are capable of removing the bias component of the ionospheric error by forming a linear combination of the satellite range measurements at the two GPS carrier frequencies. The residual error after application of the dual frequency correction is typically well below errors resulting from other sources (eg the Control segment). SPS receivers, on the other hand, have access to only one frequency and are therefore unable to remove ionospheric biases in this way. Such receivers must rely on a model of the ionosphere which is broadcast as part of the GPS Navigation message in order to reduce the ionospheric bias. However, this single frequency model is only capable of reducing the ionospheric bias by 50% RMS, and can at times leave a large residual error. Both PPS and SPS receivers are, however, susceptible to the additional range measurement noise and tracking difficulties associated with disturbed ionospheric conditions. Problems associated with the disturbed ionosphere are inherent within the GPS receiver tracking loops and cannot be eliminated by either modelling or the use of multiple carrier frequencies.

The purpose of this report is two-fold: (i) to provide an overview of the effects of the benign ionosphere on GPS and, (ii) to provide an understanding of the effects of disturbed ionospheric conditions on GPS performance. A follow-on report to be provided by Wide Area Surveillance Division (WASD) will cover the nature, temporal and spatial distribution of ionospheric disturbances and their impact on the GPS signal. In this report, particular emphasis is given to the equatorial ionosphere over the regions of Northern Australia and South East Asia. This is an area of significant operational interest to the ADO as well as an area where ionospheric disturbances and large electron density gradients are most likely to occur.

2. Overview of GPS

GPS is a satellite based navigation system that is capable of providing 24 hour worldwide coverage under all weather conditions. 3D position, velocity and time estimates are obtained from four independent time delay range and delta-range measurements to four satellites in view. The four range measurement equations can be represented as follows:

$$\left| [x_{Si}, y_{Si}, z_{Si}] - [x_R, y_R, z_R] \right| = \rho_i + C_b \quad \text{for } i=1 \text{ to } 4,$$

where $[x_{Si}, y_{Si}, z_{Si}]$ is the 3 dimensional position vector of satellite i with respect to the centre of the Earth, $[x_R, y_R, z_R]$ is the position vector of the GPS receiver, ρ_i is the range measurement to satellite i and C_b is the common receiver clock bias. The ρ_i 's are also referred to as "pseudorange measurements" because of the large error associated with the clock bias term. The four unknowns in the range measurement equations are the x , y and z components of the GPS receiver position vector (ie. the receiver's location) and the receiver clock bias. The four pseudorange measurements are found by measuring the delay in the propagation of the GPS signal from the satellite to the receiver. The satellite position vectors $[x_{Si}, y_{Si}, z_{Si}]$ are obtained from satellite ephemeris information that is contained within the GPS navigation message. The navigation message is a 50 bit per second data bit stream that is modulated onto both GPS carriers and includes information about the system time, clock correction factors, satellite health and hand over information from the C/A-Code to the P(Y)-Code. The receiver position vector produced by these equations is tied to the WGS 84¹ reference ellipsoid via the satellite ephemeris information. Most GPS receivers will allow their position solutions to be referenced to other reference ellipsoids (eg the Australian National Spheroid) by applying an appropriate coordinate transformation.

The GPS pseudorange measurements are obtained by correlation of the Pseudorandom Noise (PRN) ranging codes transmitted by the GPS satellites with a replica code

¹ WGS 84: World Geodetic System of 1984. A geocentric reference ellipsoid to which the GPS satellite positions are referenced.

generated within the receiver. A second estimate of satellite range can be obtained by integrating the carrier Doppler beat frequency which is produced by the carrier tracking loops. The pseudorange measurements derived by code correlation are absolute but suffer from high levels of thermal and multipath noise, while those derived from the carrier tracking loops are relatively noise free but subject to an unknown integer cycle ambiguity. A combination of these two measurements is required in order to derive low noise estimates of the satellite pseudorange.

The GPS signals consist of two carrier frequencies ($L1=1575.42\text{MHz}$ and $L2=1227.6\text{MHz}$) each of which are bi-phase modulated by PRN ranging codes and GPS navigation data. The PRN codes serve two purposes; (i) to create a direct sequence spread spectrum signal with good multiple access rejection and jamming immunity, and (ii) to enable the GPS receiver to measure satellite ranges by code correlation. Two PRN codes are provided for this purpose, the Precise code or P-Code at 10.23Mbits/s which is modulated onto both GPS carriers, and the Coarse/Acquisition code or C/A-Code at 1.023Mbit/s which is modulated onto the $L1$ carrier only. The US Department of Defence (DoD) reserves the right to deny access to the higher accuracy available from the P-Code by encrypting it with a second code, the W-Code. The resulting P(Y)-Code is then available to authorised users only who are equipped with the appropriate code decryption keys. This process is known as Anti-Spoofing (AS) as its principal function is to protect authorised users from deceptive jamming (or spoofing) by hostile forces. In addition to AS, the US DoD degrade the accuracy available to unauthorised users by dithering the satellite clock and introducing small errors into the ephemeris parameters. This process is referred to as Selective Availability (SA) and can only be removed by users who are equipped with the appropriate decryption keys. It is expected that SA will be turned off over the coming years which will reduce the RMS error for SPS users by at least a factor of two.

The P(Y)-Code is modulated onto both GPS carriers allowing authorised users to measure and therefore remove ionospheric delays directly (see Appendix A). The C/A-Code is modulated onto the GPS $L1$ carrier only, and so unauthorised users are unable to directly measure ionospheric delays and must apply a correction derived from a broadcast ionospheric model (see Appendix C and [1]). Despite this, several techniques have been developed since the introduction of GPS which enable unauthorised users to measure ionospheric delays directly. These include squaring techniques for the measurement of the $L2$ carrier phase [2], cross-correlation techniques for the measurement of the code delay difference between the $L1$ and $L2$ P(Y)-Codes and indirect P(Y)-Code tracking by correlation of the satellite P(Y)-Codes with a locally generated P-Code (the Ashtech P-W tracking technique [3]). All of these techniques suffer from a significant degradation in the signal to noise ratio relative to full correlation. Consequently, noise on the pseudorange measurements obtained through these techniques is much larger than on the corresponding direct P(Y)-Code measurements.

In addition to ionospheric delays, GPS pseudorange measurements are affected by SA, ephemeris errors, tropospheric delays, RF channel biases, multipath and thermal noise.

Expressions for code and carrier phase pseudorange which include these errors are as follows:

$$\text{Code Pseudorange: } \rho = R + c(dt - dT) + d_{\text{TROPO}} + d_{\text{IONO}} + b_S + b_R + n_{Tp} + n_{Mp},$$

$$\text{Carrier Pseudorange: } \phi = R + c(dt - dT) + d_{\text{TROPO}} - d_{\text{IONO}} + b_S + b_R + n_{T\phi} + n_{M\phi} + N\lambda,$$

where R is the true range to the satellite, c is the speed of light, dt is the satellite clock error (including SA), dT is the receiver clock error, d_{TROPO} is the tropospheric delay, d_{IONO} is the ionospheric delay, b_S and b_R are the satellite and receiver inter-channel biases (hardware biases), n_T and n_M are the thermal and multipath errors and $N\lambda$ is the cycle ambiguity in the carrier phase measurement.

The User Equivalent Range Error (UERE) is the RMS or 1σ pseudorange error which results from a combination of all of these error sources. UERE may be converted into an equivalent position and/or time error by multiplying by a factor referred to as the Dilution of Precision (DOP) [4]. The DOP is a geometrical factor which takes into account the 3 dimensional position of all satellites in relation to the receiver and translates line of sight range errors into equivalent position and time errors. Most receivers will choose the four satellites from the available constellation which minimise the DOP in order to derive the best PVT solution. DOP values can be defined for three dimensional position and time (GDOP), three dimensional position only (PDOP), horizontal position (HDOP), vertical position (VDOP) and time (TDOP). Table 1 below gives the error budget for both SPS and PPS receivers as well as typical horizontal and vertical position errors at the 1σ and 2σ levels obtained by applying typical DOP values [5].

Also shown in Table 1 are the position errors expected from Differential GPS over both short ranges (where the ionosphere and troposphere are correlated), and long ranges (where they are assumed to be uncorrelated).

Differential GPS (DGPS) is a technique designed to remove many of the correlated error sources associated with stand alone GPS. A number of DGPS techniques are available, including code DGPS, carrier phase DGPS and Wide Area DGPS (WADGPS). The errors removed in a DGPS system are those which are correlated between the base station and remote receiver and include ionospheric biases, tropospheric biases, ephemeris errors and satellite clock errors. The improvements in accuracy obtained through the use of DGPS will depend on the separation between the base station and remote receiver and the degree to which the error sources de-correlate with distance. In table 1, it is assumed that the tropospheric and ionospheric errors are highly correlated over short range, but completely uncorrelated over long range. The distances over which atmospheric errors become uncorrelated will depend very much on factors such as the geographic location, time of day and season etc. WADGPS is a technique which has been developed to overcome the problem of the decorrelation of errors by modelling many of the error sources over a region using data obtained from a network of base stations. The performance of WADGPS is therefore dependant on

the number and location of base stations and the complexity and accuracy of the error models.

Table 1: PPS and SPS pseudorange error budgets and typical position errors for both stand-alone and Differential GPS receivers.

Error Sources	PPS P-Code	SPS C/A-code (with SA)	PPS DGPS (short)	SPS DGPS (short)	PPS DGPS (long)	SPS DGPS (long)
RMS (1σ) pseudorange errors (m)						
Space Segment (including SA)	3.2	33	0	0	0	0
Control Segment (eg ephemeris errors)	4.3	4.3	0	0	0	0
Ionospheric error (after correction)	2.3	5.0	0	0	2.3	5.0
Tropospheric error	2.0	2.0	0	0	2.0	2.0
Multipath error	1.2	2.5	1.2	2.5	1.2	2.5
Receiver thermal noise	1.1	2.2	1.1	2.2	1.1	2.2
Other user errors (eg channel biases)	0.5	0.5	0.5	0.5	0.5	0.5
UERE (1σ)	6.4	33	1.7	3.8	3.5	6.4
Equivalent position errors (m)						
1σ Horizontal error (HDOP = 1.5)	9.6	50	2.6	5.7	5.3	9.6
2σ Horizontal error (HDOP = 1.5)	19	100	5	11	11	19
1σ Vertical error (VDOP = 2.5)	16	83	4.3	9.5	8.8	16
2σ Vertical error (VDOP = 2.5)	32	166	8.5	19	18	32

3. Overview of the Ionosphere

The ionosphere is a region of the upper atmosphere in which the density of free electrons is large enough to have an appreciable effect on the propagation of radio waves [6]. Although both the upper and lower boundaries of the ionosphere are not precisely defined, for our purposes it can be considered to extend in height from about 50km to 1000km. Below this is the neutral atmosphere (the troposphere and stratosphere) and above is the protonosphere which tends to have a smaller effect on transionospheric radio waves.

The ionospheric plasma is formed by the ionising effects of Solar X-ray and ultraviolet radiation on (mostly) atomic oxygen in the upper atmosphere. As solar radiation penetrates the atmosphere, its intensity decreases due to absorption, while at the same time the density of the atmosphere increases. This tends to result in the formation of a region of maximum electron density (referred to as the F2 layer peak) which resides at an altitude of between 250km and 400km. A typical daytime electron density profile for a mid-latitude location is given in Figure 1 below. In this figure, it can be seen that the plasma forms into layers or regions, the principal of these being the D-region (50 - 90 km), the E-region (90 - 140 km), the F1-region (140 - 210 km) and the F2-region (210 - 1000 km). At altitudes between about 1000km and the orbital height of the GPS satellites is a region of very low density hydrogen plasma which is referred to as the protonosphere. This region has a much smaller effect on radio waves during daylight hours, although its contribution at night can become significant (as the density of the lower layers is diminished). The heights and peak densities of the ionospheric layers vary with the time of day, season, geographic location, Solar and geomagnetic activity.

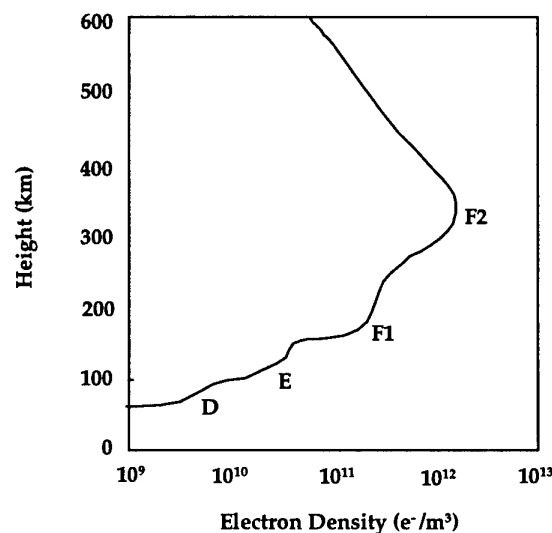


Figure 1: Typical daytime electron density profile for a mid-latitude location.

The ionospheric parameter of principle interest to GPS users is the Total Electron Content (TEC). TEC is defined as the number density of free electrons in a column of 1m^2 cross-sectional area which passes vertically through the ionosphere. With reference to Figure 1, TEC is therefore the integral of the electron density profile from the ground to an infinite height (in practice, the satellite height). In Appendix B, a simple expression is derived from the Appleton-Hartree formula² that relates TEC to the ionospheric refractive index and carrier frequency. It shows that for a modulated waveform at GPS frequencies, the carrier phase is advanced and the code phase delayed by equal amounts which are proportional to the TEC. As most satellites are unlikely to be directly overhead, this delay is in fact proportional to the slant TEC which is the integrated electron density along the line of sight path to the satellite.

The simplification of the refractive index expression given in Appendix B ignores the higher order terms which result from a full expansion of the expression. In addition refractive bending effects which are a function of the angle of incidence, TEC and ionospheric height are also ignored. Both of these effects, however, are negligible when compared to the principal term, except at very low elevation angles.

As TEC is related to the electron density profile, it is also a function of the time of day, season, geographic location, Solar and geomagnetic activity. Both TEC and the peak F2 layer density (N_mF2) show large diurnal variations, reaching a maximum at approximately 1400hrs local time and a minimum just before dawn. The GPS single frequency model (appendix C and Figure 4) employs a half cosinusoid to model this variation, with a constant value of about 9 TECu for the nocturnal TEC. Diurnal variations are particularly large in the lower regions of the ionosphere where the D, E and F1 layers will actually disappear at night. The height of the F2 layer peak (h_mF2) also shows a diurnal dependence, tending to fall at dawn and rise during the evening. In low geomagnetic latitudes, h_mF2 continues to rise during the evening hours reaching a maximum height of about 500km at approximately 1900hrs local time. This effect is due to an upward $E \times B$ force caused by an Eastward electric field in the E region which becomes enhanced after sunset. At these altitudes, free ions recombine very slowly after dusk and so the plasma density remains high. Under the influence of pressure gradients and gravity, the equatorial plasma in the heightened F2 layer is forced downwards along the magnetic field lines, creating regions of enhanced electron density approximately 20° either side of the geomagnetic equator. These enhanced regions are referred to as the equatorial anomaly and the process by which they are created is known as the Fountain effect [7], [8] (Figure 2 below).

² The Appleton-Hartree formula is a general expression for the phase refractive index of the ionosphere.

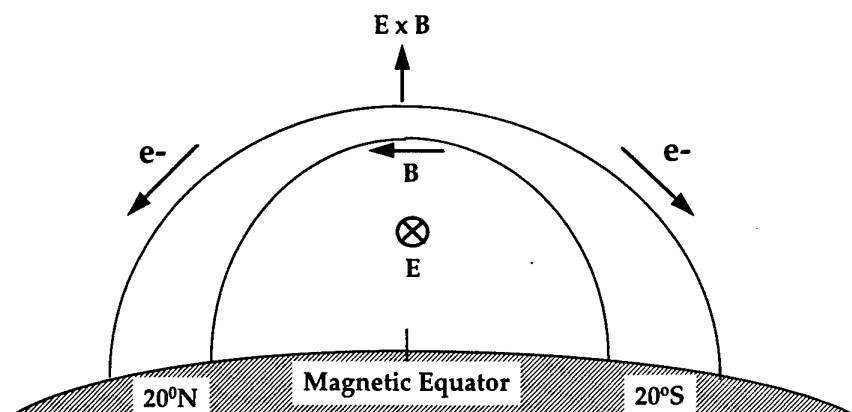


Figure 2: Illustration of the Fountain effect at equatorial latitudes.

In general, the peak electron density of the night-time F region ($NmF2$) is greater in summer than in winter. This result is consistent with the higher levels of Solar radiation and longer daylight hours experienced during the summer months. However, during daylight hours in the mid-latitudes, $NmF2$ is smaller in summer than in winter. This occurs because the F layer splits into an F1 layer and an F2 layer during summer months, and so the F layer thickness becomes larger. In both cases, however, TEC in the summer months is larger than in the winter.

$NmF2$ and TEC are also influenced by the 11 year Solar sunspot cycle (Figure 3). During periods of high Solar activity, $NmF2$, $hmF2$ and TEC are all larger, particularly at the equatorial anomaly. The higher levels of electron density during Solar active years are the result of an increase in the intensity of the Solar winds caused by sunspot activity.

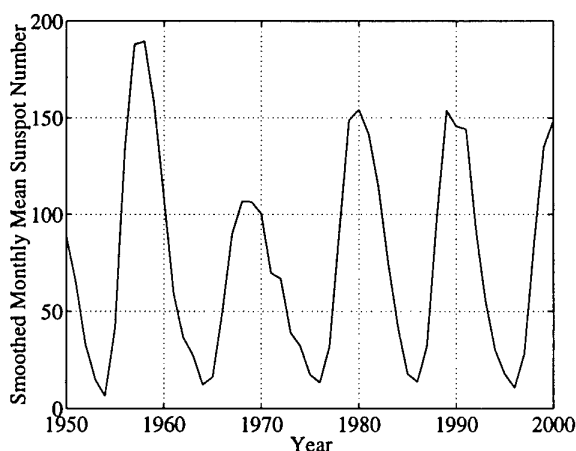


Figure 3. Solar sunspot cycle since 1950 including the predicted peak near the year 2000.

An aspect of importance to GPS users is the existence of irregularities in the density of the ionosphere. Such irregularities are responsible for creating rapid variations in the amplitude and phase of radio signals as they propagate towards the ground. These fluctuations have the potential to disrupt both the tracking and acquisition of GPS signals within a GPS receiver. Significant scintillations are most likely to occur in the region of the equatorial anomaly and in auroral and polar cap areas during periods of high solar activity. The nature of scintillation activity and the morphology of ionospheric disturbances will be discussed in more detail in section 5.

4. Benign Ionospheric Effects on GPS

4.1 Introduction

The effects of the ionosphere can be described in terms of two components; (i) a benign or background component, and (ii) a disturbed component.

The benign component represents the average or background level of the ionosphere and is responsible for biases in the measurement of satellite pseudorange. These biases are substantially reduced in dual frequency GPS receivers which form an ionospheric free pseudorange observable from the L1 and L2 P-Code observables (see Appendix A). This is accomplished by taking advantage of the simple inverse square relationship between the carrier frequency of the GPS signal and the ionospheric delay (see Appendix B). Single frequency receivers, on the other hand, have access to only one carrier frequency and so are unable to measure ionospheric delays directly. Such receivers must rely on a relatively crude ionospheric model which is broadcast as part of the GPS navigation message in order to reduce delays (see Appendix C). This single frequency model is a function of only a few parameters and as such cannot take into account the large semi-permanent structures which exist in the ionosphere such as the equatorial anomaly and mid-latitude troughs. The model is also particularly unsuitable for the Australian region as it is derived entirely from data obtained in the Northern hemisphere (it is known that the ionosphere in the Northern hemisphere does not accurately mirror that of the Southern hemisphere). The benign ionosphere can also introduce errors into DGPS systems if the separation between the base station and remote receivers is large enough for the ionosphere to become de-correlated between the two sites. This is most likely in the equatorial region where the ionospheric plasma can contain large horizontal gradients. For this reason, systems such as WADGPS include an ionospheric model which is updated in real time by ionospheric measurements taken from a network of monitor stations. Such a model is usually based on a second model which contains *a priori* information about the behaviour of the benign ionosphere.

More recently [9], [10], a second civilian frequency (L5) has been proposed which will enable suitably equipped, stand alone SPS receivers to remove the majority of the ionospheric delay. An L5 frequency would make the single frequency model

redundant and would eliminate the need for an ionospheric model for WADGPS. It was intended that L5 be incorporated into the new generation block IIF satellites, but as yet it is not clear whether this will take place (launches of block IIF satellites are to begin in 2001).

The disturbed component of the ionosphere introduces rapid variations in both the amplitude and phase of the GPS signal (usually referred to as scintillations). These variations can result in loss of signal lock if either the rate of change of carrier phase exceeds the carrier tracking loop bandwidth, or the amplitude of the GPS signal falls below the tracking loop threshold (amplitude fading). Scintillations also have the capacity to impair a receiver's ability to acquire or re-acquire the GPS signal. As scintillations affect GPS receivers at the tracking loop level, both single and dual frequency SPS and PPS receivers are susceptible to their effects. At present, the only strategy available to deal with scintillations is to avoid the locations and times for which they are likely to be most severe, or to make use of other navigation aids such as INS.

4.2 Single Frequency GPS

As already discussed, the propagation delays experienced by GPS signals in the ionosphere are a function of both TEC and the frequency of the GPS carrier (Appendix A). Dual frequency receivers exploit this relationship in order to measure and thus remove ionospheric delays directly. This is accomplished by creating an ionospheric free pseudorange observable by forming a linear combination of the two pseudorange measurements at the GPS L1 and L2 frequencies (Appendix B). However, single frequency C/A-Code receivers obtain only one pseudorange estimate at the L1 frequency which precludes the direct measurement of ionospheric delay. To compensate, single frequency receivers apply an ionospheric model [1] in order to estimate these delays.

The single frequency model has a relatively simple structure consisting of eight parameters which are broadcast as part of the GPS navigation message. These parameters are the coefficients of two polynomials which define the phase and amplitude of a half cosinusoid describing the daily variation of ionospheric TEC (Appendix C and Figure 4). The parameters are updated once every few days to account for changes in TEC resulting from variations in solar activity and season. Because the model is based on the Bent ionospheric model [11] which was derived almost exclusively from Northern hemisphere measurements obtained during a notoriously depressed solar maximum, its applicability to the Australian region and/or high solar activity is not well known.

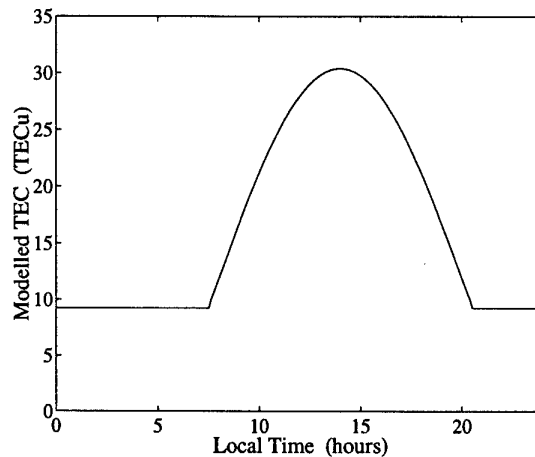


Figure 4: Zenith TEC derived from the GPS Single Frequency model for Darwin, September 1994. Units are 10^{16} e/m^2 (1 TECu).

The simple form of the single frequency model prevents it from including large ionospheric structures such as mid-latitude troughs and the Equatorial Anomaly. This is a significant limitation for users of single frequency GPS in the regions of Northern Australia and South East Asia where the satellite signal paths will occasionally penetrate the anomaly. In Figure 5, it can be seen that the Southern crest of the Equatorial Anomaly (where model errors are likely to be greatest) lies approximately 5 degrees South of the geographic equator at longitudes within the AAI. The northern anomaly crest, on the other hand, lies approximately 25 degrees North of the geographic equator at these longitudes. The exact position of the anomaly can vary by a few degrees from day to day.

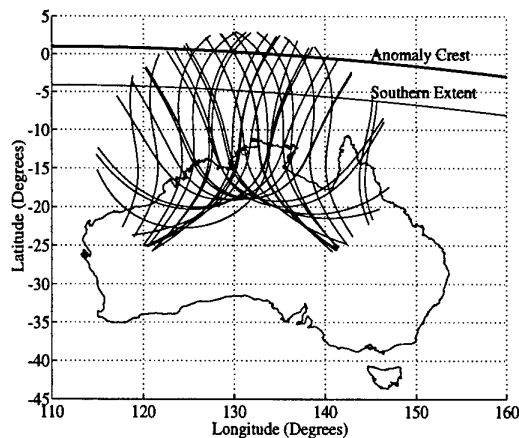


Figure 5: 24 hr coverage of ionospheric pierce points for GPS satellite ray paths at Darwin. An ionospheric height of 600km is assumed. The Southern extent of the anomaly and the anomaly crest are shown.

A number of Northern hemisphere studies have been performed to quantify the performance of the GPS single frequency model. Feess and Stephens [12] compared dual frequency GPS estimates of the RMS delay with GPS Single Frequency model estimates at four stations³ between the years 1980 to 1983. The studies demonstrated that the Klobuchar model [1] reduced RMS error by between 57% and 69% during daylight hours which exceeded the specified levels of performance. Night time errors, however, were reduced by less than 50%. In addition, the RMS errors remaining after correction at near equatorial stations (Guam and Hawaii) were much larger than at the other two stations (Vandenberg and Alaska) as absolute TEC was much greater at the equatorial stations. It was also noted that the model performed particularly well over the Continental United States, a region for which it has been optimised. To date there have been no thorough studies of the accuracy of the single frequency model in the Australian region and the lack of suitable GPS data during the last solar maximum (1990) would make such a study difficult to achieve in the short term.

An example illustrating the performance of the GPS Single Frequency model in low latitude regions in the Southern hemisphere can be obtained by comparing Figures 6, 7 & 8. Figure 6 represents vertical TEC over the Cocos Islands region obtained from the Single Frequency model for days 100 and 101 of 1995 (near Solar minimum). The simple sinusoidal nature of the Klobuchar model and the constant nocturnal value of 10 TECu⁴ is apparent from this figure. Another feature is the gradual increase in both the amplitude and period of the cosinusoid with latitude (approximately 5 TECu between 20° S and 3°S). Figures 7 & 8 represent approximately 14 hours of GPS TEC measurements for the same two days in 1995. This data was obtained from the AUSLIG⁵ GPS monitor station on Cocos Islands (12.18° S, 96.83° E) and processed using the TEC estimation technique outlined in Appendix D. The x-axis on these plots is local time which was obtained by combining the longitude of the ionospheric intercept point with Universal time (*i.e.* $t_{\text{LOCAL}} = t_{\text{UT}} + 12 \cdot \lambda^{\circ} / 180$). The y-axis is the latitude of the ionospheric intercept point. The ionospheric intercept point is defined as the equivalent latitude and longitude of the intercept point between the signal ray path and the centroid height of the ionosphere. By comparing Figure 6 (model) to Figures 7 & 8 (measurements) it is apparent that the phase and period of the model is approximately correct, but the magnitude of the vertical TEC is significantly different at low latitudes. At a latitude of 20° S, the model and measurements vary by less than a few TECu (corresponding to less than a metre of range error). The reduction in ionospheric error will therefore be of the order of 90% or so during daylight hours (in this particular case). However, at a latitude of 5°S the model is approximately 33 TECu below measurement on both days, and so the reduction in error will only be approximately 43%. 33 TECu of vertical delay corresponds to approximately 90 TECu of slant delay (assuming an elevation angle of 10°) which corresponds to a

³ Vandenberg, Guam, Hawaii and Alaska.

⁴ TECu is a measure of Total Electron Content: 1 TECu = 10^{16} electrons/m² which is equivalent to a delay of 0.542ns at L1 or a range error of 0.163m.

⁵ AUSLIG - Australian Surveying and Land Information Group.

pseudorange error of about 15m at L1. Clearly, this is not a rigorous assessment of the model's performance in this region, but it does demonstrate that at low latitudes where the magnitude of TEC is particularly large, the reduction in error can be less than 50% leaving a significant residual error term. Model performance during the nocturnal hours is generally of less importance because of the much lower levels of TEC. However, it has been shown [14] that during these times, the application of a model can result in poorer performance than simply ignoring the effect. During a solar maximum, this analysis would be expected to reveal much larger errors.

Ionospheric models such as the broadcast single frequency model indicate that vertical position errors and time errors are much greater than horizontal position errors. Studies by Jorgensen [15] based on the GPS model suggest that vertical errors are approximately 6 times greater than horizontal position errors, while time errors (when converted to distance) are approximately 8.5 times greater. This situation arises because the ionospheric errors are highly correlated between satellites in such a model, and so are substantially absorbed into the receiver clock bias term (*ie.* N-S and E-W errors cancel, but because there are no satellites below the receiver, height errors do not). The implication of this result is that the ionosphere is not a significant source of error for users requiring horizontal accuracy only (*ie.* ships). Although this may be true at mid-latitudes, it is not necessarily the case at equatorial latitudes or at dawn and dusk when large horizontal gradients can exist.

UNCLASSIFIED

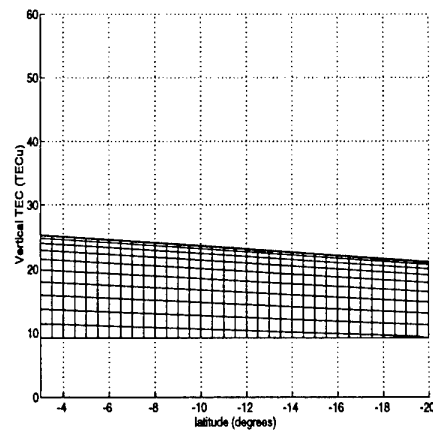
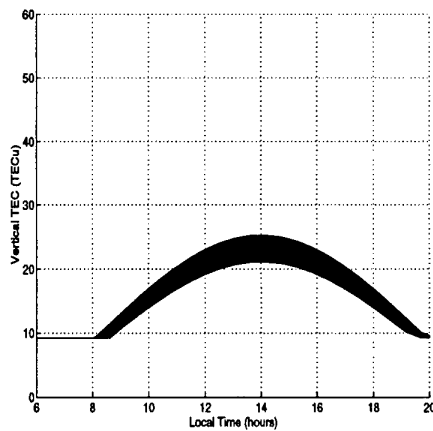
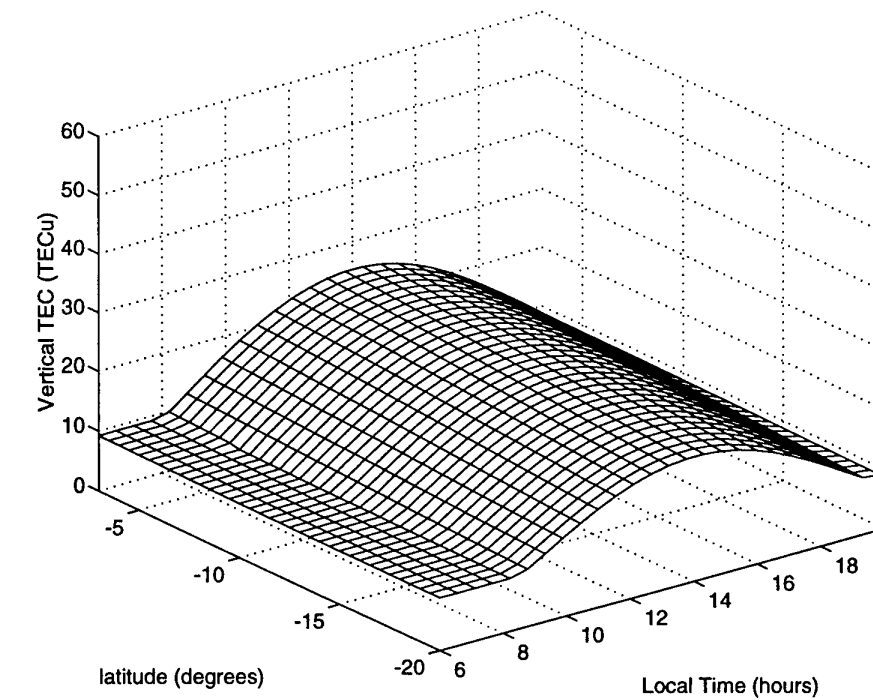
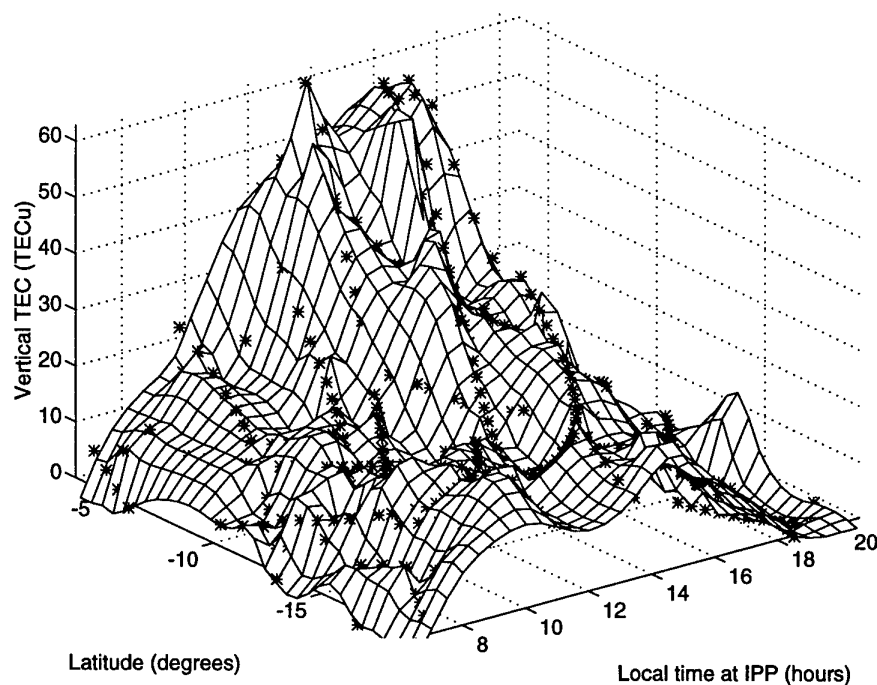
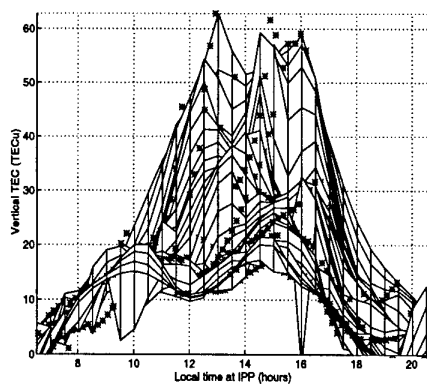


Figure 6: Surface plot of Vertical Ionospheric Total Electron Content over the Cocos Islands region from the Klobuchar single frequency model (days 100 and 101 of 1995).

UNCLASSIFIED



TEC as a function of Local Time



TEC as a function of Latitude

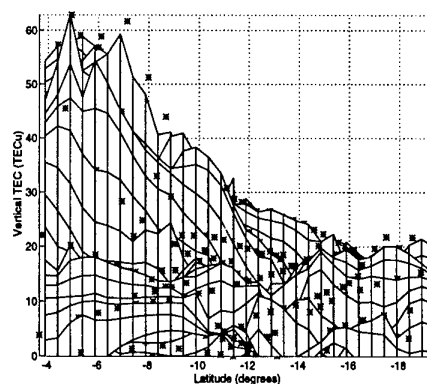
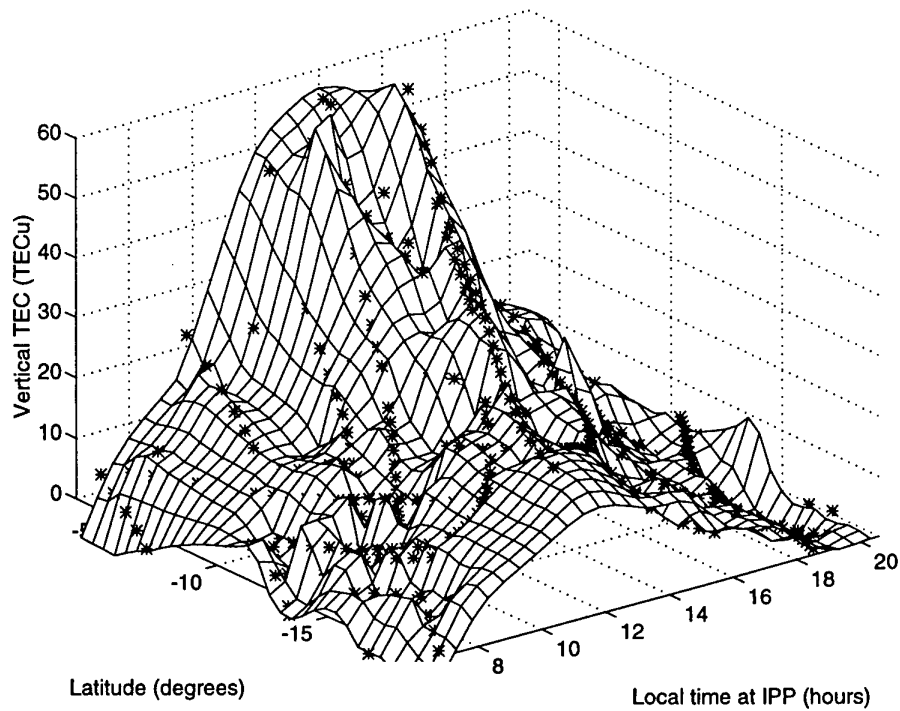
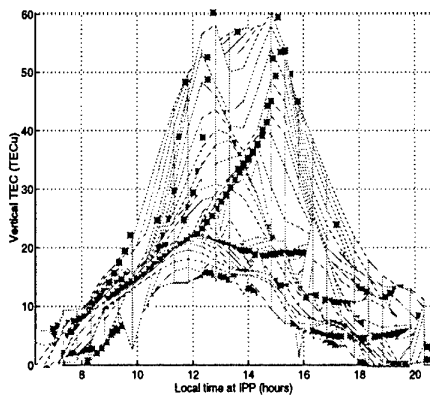


Figure 7: Surface plot of Vertical Ionospheric Total Electron Content (TEC) from Cocos Islands (12.18° S, 96.83° E) on day 100 of 1995 (data period 00:00 to 14:00 UT). An Elevation mask angle of 15° and an Ionospheric Pierce Point height of 350km has been chosen.



TEC as a function of Local Time



TEC as a function of Latitude

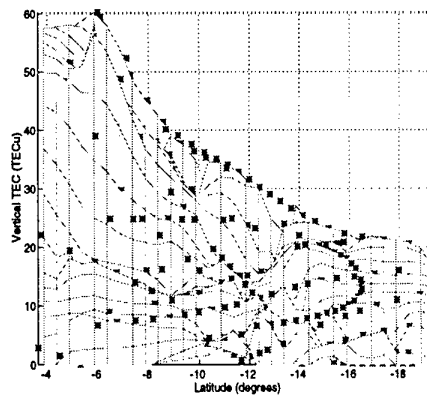


Figure 8: Surface plot of Vertical Ionospheric Total Electron Content from Cocos Islands on day 101 of 1995 (data period 00:00 to 14:00 UT). An Elevation mask angle of 15° and an Ionospheric Pierce Point height of 350km has been chosen.

4.3 Wide Area Differential GPS

Differential GPS (DGPS) is limited somewhat by the de-correlation of various error sources with increasing distance from the reference station. Such errors include ephemeris errors, tropospheric delay errors, and ionospheric delay errors. Of these, the most significant for single frequency users is the ionospheric delay error. WADGPS is designed to overcome these limitations without the need to install a large number of monitor stations by modelling the three error sources in real time. Model parameters are then broadcast to all users within the area of interest via, typically, a communications satellite.

Several WADGPS systems are currently being developed including the United States Federal Aviation Administration (FAA) system designed to cover the Continental United States (CONUS) for precision aircraft approach ([16] & [17]), a European system being developed by Racal Research and others ([18] & [19]) and a system proposed by the Ionospheric Prediction Service (IPS) for the Australian region. The proposed FAA system uses the Klobuchar model and an inverse distance weighted scheme to convert station measurements of slant TEC into vertical TEC estimates at the nodes of an imaginary grid. This grid covers the region of interest (in this case the CONUS) with a spacing of 10 degrees in latitude and longitude. Vertical TEC estimates at each grid node along with the corresponding latitudes and longitudes are then broadcast to all users via a geostationary INMARSAT communications satellite. Users of the system then estimate vertical TEC at the ionospheric intercept points for each satellite by interpolating from the grid using the four enclosing nodes. The vertical TEC estimates are then converted back to slant TEC through an appropriate obliquity factor and applied directly to the pseudorange measurements. The European system employs an ionospheric model which is based on two existing empirical ionospheric models; the Boston University Slab Thickness Model and the URSI 1988 foF2 model. This combined model has the added advantage of permitting HF sounder measurements of foF2 to be incorporated into the model along with GPS TEC measurements. Consequently, a denser network of monitor stations is available for the ionospheric modelling component of the system. The IPS system employs an inverse distance weighted scheme similar to that used by the FAA (without Klobuchar model weighting) to create a real time map of TEC from the AUSLIG network of GPS stations. At present, such a system is intended primarily for use by the CAA.

In all the proposed WADGPS architectures, ionospheric TEC is modelled over a region using data obtained from a network of GPS monitor stations separated by several thousand kilometres or so. User estimates of vertical TEC at each ionospheric intercept point are obtained from a broadcast WADGPS ionospheric model and converted back to slant TEC by applying an obliquity factor. Obvious sources of error in this process are in the conversion from slant TEC to vertical TEC (for the creation of the ionospheric model), the conversion of vertical TEC back to slant TEC by the user, and interpolation errors. Conversions such as these which involve an obliquity factor make assumptions about the vertical structure of the ionosphere which may not always be correct. Models incorporating vertical structure such as the Bent ionospheric model

may help in this respect, particularly if supplemented by HF sounder measurements of ionospheric peak height (h_mF2), critical frequency (f_oF2) and $M(3000)$. Local ionospheric disturbances (so called Travelling Ionospheric Disturbances or TIDS) and large horizontal gradients will also reduce the accuracy of WADGPS by preventing the horizontal structure from being correctly modelled. Again, the equatorial regions are likely to be affected more in this respect. Also, GPS monitoring networks such as the AUSLIG Fiducial Network were not originally designed for WADGPS and may require supplementary stations in order to achieve a satisfactory level of accuracy (particularly during solar maxima). To date, issues relating to the decorrelation of the ionosphere with distance in the Australian region have not been adequately addressed.

5. Disturbed Ionospheric Effects on GPS

5.1 Introduction

Although the effect of the benign ionosphere on single frequency GPS and DGPS systems is of interest, it is not considered to be of crucial importance as the ADO have access to dual frequency P(Y)-Code receivers which can be used when high levels of accuracy are required. In addition, techniques such as Cross-Correlation and P-W tracking [3] as well as WADGPS can be used to substantially reduce ionospheric delays without requiring access to the P(Y)-code⁶. The benign ionosphere is, however, closely linked to the disturbed ionosphere, and as such an understanding of its morphology is essential to the study of ionospheric disturbance behaviour. For microwave frequency satellite based systems such as GPS, the principal manifestation of a disturbed ionosphere is scintillations in the received signals.

Ionospheric scintillations are rapid variations in the amplitude, phase, angle of arrival and polarisation of radio signals resulting from electron density irregularities in the ionosphere. For GPS, only the variations in amplitude and phase are important, as refractive bending by the ionosphere at L-band is negligible, and polarisation rotation has no effect on the circularly polarised GPS carriers. Scintillations lead to an increase in the noise on GPS pseudorange and range rate measurements, as well as an increase in the probability of losing signal lock. These effects will occur in all types of GPS systems, including single frequency receivers, dual frequency receivers, DGPS and WADGPS systems. Although scintillations are unlikely to affect all of the satellites in a receiver's field of view, they will, impact on the accuracy of the resulting navigation solution by degrading the geometry of the available constellation. Consequently, the coverage of both the satellites and the irregularities, as well as the intensity of scintillation activity will all contribute to the accuracy of the final solution. Also, in hostile electromagnetic environments, tracking loops which have been weakened by scintillation activity will become more susceptible to the effects of jamming. Quantifying the increase in the jamming susceptibility of receivers affected by scintillations is an important direction for future research in this area.

5.2 Morphology of Scintillations

Scintillations occur predominantly in the equatorial band which extends from about 20°S to 20°N of the magnetic equator, and in the auroral and polar cap regions. The processes which produce scintillations in these two regions are quite different, leading to significant differences in the characteristics of the resulting scintillations. Auroral and polar cap scintillations are mainly the result of geomagnetic storms⁷ which are

⁶ However, for Cross-Correlation and P-W tracking receivers, Selective Availability errors will still be present.

⁷ Variations in the strength and direction of the Earth's magnetic field.

associated with solar flares⁸ and coronal holes⁹. Unlike equatorial scintillations, they show little diurnal variation in their rate of occurrence, and can last from a few hours to many days, beginning at any time during the day [25]. Large and rapid variations in TEC are often associated with auroral and polar cap scintillations [26] and can lead to significant errors in DGPS systems as well as rapid changes in the apparent range and range rate [27], [25]. Auroral scintillation activity also shows a seasonal dependence which is the reverse of that observed at low latitudes, being greatest from the autumn equinox through winter to the spring equinox, and a minimum during the summer months [28]. Indeed, the geomagnetic disturbances which excite auroral and polar cap scintillations tend to suppress the onset of equatorial scintillations during solar maximum [8], [27], [29]. However, because geomagnetic storm activity is associated with solar activity (through solar flares and coronal holes), auroral and polar cap scintillations do show a strong dependence on the solar cycle, being most intense during solar maximum, but almost non-existent during minimum.

Equatorial scintillations, on the other hand, are produced by the collapse of the E-layer and the subsequent rise of the F-layer in equatorial regions after the passage of the evening terminator, and tend to disappear soon after midnight. As equatorial scintillations are coupled to the anomaly, they tend to be worse during the years of solar maximum when the anomaly is at its greatest, and tend to show the same seasonal dependence as the anomaly. Consequently, the next peak in equatorial scintillation activity is expected to coincide with the forthcoming solar cycle maximum in the year 2000 (see Figure 3). In the discussions which follow, only equatorial scintillations will be considered as they are of the greatest operational interest to the ADO and also tend to be more severe than their auroral counterparts [27]. In addition, the latitude band which is affected by equatorial scintillations covers approximately 50% of the Earth's surface as compared to only 7% for the auroral and polar cap regions. However, it should be mentioned that during intense magnetic storms, auroral disturbances can extend well into the mid-latitudes, disrupting GPS through both scintillation activity and large density gradients. An example of this was the magnetic storm of March 1989 during which auroral scintillation effects were felt over most of the continental United States causing narrow bandwidth (1Hz) receivers to frequently lose signal lock [25]. However, such events are uncommon.

The most severe scintillation activity appears to be associated with the crests of the equatorial anomaly which are centred approximately 15° either side of the magnetic equator. For example, observations of scintillation activity at 1.5GHz using the Marisat geostationary satellite show fading depths greater than 20dB occurring up to 30% of the time beneath the anomaly crest at Ascension Island (350km ionospheric intersection dip latitude of 17°S). However, fades rarely greater than 3dB occurred near the magnetic equator at Huancayo, Peru. These measurements were taken during the

⁸ Sudden increases in the intensity of solar electromagnetic radiation associated with sunspot activity. Flares cover the frequency band from radio to X-ray.

⁹ Low density regions of the solar corona which are associated with solar winds (high energy charged particles from the sun).

high sun-spot period of 1980-1981 [30]. Similar measurements made during a solar minimum at the same locations showed virtually no scintillation activity at 1.5GHz. Equatorial scintillations also show a strong seasonal dependence, being greatest during the months of April to August¹⁰ in the Pacific longitude sector, but a minimum in the American, African and Indian sectors. This situation is reversed during the months of October to March¹¹ [27]. During the seasons of high scintillation activity, the equinoctial months of March and September tend to suffer the highest levels of activity, although this does not appear to be true at all longitudes [31]. The reason for this complex association between longitude and season at equatorial latitudes is not well understood [30], and is therefore not predictable in a reliable way at this stage. The diurnal, latitudinal and solar cycle variations are, however, quite well understood and are therefore relatively predictable, at least in a statistical sense.

Equatorial scintillations are mainly caused by irregularities formed during the collapse of the lower regions of the ionosphere during the evening hours. After sunset, the E-layer and the lower regions of the F-layer recombine more rapidly than the upper regions, leading to an unstable situation akin to a heavy fluid being supported on a lighter fluid¹². This situation eventually leads to the formation of bubbles of low density plasma which are forced upwards through the denser upper regions. As the bubbles grow, steep density gradients at the walls cause smaller irregularities to form [32]. At GPS frequencies, these smaller irregularities, which can be of the order of the Fresnel zone radius (300m) and less, are responsible for scintillation effects [29]. The bubbles eventually form into irregularity patches, often called 'plumes', which can reach heights of up to 1500km at the magnetic equator. These patches extend along the magnetic field lines in a North-South direction for over 2000km, leading to an accumulation of irregularities in the Northern and Southern anomaly regions ($\pm 15^\circ$ DIP latitudes - see Figure 9). The East-West extent of these patches is typically 100 to 200km, and they move in an Easterly direction with velocities of the order of 50 to 200 m/s [33]. This causes scintillations to occur in patches which can last for an hour or so, with periods of little or no scintillation activity in between [29]. Eventually, in the absence of solar radiation, recombination causes the irregularity patches to fade, along with the associated scintillation activity. This usually occurs around local midnight, although scintillations can occasionally persist until early morning. Scintillations can also occur during daylight hours when Sporadic-E is present in the E-layer. Sporadic-E is a region of highly dense plasma at heights of about 100km in which large density gradients can exist. However, scintillations produced by Sporadic-E are less common than those produced by the F-layer processes described above.

¹⁰ Centred on the June Solstice.

¹¹ Centred on the December Solstice.

¹² This is referred to as a Rayleigh-Taylor instability.

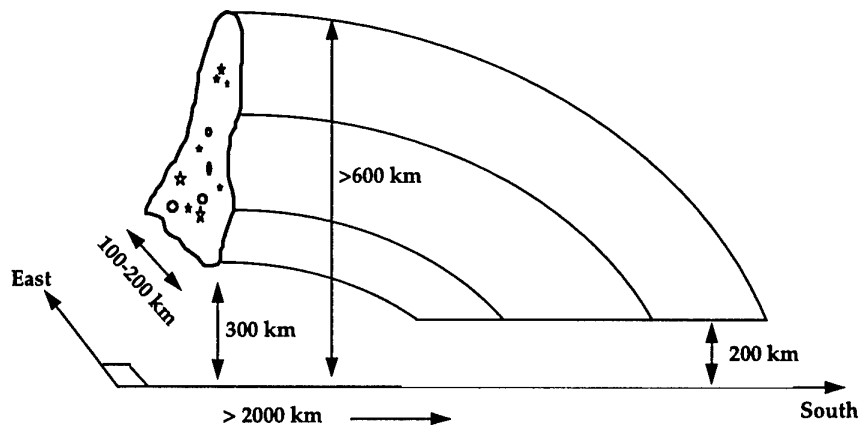


Figure 9: A three dimensional model showing how an irregularity patch maps along the field lines from the geomagnetic equator to the anomaly regions.

To date there have been few measurements of equatorial L-band scintillations during solar maximum, particularly in the Australian and South-East Asian regions. Much of the GPS data which has been collected so far has been for reasons other than scintillation studies¹³ and tends to be at sampling rates which are much less than the bandwidth of the scintillations. Consequently, such data is often heavily aliased and cannot provide useful spectral information. In addition, amplitude information is often either missing or is in a form which is unsuitable for amplitude scintillation studies. For example, data is frequently recorded in the internationally recognised RINEX data format which scales the signal to noise ratio into the integer range of 1 to 10. For these reasons, the majority of useful data on equatorial L-band scintillations has been obtained from experiments specifically designed to observe these effects. These include the observations made by Aarons [34] during the 1979-1980 solar maximum, and those by Wanninger [35] in Hawaii during the 1990 solar maximum. A campaign of measurements involving TEC and scintillation monitoring GPS receivers is to begin shortly in the South-East Asia region. This will aim to measure the effects of scintillations on GPS and to verify existing scintillation models leading up to the year 2000 solar maximum. Wide Area Surveillance Division (WASD) will report on the results of this study in due course.

5.3 Scintillation Models

Scintillations result from changes in the phase velocity of sections of a satellite signal wavefront as it propagates through density irregularities in the ionosphere. The amplitude of the emergent wave is unaffected by the irregularities as absorption by the ionosphere at L-band frequencies is usually negligible. As the wave propagates towards the ground, mutual interference across the wavefront creates complex patterns of amplitude and phase variations which are a function of both the range to

¹³ Data recorded for DGPS and Integrity monitoring purposes etc.

the irregularities and the cross-range position. Scintillations are produced when these spatial diffraction patterns are converted into temporal ones, either through relative motion between the receiver and the patterns, or by changes in the structure of the irregularities with time.

5.3.1 Fresnel-Kirchoff Diffraction model

A simple model, based on Fresnel-Kirchoff diffraction theory, which demonstrates the effects of a collection of Gaussian shaped irregularities on a vertically propagating plane wave is given in Appendix F. This model assumes that the density irregularities are concentrated within a thin layer at a height which is typical of the F2 layer peak height. The resulting patterns of amplitude and phase variations on the ground are then derived using simple diffraction theory. The model provides an insight into the types of irregularities which are likely to produce scintillations at L-band, as well as the characteristics of the resulting signals. At GPS frequencies, irregularities with scale sizes of the order of the first Fresnel Zone radius¹⁴ or smaller are likely to produce the most significant scintillation effects. Larger irregularities produce very little amplitude variation and only gradual phase variation, unless the density gradients are extremely large. Very small irregularities (tens of metres or less) produce quite complex diffraction patterns, but at an intensity which is too low to have a significant effect on GPS. In Figure 10, three examples are given of the diffraction patterns produced by an isolated irregularity using the model in Appendix F. From this figure, it is apparent that the 100m irregularity, which is approximately one third the size of the Fresnel zone radius, produces the most significant amplitude variations (centre plate). For the case of three equally spaced irregularities of the same size, the diffraction patterns become very complex and contains many deep null's (Figure 11). In general, because the Fresnel zone radius at L-band frequencies is so small, large density gradients are required in order to produce significant scintillation effects. This tends to restrict the majority of scintillation activity to the equatorial anomaly and polar regions where large TEC and density gradients are known to exist.

¹⁴ The Fresnel zone radius is approximately 276m at GPS L1 and 312m at GPS L2. This assumes an irregularity height of 400km which is typical of the height of the F2-layer peak.

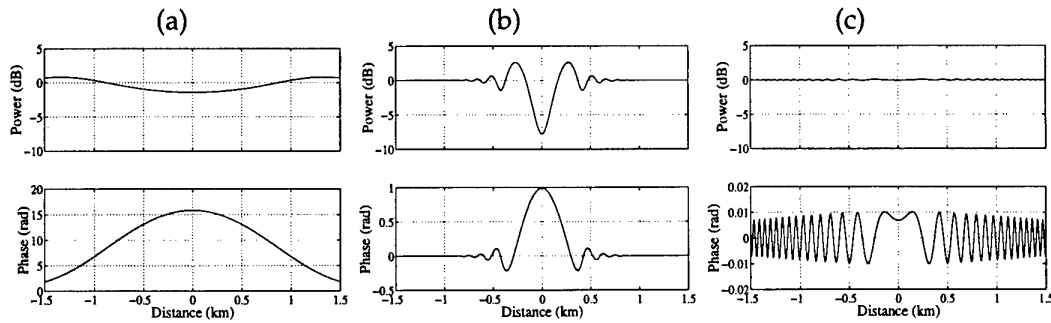


Figure 10: Modelled diffraction patterns based on a thin screen diffraction model and an isolated Gaussian shaped irregularity (see Appendix F). Scale sizes of the irregularities are 1km (a), 100m (b) and 10m (c). The irregularities were centred at a height of 400km with a peak density variation of 500% over background.

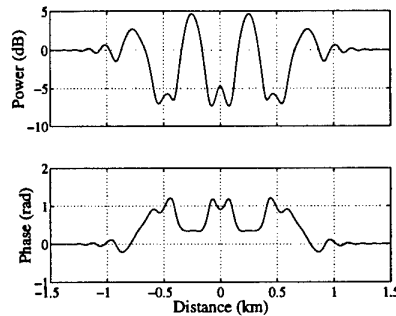


Figure 11: Modelled diffraction patterns for a collection of three 100m Gaussian shaped irregularities separated by 400m. The irregularities were all centred at a height of 400km with a peak density variation of 500% over background.

For an isolated irregularity which is smaller than the first Fresnel Zone radius, the thin screen diffraction model of Appendix F produces an amplitude diffraction pattern consisting of regular oscillations with wavelengths equal to twice the separation of the Fresnel zones. These oscillations die out when the separation of the respective Fresnel zones becomes less than the size of the irregularity [36]. Consequently, the scale size of an irregularity determines the rate of decay of the diffraction pattern envelope, but does not influence the wavelength of the oscillations. The absence of significant oscillations with wavelengths greater than the first Fresnel zone radius leads to a low frequency cutoff in the amplitude scintillation spectrum¹⁵. This cutoff is at a frequency ν_F which is proportional to the relative velocity between the propagation path and the

¹⁵ A phenomenon known as Fresnel Filtering.

irregularities (V_R), and inversely proportional to the Fresnel zone radius (z_F), assuming a frozen flow model for the irregularities¹⁶;

$$\nu_F = \frac{V_R}{z_F} \text{ Hz}$$

where $z_F = \sqrt{\frac{\lambda z_1 z_2}{z_1 + z_2}}$ and z_1 and z_2 are the distances between the ionospheric

irregularity layer and the satellite and receiver. Weak focusing and de-focusing caused by refraction creates energy at frequencies below ν_F , but unless density gradients are extremely large, these fluctuations tend to be at a low level (top panel in Figure 10a). Although phase diffraction patterns also consist of regular oscillations with wavelengths related to the Fresnel zone radius, the phase scintillation spectrum does not have a well defined low frequency cutoff. This is because, unlike the amplitude patterns, the phase patterns are a mixture of both diffraction effects and the original phase perturbations which were imposed onto the emergent wave. Consequently, irregularities larger than the Fresnel zone radius are capable of producing long wavelength phase variations which contribute significantly to the low frequency end of the phase scintillation spectrum (bottom panel in Figure 10a).

For frequencies greater than the low frequency cutoff, both the amplitude and phase scintillation spectra follow an inverse power law relationship of the form $T \cdot \nu^{-p}$, where T is the spectral strength at 1Hz, ν is the fluctuation frequency and p is the spectral index¹⁷ (see Figure 12) [8, 38]. For the phase scintillation spectrum, T is of the form:

$$T = N \lambda^2 C_k L \sec(\theta) G V_R^{(p-1)}$$

where N is a normalisation factor, λ is the carrier wavelength, $C_k L$ is a measure of the density and thickness of the irregularity layer (the height integrated irregularity strength), G is a factor which accounts for the geometry and orientation of the irregularities, θ is the off-vertical incidence angle of the propagation path at the irregularity layer and V_R is the relative velocity. For GPS, the relative velocity V_R is strongly dependant on the irregularity drift velocity and the receiver velocity, but only weakly dependant on satellite motion¹⁸. By changing V_R through receiver motion, the scintillation spectra will be translated either to the left or right, depending on the direction of motion of the receiver in relation to the direction of drift of the irregularities (*i.e.* both T and ν_F will change) This effect, in conjunction with the higher levels of loop stress experienced during motion, has the potential to significantly alter a receiver's tolerance to scintillation activity. This will be discussed further in the next section. Under weak scintillation conditions, the spectral index p is related to the slope

¹⁶ In a Frozen Flow model, the structure of an irregularity patch remains fixed as the patch moves relative to the ground.

¹⁷ p is typically in the range 1 to 4.

¹⁸ In other satellite based systems such as TRANSIT where the orbital heights and orbital periods are much less than those of GPS, satellite motion can contribute significantly to V_R .

of the three dimensional irregularity spatial power spectrum q by $p=q-1$. The spatial power spectrum is therefore of the form k^{-q} , where k is the three dimensional spatial wavenumber of the irregularities. Consequently, for weak scattering at least, a simple link exists between the spatial spectrum of irregularities in the ionosphere and the observed scintillation spectra on the ground. At equatorial latitudes, measurements have shown that the in-situ spectral slope q is typically about 3.5. Consequently, the spectral index p is about 2.5 and is independent of motion. Thus, receiver motion may change the horizontal position of both scintillation spectra, but will not alter the spectral slope.

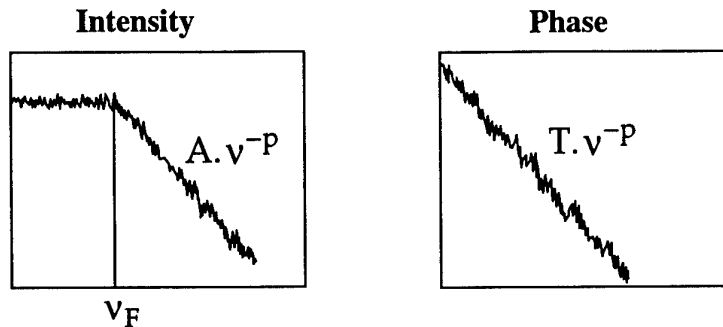


Figure 12: Cartoon of typical intensity and phase scintillation power spectra.

By providing a more realistic in-situ density profile for the irregularity layer, the Fresnel-Kirchoff diffraction model will produce time series amplitude and phase scintillation data which has more realistic statistics. In Figure 13 a realisation of a random, Gaussian distributed density layer with an in-situ spectral slope¹⁹ of 2 was used in place of the individual Gaussian shaped irregularities described earlier. The wavenumber power spectrum of the vertically integrated density profile is given in panel (a) along with a straight line representing a slope of -2. The low frequency cutoff at a wavenumber of approximately -31 dBmetres⁻¹ is produced by assuming an outer scale size of about 1.3km for the irregularities. The power spectra of the resulting amplitude and phase scintillation data (panels (b) and (c)) also have a spectral slope of 2, with the amplitude scintillations displaying a low frequency cutoff at a wavenumber which corresponds to the first Fresnel zone radius (about -26dBmetres⁻¹ for an irregularity layer height of 400km). In addition, the phase scintillation spectrum shows evidence of Fresnel oscillations which also begin at a wavenumber of -26dBmetres⁻¹. The measured Probability Density Functions (PDF's) of both amplitude and phase are consistent with the expected PDF's for scintillations (Gaussian for phase and Nakagami-m for amplitude [39] and Appendix G). As shown in panel (d), the phase scintillations appear to be Gaussian distributed, while in panel (e) the amplitude scintillations appear to be Nakagami-m²⁰ distributed. The smooth curves overlying

¹⁹ For the integrated density profile.

²⁰ The Nakagami-m distribution is a semi-empirical probability distribution function which has been shown to provide the best fit to amplitude scintillation data [39].

both of these plots are the theoretical distribution functions derived from the appropriate PDF equations given in Appendix F. More rigorous statistical tests would need to be applied in order to confirm that the data does follows the assumed distribution functions.

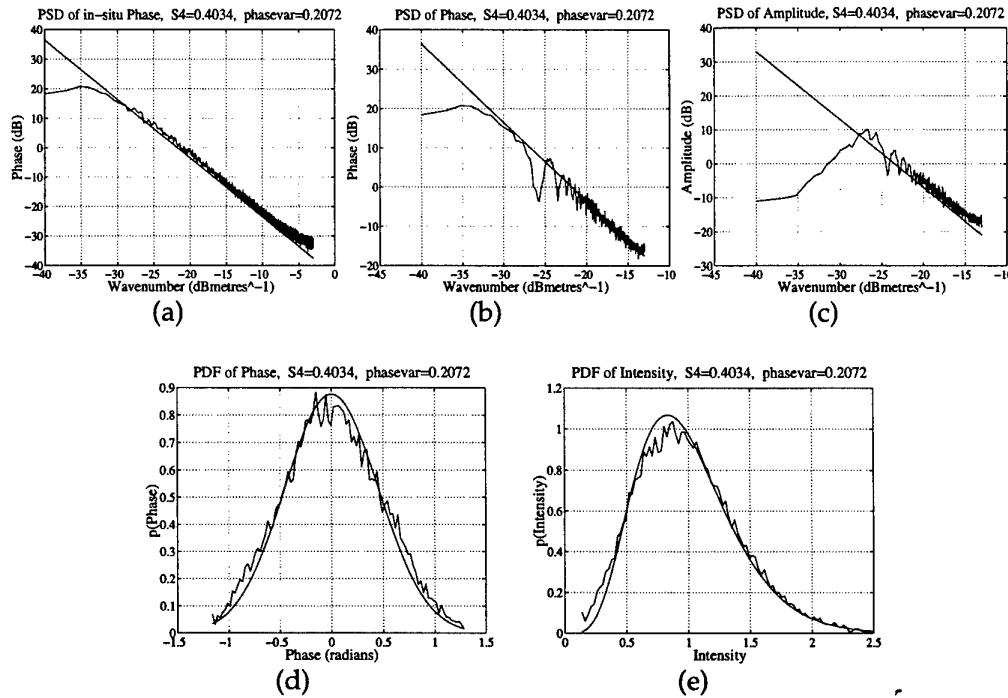


Figure 13: Statistics resulting from a random, Gaussian distributed density layer with an in-situ spectral slope for the integrated density of 2. Shown are the in-situ spectrum (a), the phase scintillation power spectrum (b), the amplitude scintillation power spectrum (c), the phase PDF (d) and the Intensity PDF (e).

5.3.2 Wide Band Scintillation Model (WBMOD)

The WideBand ionospheric scintillation MODel (WBMOD [40]) is a global model of ionospheric scintillation activity which enables users to predict the levels of scintillation activity at a given time and location. The equatorial portion of the current version of WBMOD is based on data from widely separated longitude sectors including Huancayo in Peru (12°S, 75°W), Kwajalein Island (9°N, 167°E), Ascension Island (7.6°S, 14.2°W) and Manila (14.4°N, 121°E). The parameters provided by WBMOD are the spectral index p , the spectral strength T , occurrence statistics and estimates of the rms phase and intensity scintillation levels. WBMOD consists of two parts; a collection of empirically derived models of the global distribution and characteristics of F-layer irregularities, and a power law phase screen propagation model to calculate the levels of scintillation activity in a user defined system. The

propagation model assumes a spectral index value of 2.5 at equatorial latitudes, and calculates T from a series of eight parameters provided by the irregularity models. These parameters include the in-situ spectral slope ($q = p - 1$), the height integrated irregularity strength ($C_k L$), the in-situ drift velocity of the irregularities, the phase screen height, three parameters describing the geometry and orientation of the irregularities and an outer scale size. The only external inputs required are the carrier frequency, the transmitter and receiver locations, local time, sunspot number, and the planetary magnetic activity index. In addition to T , p and the occurrence statistics, WBMOD also provides measures of the rms levels of phase scintillation (σ_ϕ) and the normalised (by the mean) rms intensity scintillation ($S4$). Integrating the power spectral density of phase scintillations over a band of phase fluctuation frequencies ($v_2 - v_1$) gives the mean square phase:

$$\sigma_\phi^2 = 2 \int_{v_1}^{v_2} \frac{T}{(v_o^2 - v^2)^{p/2}} \cdot dv = E\{\phi^2\} - E\{\phi\}^2$$

where ϕ is the carrier phase and $E\{\}$ is the expectation operator. Consequently, σ_ϕ is a function of T , p , bandwidth and a low frequency limit v_o which is based on the outer scale size of the irregularities. $S4$ is also a function of T and p , but contains a Fresnel filter factor (F) and the Fresnel zone radius (z_F) which together account for the low frequency cutoff in the intensity scintillation spectrum;

$$S4 = M \frac{T}{G} F \frac{z_F^{(p-1)/2}}{V_R^{(p-1)}} = \sqrt{\frac{E\{I^2\}}{E\{I\}^2} - 1}$$

where M is a normalisation factor and I is the signal intensity. Both σ_ϕ and $S4$ are commonly used measures of scintillation activity and show a simple dependence on the carrier frequency [8, 38, 41]. For low to moderate levels of scintillation activity ($S4 < 0.5$), $S4$ scales with carrier frequency as $f^{-(p+3)/4}$. Under strong scintillation conditions, $S4$ is approximately 1 at all frequencies. The rms phase, on the other hand, shows an f^{-1} dependence for both weak and strong scattering, unless scattering is exceptionally strong. Consequently, the L2 frequency will be affected slightly more by scintillation activity than L1 (by a factor of about 1.4 for $S4$ and 1.3 for rms phase). This adds to the problem of an inherently higher level of susceptibility at L2 as a result of the reduced SNR on the L2 P-Code (rms phase jitter due to thermal noise on the L2 P-Code is $\sqrt{2}$ times greater than jitter on the L1 P-Code, and twice as large as jitter on the C/A-Code).

An example of the output provided by WBMOD is given in Figure 14. The scintillation indices $S4$ and σ_ϕ are provided in the top panel, the Spectral Strength parameter T is in the centre panel and the Spectral Slope p is in the lower panel. All plots are a function of latitude at a longitude of 120°E and are at the 70th percentile (ie. The

activity is stronger than the specified level for only 30% of the time). This example represents a period of high Solar activity during the evening hours when scintillations are expected to be at their strongest. The two humps at approximately 25°N and 5°S correspond to the Northern and Southern equatorial anomaly crests.

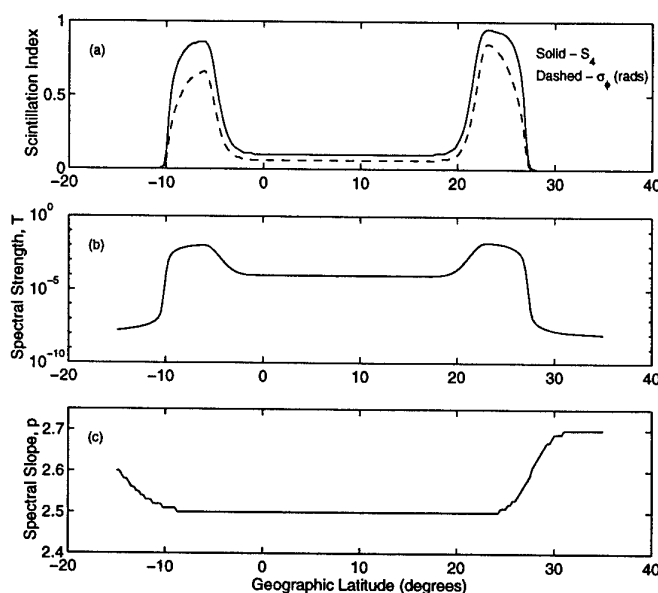


Figure 14: An example of the scintillation indices provided by WBMOD (April 10, 21:00hrs local time, Longitude 120°E, Receiver altitude 0km, Satellite altitude 20,000km, 70th percentile, Frequency=1227.6GHz, R12=150, Kp=2, Phase stability of receiver 10s).

The statistical parameters provided by WBMOD can be used to determine the performance of a GPS receiver tracking loop in a scintillation environment. By combining this knowledge with occurrence statistics (also provided by WBMOD), predictions can be made about the likely performance of a receiver at a given time and location. Sections 5.5 and 5.6 describe the links between the statistical parameters provided by WBMOD and the expected performance of a single code/carrier tracking loop.

5.3.3 Synthetic Scintillation Time Series Model (SSTS)

The objective of the SSTS model is to generate scintillation time series with specific amplitude and phase statistics for testing against a GPS receiver tracking loop simulator (described later). The SSTS model is essentially a more sophisticated version of the Fresnel-Kirchoff diffraction model which has the advantage of being linked to the WBMOD scintillation model. The SSTS model generates amplitude and phase scintillation data which have power spectra and PDF's which are consistent with both

measured scintillation data (eg [39]) and the statistical parameters provided by WBMOD (S_4 and σ_ϕ etc.). Consequently, phase scintillation data is Gaussian distributed with an inverse power law power spectrum, whereas amplitude scintillations are Nakagami-m distributed and have a low frequency cutoff in the power spectrum. A more detailed description of the SSTS model is given in Appendix G.

Figure 15 displays an example of the output produced by the SSTS model with intensity scintillation shown in the top panel and phase scintillation bottom. The input S_4 and σ_ϕ were 0.90 and π radians respectively, the spectral slope (for both intensity and phase) was 2.30, and the time resolution was 0.01 s.

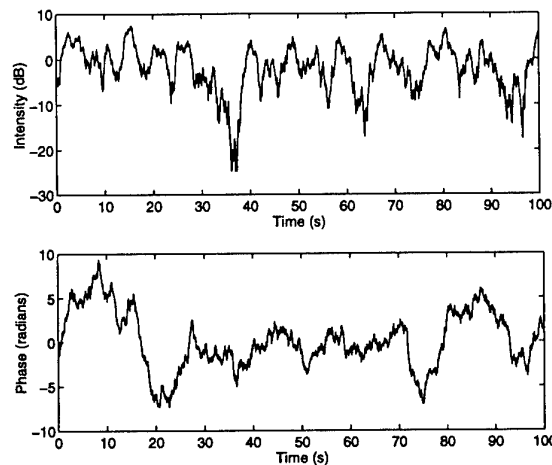


Figure 15: Example of the SSTS model output showing intensity and phase scintillations (top and bottom respectively).

Statistical analysis of the resultant model data shows that the output S_4 has a value of 0.89 and a spectral slope of 2.32 which are in good agreement with the input values. The output σ_ϕ is exactly π as the phase scintillation data is renormalised to the desired level.

It is important to verify that the model data PDF's and power spectral densities are that which is required. Figure 16 shows the PDFs of the modelled intensity (top) and phase (bottom) scintillation data. In both cases the dashed line is the expected PDF (Nakagami-m with $m = 1.23$ and Gaussian with $\sigma_\phi = \pi$ respectively). For both intensity and phase the PDF's are in good agreement with the expected distributions. Figure 17 displays the power spectra of the modelled scintillation data and again it is clear that it is in good agreement with the desired spectra.

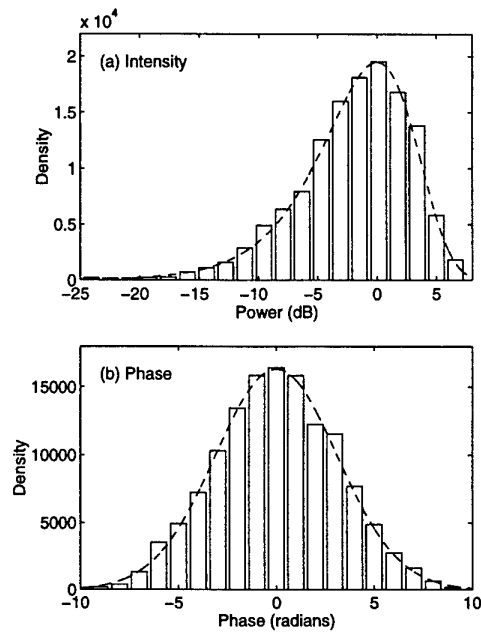


Figure 16: Probability density functions for the modelled intensity (a) and phase (b) scintillation data of Figure 15.

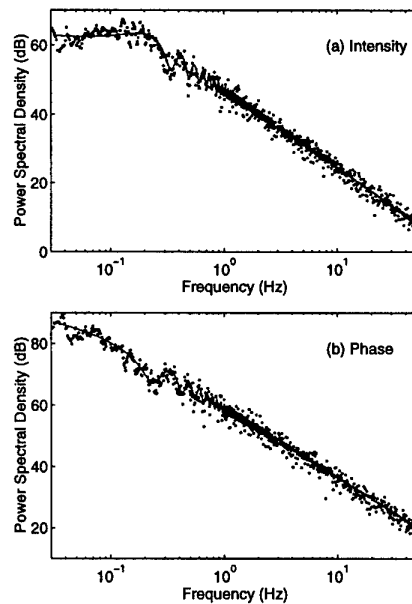


Figure 17: Power spectra of the modelled intensity (a) and phase (b) scintillation data from Figure 15 (dotted lines) with the desired power spectra overlaid (solid lines).

Although it is intended that the SSTS model will replace the less sophisticated Fresnel-Kirchoff diffraction model, at present only preliminary tests have been conducted using this model. Some results from these tests on a Costas carrier tracking loop are given in section 5.4.3. The results of a more thorough series of tests based on the SSTS model and the GPS System Simulator will be provided in a subsequent report.

5.4 Impact of Scintillations on GPS

The impact of scintillations on GPS is being investigated by a combination of numerical simulation and signal processing modelling. The numerical simulation technique has the advantage of accounting for the inherent non-linearities which exist in both the code and carrier tracking loops, whereas the signal processing model has the potential to offer a deeper insight into the reasons for the observed behaviour. Both techniques have been applied to the combined code and carrier tracking loops of a single receiver channel.

The response of a GPS receiver's tracking loops to perturbations in the incident signal is dependent upon a number of factors. These include:

1. The type of code and carrier tracking loop.
2. The bandwidth and order of the loop filters.
3. Input from external sensors such as INU's.
4. The type of the loop discriminators.
5. The ambient Carrier-to-Noise density ratio (C/No).
6. The magnitude and type of external interference.
7. The response of the AGC and antenna electronics.
8. The number of channels and their tracking strategy (*i.e.* parallel, sequential, etc.).
9. The nature and sophistication of the tracking algorithms (*i.e.* Kalman Filters).

In the analysis presented here, however, it is assumed that the receiver consists of a standard Phase Locked Loop (PLL)/Delay Locked Loop (DLL) design of the type described below. Consequently, no account is taken of the potential impact of AGC, front-end limiting, tracking algorithms, or the impact scintillation activity may have on the receiver's capacity to track and decode the navigation message. Also, no account is taken of the effects of multiple receiver channels (other channels will assist with re-acquisition if they have not already been affected by scintillations).

5.4.1 GPS System Simulator

Time domain simulations of the response of a GPS receiver tracking loop to scintillations have been conducted using a GPS receiver tracking loop simulator and the scintillation model based on Fresnel-Kirchoff diffraction theory (described in section 5.3.1 and Appendix F). The scintillation model assumes that density irregularities are concentrated within a thin, time-invariant diffraction screen which is frozen within the background plasma and moving at a constant velocity relative to the Earth. Relative motion between the irregularities and the receiver is assumed to be responsible for translating the spatial diffraction patterns into scintillations. The effects

of satellite motion and time variations in the structure of the irregularities are ignored. The GPS simulator has been designed to replicate the functions of a GPS receiver's tracking loops as closely as possible, including all non-linearities introduced by the correlators and the tracking loop discriminators. Consequently, tracking loop performance is simulated in both the quasi-linear region where phase errors are small, and in the non-linear region near the tracking loop thresholds.

The simulator consists of three principal blocks: a satellite simulator, an environment simulator, and a receiver simulator (Figure 18). At present, the satellite simulator generates an L1 and L2 carrier signal which is bi-phase modulated by the appropriate PRN timing codes. The environment simulator then introduces additive, Gaussian white noise (thermal noise), interference, ionospheric effects (including delays and scintillation effects), platform and satellite dynamics. In the absence of any external interference or scintillation attenuation, the carrier-to-noise density ratio (C/N_0) of the incident signal is approximately 45 dB-Hz, corresponding to a signal level of -160 dBW and a noise power density of -205 dBW-Hz. From the environment simulator, the satellite signal is passed into the receiver simulator, where it is processed by the code and carrier tracking loops.

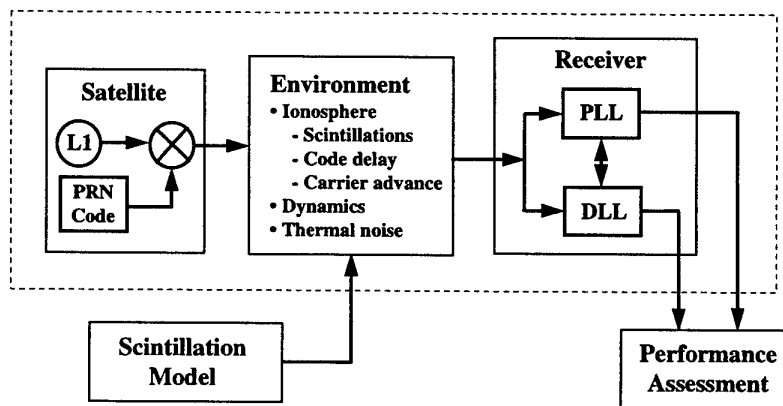


Figure 18: Block diagram representation of the GPS system simulator.

At present, a delay locked loop (DLL) is used with an early minus late envelope discriminator for code tracking, and a Phase Locked Loop (PLL) with a four quadrant arctangent phase discriminator for carrier tracking. In addition, the DLL is carrier-aided by the PLL which has the effect of eliminating virtually all of the platform and satellite dynamics from the DLL as long as carrier lock is maintained. Consequently, the DLL will remain in lock whenever the PLL is tracking. The loop orders of both the code and carrier tracking loops can be chosen to be either 1, 2 or 3. For an un-aided receiver, typical loop orders are 2nd order for the code tracking loop, and 3rd order for the carrier tracking loop.

The coefficients of the code and carrier loop filters were chosen for minimum mean square error. This ensures that transient overshoot is kept to a minimum in response to rapid changes in phase. Carrier phase lock information is derived from the punctual I and Q signals (I_P & Q_P) using the following lock state indicator [42, pp 393]

$$\left((\Sigma I_P)^2 - (\Sigma Q_P)^2 \right) / \left((\Sigma I_P)^2 + (\Sigma Q_P)^2 \right)$$

In this method, the carrier loop is assumed to be tracking the incoming signal if the above ratio exceeds a threshold value of 0.4. This indicator, however, should be used in conjunction with the known code and carrier phase range information to assess the extent of code and carrier lock. Notice also that because code lock is required in order to remove the code from the underlying carrier, carrier phase lock implies that the code loop is tracking.

5.4.2 Simulation Results

A large number of simulations have been conducted in which the characteristics of both the irregularities and the receiver were varied. Some preliminary results from these simulations using the Fresnel-Kirchoff diffraction model and a series of discrete Gaussian shaped lenses are given below (see [43] for more detail). Future work will concentrate on the application of the more sophisticated SSTS scintillation model to the receiver simulator.

1) Both the transient response and the steady state errors of a narrow bandwidth receiver are worse than those of a wide bandwidth receiver. Consequently, the rapid variations in carrier phase caused by scintillation activity stress the carrier tracking loops of a narrow bandwidth receiver more than those of a wide bandwidth receiver. As a result, narrow bandwidth receivers are more likely to lose lock on an incoming signal. Figure 19 shows the lock state indicators for three receivers employing 3rd order carrier tracking loops and 2nd order code tracking loops. The carrier and code loop bandwidth's for these receivers are 2Hz & 0.8Hz, 5Hz & 1Hz, and 10Hz & 2Hz, respectively. The rate of change of Doppler on the incoming GPS signal was typical of a stationary receiver and a satellite relatively low on the horizon (*i.e.* approximately constant Doppler and a zero steady state tracking error). The scintillation patterns were obtained using Fresnel-Kirchoff diffraction theory (Appendix F) with an assembly of moderately dense ionospheric irregularities at a height of 400km all travelling at 100m/s. The narrow bandwidth receiver (upper panel) lost lock on several occasions, whereas the wide bandwidth receiver (lower panel) did not, although it was significantly stressed by the scintillations. In all cases, because the Doppler shift on the incoming signals was approximately constant, the receivers returned to their normal tracking states with zero mean tracking error once the disturbance had passed.

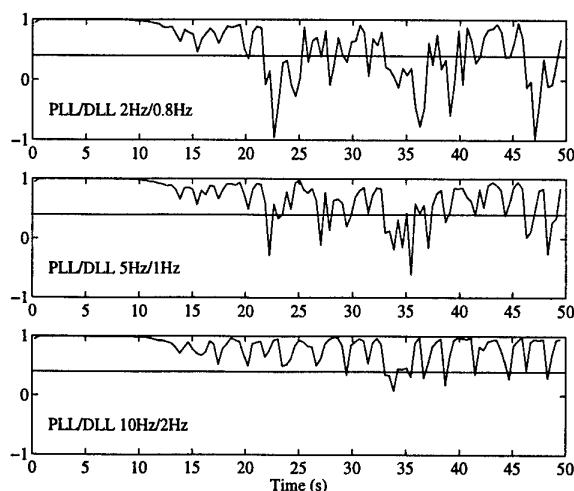


Figure 19: Carrier phase lock states for 2Hz/0.8Hz, 5Hz/1Hz, & 10Hz/2Hz bandwidth receivers in the presence of moderate simulated scintillation activity. The line at 0.4 represents the approximate threshold level for carrier phase lock.

2) Phase scintillations appear to have a more significant impact on a receiver's tracking loops than amplitude scintillations. Figure 20 compares the carrier phase lock indicators of 10Hz/2Hz and 2Hz/0.8Hz receivers in response to combined phase and amplitude scintillations, and the same scintillations with first the phase and then the amplitude scintillations suppressed. By comparing these figures it can be seen that the wide bandwidth receiver generally performs better than the narrow bandwidth receiver. This is mainly the result of the wide bandwidth receiver's superior capacity to track the rapid variations in phase which are associated with phase scintillations (central panel). Although the narrow bandwidth receiver copes with amplitude scintillations better than the wide bandwidth receiver, the improvement in performance is only marginal (lower panel). Other tests performed using irregularities of different sizes and separations produced similar results. It is, however, likely that the impact of amplitude scintillations will become more significant when the relative velocity between the irregularities and the receiver is small. Under these conditions the receiver is likely to dwell for longer periods in the troughs of the amplitude scintillation patterns, while at the same time experiencing reduced phase stresses as a result of the lower phase rates.

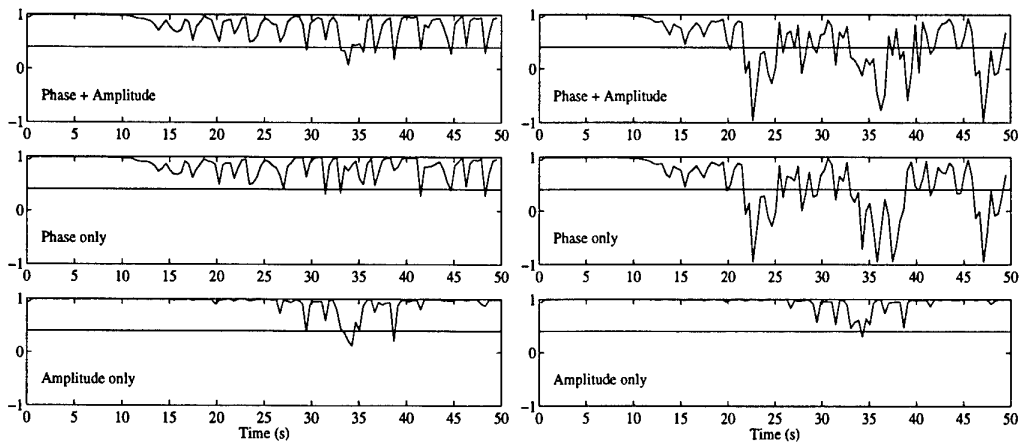


Figure 20: Carrier lock states for a 10Hz/2Hz receiver (left panels) and a 2Hz/0.8Hz receiver (right panels) in response to phase-amplitude scintillations (upper panels), phase-only scintillations (centre panels), and amplitude-only scintillations (lower panels) based on the Fresnel-Kirchoff diffraction model.

3) As the relative velocities between the receiver and the ionosphere increase, the duration of amplitude fading events will decrease. Consequently, the impact of amplitude scintillations is likely to be reduced at high velocities (*i.e.* high frequency amplitude scintillations are likely to be removed by the pre-detection filters in the tracking loops). Conversely, an increase in velocity will increase the frequency of phase scintillations making them harder to track. Preliminary results suggest that at high velocities, the increased susceptibility from phase scintillations outweighs the reduced susceptibility from amplitude scintillations, making the receiver in general more vulnerable. When the velocity of the irregularities was increased to 600 m/s with the same Doppler conditions as those outlined under item 1, all of the receivers suffered from cycle slips and eventually lost lock. Once the disturbance had passed, however, all receivers were able to re-acquire the signal.

4) Under the same ionospheric conditions, but with less favourable Doppler similar to that of a satellite at its point of closest approach, the narrow bandwidth receiver was unable to track the incoming signal or re-acquire it after the disturbance had passed. The wide bandwidth receiver, on the other hand, managed to track the signal through the activity, although it did suffer from cycle slips during the most severe parts of the disturbance (the upper panel of Figure 21 shows the difference between the actual and the observed phase ranges for this receiver). Subjecting the same receiver to a constant 2g acceleration, such as might be experienced during flight, resulted in it losing lock and being unable to re-acquire, even after the irregularity had passed (Figure 21, lower panel). In the absence of any scintillation activity all of the receivers were capable of tracking the incoming signals correctly under the specified dynamic conditions.

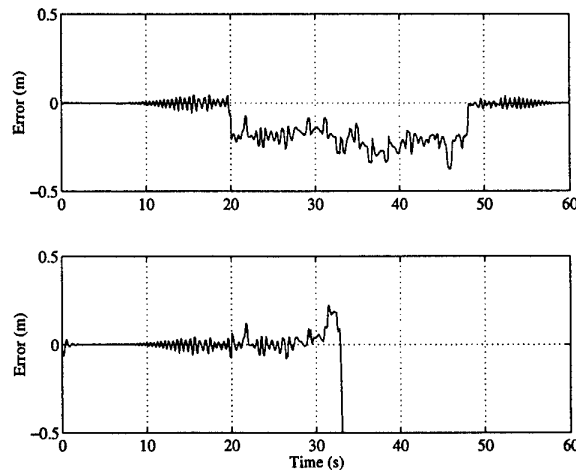


Figure 21: Carrier phase range errors of a wide bandwidth receiver subject to scintillation activity from the Fresnel-Kirchoff diffraction model under both unfavourable satellite Doppler conditions (upper panel), and a constant 2g platform acceleration (lower panel).

Acceleration stresses will in general make tracking more difficult for both wide and narrow bandwidth receivers. This is the result of two effects:

- Under acceleration conditions, a receiver suffers from additional tracking errors which add to the scintillation and thermal noise errors.
- More importantly, once lock is lost, the PLL will have difficulty regaining lock on a carrier which is continually changing. In a real GPS receiver, the other channels and/or INS aiding will help the affected tracking loop to regain lock (unless all channels have been affected or there is no aiding). These effects have not yet been modelled.

5) Carrier phase DGPS is likely to gain some benefit from the filtering effects of narrow bandwidth receivers. This will become more pronounced at high relative velocities as the power spectra of both the amplitude and phase scintillations are shifted to higher frequencies. This advantage will of course be negated if the receiver loses lock, which as explained earlier, is more likely for narrow-band receivers.

6) The short wavelengths of the phase disturbance patterns produced by small irregularities (those with scale sizes less than the first Fresnel zone radius) means that the errors in the carrier loops will become de-correlated over very short baselines. Consequently, receivers that use carrier phase DGPS techniques to establish their positions (e.g. high precision navigation systems, attitude determination systems, etc.) are likely to be profoundly affected by these disturbances. Figure 22 shows the phase response of a wide bandwidth receiver to a number of small irregularities (scale size = 30m) with peak TEC variations of about 0.25 TECu. In this case, the relative velocity between the ionosphere and the receiver is 200m/s. Although no cycle slips have occurred, the rms errors have increased from about 1mm prior to the scintillation activity to around 10mm at its centre (with peak errors around 20mm). The

wavelength of the central component of the disturbance pattern on the ground is approximately 290m, which is about the radius of the first Fresnel zone. Consequently, receivers would need to be separated by much less than this in order for the errors to be correlated. Figure 23 shows as a function of separation the difference in the phase errors between two GPS receivers subject to the above irregularity. Notice that the errors increase very rapidly as separation increases, reaching a maximum at about $\frac{1}{2}$ the Fresnel zone radius. Small-scale irregularities of this sort are particularly important because they are likely to be far more common than the more dense ones. Moreover, they can also occur as a result of irregularities within the lower layers of the ionosphere and are therefore not restricted solely to the evening hours of solar maximum.

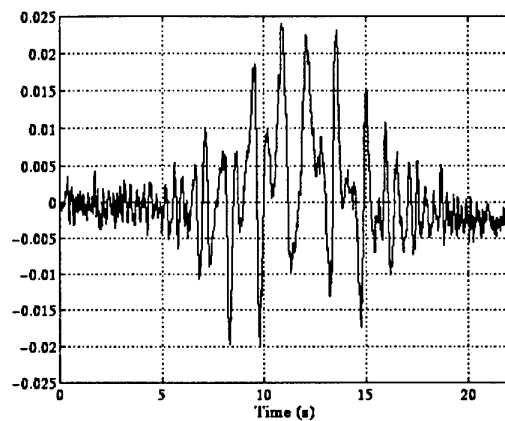


Figure 22: RMS phase response of a 10Hz carrier tracking loop resulting from scintillations produced by an assembly of 30m ionospheric irregularities with peak TEC variations of 0.25 TECu. The relative velocity between the irregularities and the receiver is 200m/s.

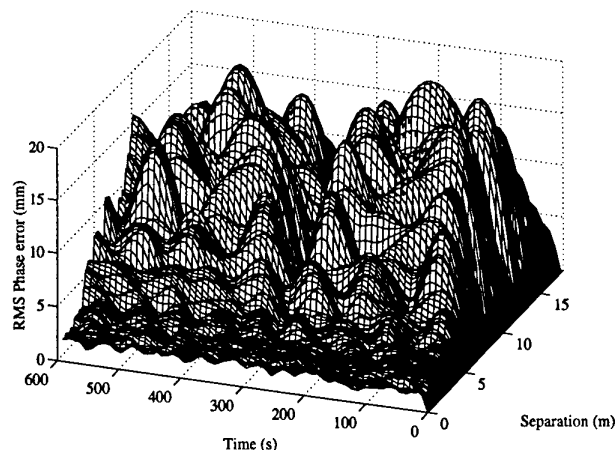


Figure 23: Differential phase range errors as a function of time and antenna separation for the scintillation activity outlined in Figure 22.

5.4.3 Preliminary results from the SSTS model

In Figure 24, the results of a test conducted on a second order Costas loop using SSTS simulated data are given. The loop bandwidth (5Hz) and order are typical of a stand alone GPS receiver. The SSTS simulated data was generated with an S_4 of 0.6 and σ_ϕ of π radians.

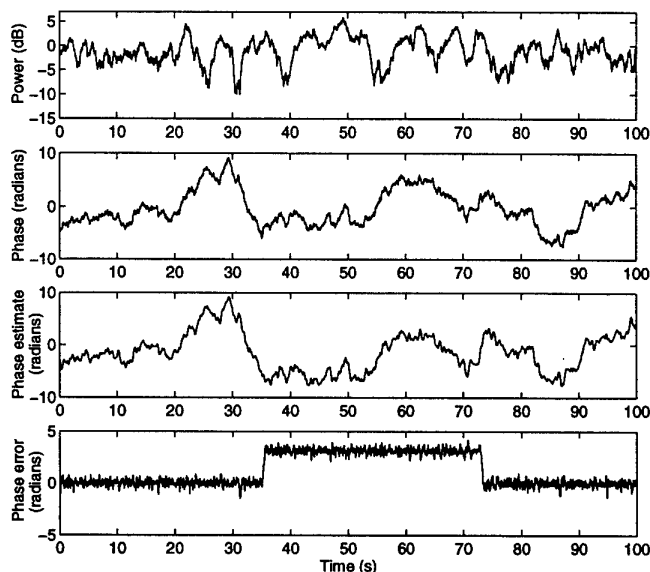


Figure 24: Results from inputting SSTS model data ($S_4 = 0.6$ and $\sigma_\phi = \pi$) into a second order Costas loop with a 5 Hz bandwidth. The top two panels show the input intensity and phase scintillation data respectively, the third panel displays the phase estimate of the Costas loop, and the bottom panel shows the phase error which (difference between the input phase and the phase estimate). Note the incidents of cycle slips in the phase error which are indicative of the Costas loop experiencing difficulties in maintaining signal lock.

From examination of Figure 24 one can see that the Costas loop is stressed and experiences cycle slips at times of 36 and 73 seconds. The phase error (which is the difference between the input phase and the phase estimate of the Costas loop) at these times jumps by π radians. It is interesting to note that at these times the signal power does not experience any significant fading, although an increase in the phase error noise is evident at a time of 32 seconds where a -10 dB fade is experienced. On the other hand, the input phase data does show large rates of change at the times of the cycle slips. Therefore, in this case it is the phase scintillation which is stressing the Costas loop.

Other tests with different levels of S_4 and σ_ϕ were also performed. The results of these tests are not displayed here; however, briefly, we found that the Costas loop was stressed to a greater degree by one type of scintillation (*i.e.* intensity or phase

scintillation) over the other under certain conditions. We found that when the relative speed of the ionospheric irregularities transverse to the propagation path was small, then intensity scintillation played a greater role in determining if the loop lost lock, while for large transverse speeds it was the phase scintillation that caused loss of lock. These results are expected; for large irregularity drift speeds transverse to the propagation path any fading in the signal power will be short in duration and the integrator in the Costas loop is able to average the signal over the fade. However, large drift speeds cause any changes in phase to be more rapid; thus, the loop will be stressed if there is any appreciable phase scintillation activity. The reverse is true for small irregularity drift speeds; now the phase changes will be slower but the fades in the signal power will be longer in duration. Thus, under this condition it is intensity scintillation which stresses the Costas loop. A following report will describe these observations and results in detail.

5.4.4 Additional Comments

1) Dual frequency receivers track both the L1 and L2 carriers in order to remove the biases introduced into the receiver's position by the ionosphere. If the two measurements are assumed to be uncorrelated, then the variance of the corrected phase observable, σ_c^2 , is derived from the individual variances of the L1 and L2 measurements, σ_{L1}^2 and σ_{L2}^2 as follows [14]:

$$\sigma_c^2 = 6.48\sigma_{L1}^2 + 2.39\sigma_{L2}^2 = 10.4\sigma_{L1}^2$$

Consequently, any attempt to eliminate ionospheric delays from the L1 phase observable using the L2 observable will increase the measurement variance of the corrected range estimate.

2) A tightly integrated Inertial Navigation System (INS) can improve a GPS receivers tolerance to external interference by allowing the tracking loop bandwidth's to be significantly reduced (along with the order of the loop filter). Unfortunately, this means that the unit is now more susceptible to scintillation activity and has a higher probability of losing lock. Once the disturbance has passed, however, position estimates provided by the INS will allow the receiver to re-acquire the incoming signal much more rapidly. The effects of prolonged scintillation activity and INS drift upon GPS-INS systems have yet to be investigated.

3) The tracking threshold for a PLL is given by $3\sigma_T + \frac{1}{\omega_0^n} \frac{d^n R}{dt^n} \leq 45^\circ$, where σ_T is the rms thermal noise, R is the line of sight range to the satellite, and n is the loop order. For a disturbance consisting of both high frequency, noise-like components and low frequency variations, the variance of the noise-like components will add to the thermal noise error, while the low frequency variations will add to the range component. By using a high loop order, the error resulting from the low frequency component can be reduced without adding to the noise. However, for a fixed loop order, a change in

bandwidth by a factor k will change the envelope error by k^n and the noise by \sqrt{k} (assuming that the noise components of the irregularity are white over the bandwidth's of interest).

4) For an ionospheric drift velocity of 100 m/s, the corner frequency for Fresnel oscillations is of the order of 0.3Hz. Consequently, for small irregularities which produce diffraction effects with minimal interference, the PLL filters will allow most of the irregularity power through, regardless of noise bandwidth (the carrier noise bandwidth's of GPS receivers are usually greater than 1Hz to accommodate the changing Doppler imparted by the satellites). In other words, such oscillations would be slow enough for stationary receivers to track. This may not be the case for high platform velocities and narrow bandwidth's (such as those encountered in INS-aided receivers), or when the electron density gradients are large enough to produce significant interference effects. In these cases, both amplitude and phase scintillation energy will be shifted to higher fluctuation frequencies.

5) Cross-correlation and P-W tracking receivers [3] are more susceptible to loss of lock than direct correlation receivers because of the inherently lower SNR on the P2-P1 channels (cross-correlation) and P2 & P1 channels (P-W tracking). Under strong scintillation conditions, these receivers may only be capable of tracking the C/A-Code and the L1 carrier phase which are obtained by direct code correlation.

6) For scintillation activity levels below the lock limits for a PLL, frequent cycle slips may still occur which can complicate cycle slip repair and degrade the performance of carrier phase DGPS systems. This is particularly true for dynamic systems for which loop stresses may be higher and ambiguity resolution is more difficult.

7) Finally, to compensate for the deviation from unity of the radio wave group and phase refractive indices, dual frequency GPS receivers use a linear approximation of the Appleton-Hartree equation [8]. Moreover, it is also assumed that both the L1 and L2 GPS signals travel from the satellite to the receiver along the same geometric paths. The residual effect of combining these two approximations is about a 1% error in the total ionospheric correction [14]. In the presence of significant ionospheric gradients along the signal paths, however, the separation between the L1 and L2 GPS signals will be considerably greater than in the case when the ionosphere is benign or homogeneous. This will again introduce errors into the navigation solution.

5.5 Signal Processing Model

The signal processing model is a mathematical representation of the GPS receiver tracking loops which is based on a number of linearising approximations. The advantage of such a model over simulations is that it provides a deeper insight into the relationships between the parameters of both the scintillations and the tracking loops, and the expected loop performance. The principal disadvantage (and the reason for conducting simulations) is that it fails to take into account the non-linearities which are inherent in all tracking loops. Consequently, a combination of signal processing modelling and simulation is needed to provide a complete picture of receiver behaviour in a scintillation environment.

Figure 25 is an illustration of a generic GPS receiver in which the code and carrier tracking loops are shown embedded between an antenna / down-conversion stage and the navigation processor. Each tracking loop channel consists of a Costas Phase Locked Loop (PLL) for carrier tracking linked to a non-coherent Delay Locked Loop (DLL) for code tracking. In addition, the code loop is aided with Doppler corrections provided by the carrier loop to improve its robustness to dynamics¹. The mixer at the front of the code tracking loop is driven by a reference signal from the PLL and is responsible for down-converting the GPS Intermediate Frequency (IF) to a baseband digital signal. The mixer at the front of the carrier tracking loop is driven by the code estimate from the DLL and is responsible for stripping the PRN code from the IF carrier. The carrier signal produced at the output of the code mixer is modulated by navigation data and must be tracked with a suppressed carrier tracking loop such as a Costas PLL rather than an ordinary PLL.

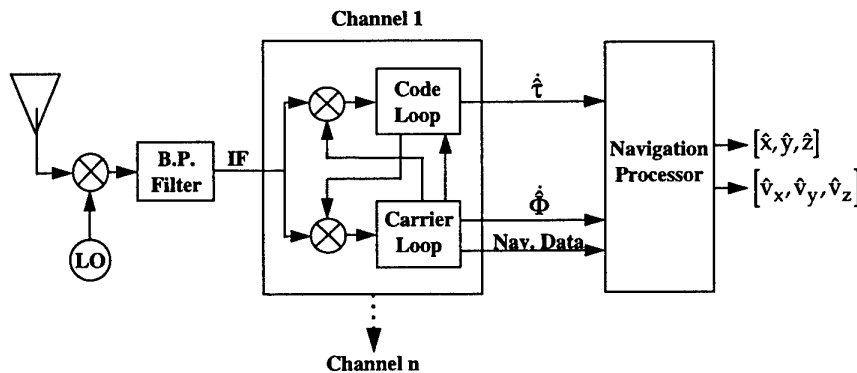


Figure 25: Architecture of a generic GPS receiver.

¹ Carrier aiding of the code loop is present in all GPS receivers.

Both the code and carrier tracking loops can be represented by the signal processing model illustrated in Figure 26. Here τ and Φ represent the phases of the code and carrier components of the IF signal at the input to the loop and $\hat{\tau}$ and $\hat{\Phi}$ represent the loop phase estimates. The loop contains two filters, a pre-detection filter $G(s)$ which reduces the levels of thermal noise prior to the non-linear phase discriminator, and a loop filter $F(s)$ which controls the order and bandwidth of the loop. The loop outputs are Doppler estimates $\dot{\hat{\tau}}$ and $\dot{\hat{\Phi}}$ which are integrated in the Navigation Processor to produce the code and carrier range estimates.

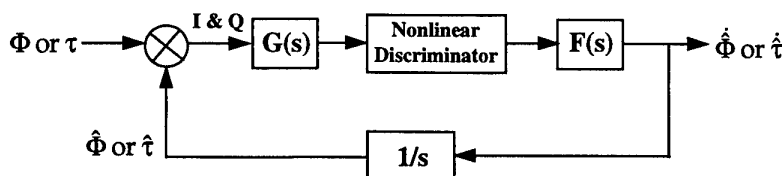


Figure 26: Signal processing model of a generic code or carrier tracking loop.

The function of the tracking loop is to measure the desired input phase process while rejecting phase noise. For GPS, the desired phase process is the Doppler introduced by satellite and receiver motion, while the phase noise is generated by a combination of thermal noise, multipath and scintillations. Important design objectives for the tracking loops are to minimise phase noise on the Doppler estimates, and to minimise the error between the input phase and estimated phase processes (ie $\tau_e = \tau - \hat{\tau}$ and $\Phi_e = \Phi - \hat{\Phi}$). This second objective is associated with the ability of the loop to remain in lock and is probably the most important of the two under extreme scintillation conditions.

The analysis which follows will concentrate on the effects of scintillations on the carrier tracking loop. It is assumed that delay jitter introduced by phase scintillations will have a more significant effect on the carrier tracking loop than the code tracking loop because of the much shorter wavelength on the carrier. In addition, the narrower bandwidth on the code tracking loop should improve its immunity to the SNR degradation's associated with amplitude scintillations. However, it is known that under conditions of very strong scintillation activity, frequency selective scintillation effects may cause distortion of the satellite PRN codes [44]. Such distortions would be likely to affect both the code and carrier tracking loops and will be the subject of future research.

Figure 27 is a representation of a Costas suppressed carrier tracking loop for tracking a data modulated carrier. The Costas loop generates In-phase (I) and Quadrature (Q) signals by mixing the GPS IF with an in-phase and quadrature reference from a Voltage Controlled Oscillator (VCO). The I & Q signals are then filtered by pre-

detection integrate and dump filters² and passed to a Costas phase discriminator to determine the phase errors.

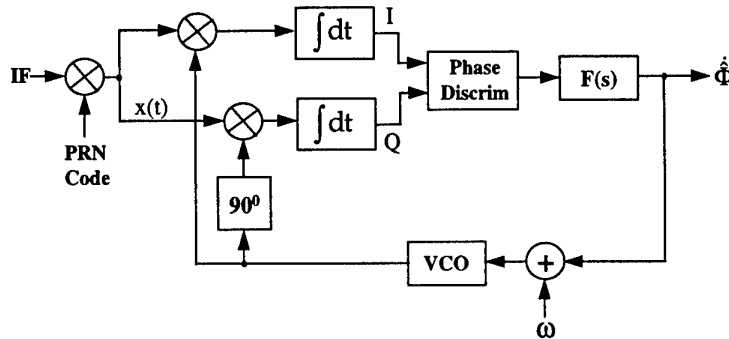


Figure 27: Representation of a generic Costas phase locked loop.

The function of the discriminator is to determine the error between the IF carrier phase and the VCO carrier phase while simultaneously removing the navigation data from the carrier. A list of the common discriminator algorithms along with their corresponding phase errors (as a function of the true phase error Φ_e) are given in Table 2 (a(t) is the signal amplitude).

Table 2: Common Phase Locked Loop Discriminators.

Discriminator	Phase Error
$Q \cdot \text{sign}(I)$	$a(t) \sin(\Phi_e)$
$Q \cdot I$	$a(t)^2 \sin(2\Phi_e)$
Q/I	$\tan(\Phi_e)$
$\text{atan2}(Q, I)$	Φ_e

Discriminator phase errors are then filtered by a loop filter $F(s)$ and passed to the VCO as corrections to the reference frequency. The loop filter controls the bandwidth and order of the tracking loop and must be adjusted according to the dynamic conditions in order to maintain optimum loop performance (minimum phase error).

In the following analysis, scintillations are modelled as a modulation of both the amplitude and phase of the GPS signal. Based on this model, the IF signal can be represented as follows:

² The integrate and dump filters are synchronised to the navigation data and have integration periods less than or equal to the length of a data bit. Without synchronisation, the SNR of the filtered I & Q signals would be significantly degraded.

$$IF = a(t)p(t - \tau)d(t - \tau)\sin(\omega t + \Phi(t)) + n(t),$$

where:

$a(t)$ is the signal amplitude (corrupted by amplitude scintillations),

$p(t - \tau)$ is the satellite PRN code with a time delay of τ seconds (± 1 bit stream),

$d(t - \tau)$ is the navigation message with a delay of τ seconds (± 1 bit stream),

ω is the GPS IF carrier frequency,

$\Phi(t) = \Phi_d(t) + \Phi_I(t) + \Phi_o(t)$ is the phase of the GPS carrier,

$\Phi_d(t)$ represents the effects of satellite and platform dynamics,

$\Phi_I(t)$ represents the effects of phase scintillations,

$\Phi_o(t)$ represents other effects (eg VCO phase noise), and

$n(t) = n_c(t)\cos(\omega t) + n_s(t)\sin(\omega t)$ is white Gaussian thermal noise

The IF signal is mixed with a replica PRN code from the code tracking loop to eliminate the code modulation $p(t - \tau)$ giving:

$$x(t) = a(t)d(t - \tau)\sin(\omega t + \Phi(t)) + n'(t),$$

where $n'(t) = n'_c(t)\cos(\omega t) + n'_s(t)\sin(\omega t)$ and $n'_c(t)$ and $n'_s(t)$ are uncorrelated, white Gaussian noise processes. Mixing with the I & Q references from the VCO and low-pass filtering through the pre-detection filters gives:

$$I = \tilde{a}(t)d(t - \tau)\cos(\Phi_e(t)) + n_I(t), \text{ and}$$

$$Q = \tilde{a}(t)d(t - \tau)\sin(\Phi_e(t)) + n_Q(t),$$

where $\tilde{a}(t)$ is a filtered version of the amplitude, $\Phi_e(t) = \Phi(t) - [\Phi_d(t) + \Phi_I(t) + \Phi_o(t)]$ is the phase error which is detected by the discriminator, and $n_I(t)$ and $n_Q(t)$ are uncorrelated baseband Gaussian noise processes. The Costas discriminator operates on the resultant I & Q signals to eliminate the navigation data and produce phase errors according to Table 2.

The Costas loop can be represented in an equivalent form in which the mixers and pre-detection filters are replaced by an adder and the phase discriminator is replaced by the equivalent phase error function. An example of this representation for the I.Q phase discriminator is given in Figure 28.

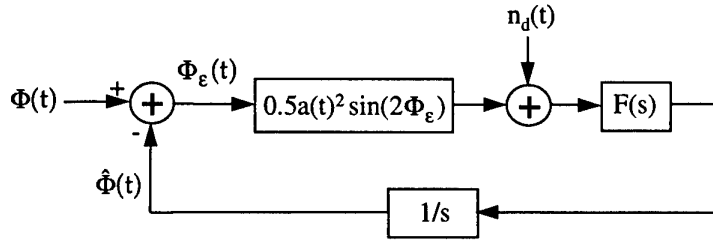


Figure 28: Non-linear model of an I.Q Costas Loop.

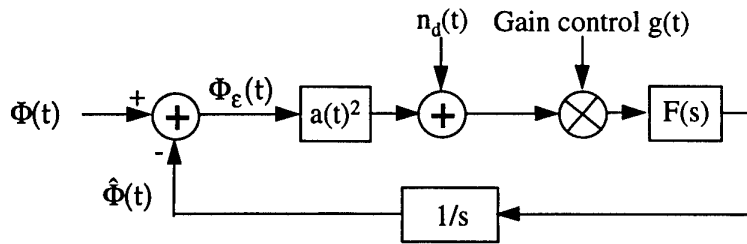


Figure 29: Linear model of an I.Q Costas Loop.

For small phase errors, the non-linear $\sin(\)$ function can be ignored leading to an entirely linearised phase model (Figure 29). The noise term $n_d(t)$ represents the effects of additive thermal noise translated to the discriminator output, and includes products between the I and Q signals and the incident thermal noise which are created within the discriminator. For the I.Q discriminator, $n_d(t)$ is given by:

$$n_d(t) = \tilde{a}(t)d(t - \tau)\cos(\Phi_\epsilon(t)) \cdot n_Q(t) + \tilde{a}(t)d(t - \tau)\sin(\Phi_\epsilon(t)) \cdot n_I(t) + n_Q(t) \cdot n_I(t)$$

The gain control $g(t)$ is typically provided by a post-detection AGC [42] and is necessary to ensure that I.Q or sign(I).Q loops operate within their design parameters. Without such control, the bandwidth and damping factor of the loops would be heavily influenced by the signal amplitude. For an I.Q discriminator, the AGC gain factor is given by $g(t) = 1/(I^2 + Q^2) = 1/\tilde{a}(t)^2$. If a normalised discriminator is used (such as Q/I or $\text{atan}(Q/I)$), or the AGC is assumed to track the signal strength fluctuations accurately, the closed loop transfer function of the Costas loop is given by:

$$H(s) = \frac{\hat{\Phi}(s)}{\Phi(s)} = \frac{F(s)}{s + F(s)}$$

Typical loop transfer functions for 1st order, 2nd order and 3rd order tracking loops are:

1st Order Loop

$$H(s) = \frac{\omega_n}{s + \omega_n},$$

2nd Order Loop

$$H(s) = \frac{2\zeta\omega_n s + \omega_n^2}{s^2 + 2\zeta\omega_n s + \omega_n^2},$$

3rd Order Loop

$$H(s) = \frac{2\omega_n s^2 + 2\omega_n^2 s + \omega_n^3}{s^3 + 2\omega_n s^2 + 2\omega_n^2 s + \omega_n^3},$$

where ω_n is the loop natural frequency (proportional to the loop noise bandwidth) and ζ is the damping factor for a second order loop. The power spectra of the phase errors and phase estimates can be found by applying the closed loop transfer function to the power spectra of the input phase processes as follows:

$$S_{\Phi_e}(\omega) = |1 - H(\omega)|^2 [S_{\Phi}(\omega)] + |H(\omega)|^2 S_n(\omega)$$

$$S_{\hat{\Phi}}(\omega) = |H(\omega)|^2 [S_{\Phi}(\omega)] + |H(\omega)|^2 S_n(\omega)$$

where $S_{\Phi}(\omega) = S_{\Phi_d}(\omega) + S_{\Phi_I}(\omega) + S_{\Phi_o}(\omega)$ and $S_{\Phi_d}(\omega)$, $S_{\Phi_I}(\omega) = T(\omega/2\pi)^{-P}$, $S_{\Phi_o}(\omega)$ and $S_n(\omega)$ are the power spectra of the dynamic phase process, ionospheric phase scintillations, other phase noise processes and thermal noise ($n_d(t)$) respectively. The variance of the phase error is thus:

$$\sigma_{\Phi_e}^2 = \frac{1}{2\pi} \int_{-\infty}^{\infty} S_{\Phi_e}(\omega) d\omega = \sigma_d^2 + \sigma_I^2 + \sigma_o^2 + \sigma_n^2$$

where σ_d^2 , σ_I^2 , σ_o^2 and σ_n^2 are the variances of the phase errors associated with dynamics, ionospheric phase scintillations, other phase noise sources and thermal noise respectively. The phase error variance $\sigma_{\Phi_e}^2$ is a measure of the error in the loop's estimate of the true carrier phase and is important for determining the probability of losing lock on the GPS signal.

The variance of the error in the dynamic phase process (ie. the error in the loop's estimate of the desired phase process $\Phi_d(t)$) is given by:

$$\sigma_{d_e}^2 = \frac{1}{2\pi} \int_{-\infty}^{\infty} [S_{\Phi_d}(\omega) - S_{\hat{\Phi}}(\omega)] d\omega$$

This is a measure of the error introduced into measurements of carrier phase range by phase scintillations and other sources. This is important in determining the impact of scintillations on the accuracy of GPS systems which use carrier phase range (such as carrier phase Differential GPS) and those which require precise velocity estimates.

In both cases, the thermal noise variance of an I.Q Costas PLL is given by ([5] pp 158):

$$\sigma_n^2 = \frac{1}{2\pi} \int_{-\infty}^{\infty} |H(\omega)|^2 S_n(\omega) \cdot d\omega = \frac{B_n}{C/N_o} \left[1 + \frac{1}{2TC/N_o} \right],$$

where:

$C/N_o = A^2/N_o$ is the Carrier to noise density ratio,

$A^2/2$ is the nominal signal power level,

$N_o/2$ is the power spectral density of the thermal noise $n_d(t)$,

T is the period of the integrate and dump filters,

$B_n = \sigma_{\Phi_e}^2 = \frac{1}{\pi_0} \int_{-\infty}^{\infty} |H(\omega)|^2 \cdot d\omega$ is the loop noise bandwidth.

The bracketed part of the expression is the squaring loss associated with the cross-products created within the I.Q discriminator. A modification to this expression for the case where amplitude scintillations are present is given by:

$$\sigma_n^2 = \frac{B_n}{C/N_o} \left[E \left\{ \frac{A^2}{\tilde{a}(t)^2} \right\} + \frac{1}{2TC/N_o} \cdot E \left\{ \frac{A^4}{\tilde{a}(t)^4} \right\} \right]$$

where $E\{ \}$ is the expectation operator. This assumes that the amplitude scintillations are uncorrelated with the thermal noise and a fast AGC is operating. As the level of amplitude scintillation activity increases, the two expectation terms also increase causing the thermal noise variance to increase. Although σ_n^2 is different for the other three Costas discriminators, it is never less than the thermal noise variance of a standard PLL (given by $B_n/(C/N_o)$).

The threshold for carrier tracking is based on the assumption that loss of lock will occur at a point near where the linearising approximations are significantly violated. If carrier phase noise is assumed to be Gaussian (as both the thermal noise and ionospheric phase scintillations are Gaussian), the probability of the phase error exceeding some threshold Φ_T is given by the Q function as follows:

$$\Pr[|\Phi_e(t)| > \Phi_T] = 2Q \left(\frac{\Phi_T}{\sigma_{\Phi_e}} \right)$$

If it is assumed that the loop will be significantly stressed when the linear approximation is in error by more than 5%, a phase error threshold of $\pi/6$ can be used

(ie $1 - \sin(\Phi_T)/\Phi_T = 0.05$). If it is also assumed that loss of lock will occur when the phase error threshold is exceeded more than 5% of the time, then the threshold phase error variance becomes

$$\sigma_{\Phi_e}^2|_{\text{Threshold}} = \left(\frac{\pi}{12}\right)^2$$

This threshold allows T and p values for the phase scintillation power spectrum to be defined which will result in loss of carrier lock. Factors which must be considered in this analysis include the bandwidth and order of the tracking loop, satellite and receiver motion and the presence of other sources of phase noise such as oscillator phase noise. In order to proceed, the following assumptions are made:

1. The satellite and receiver are stationary (ie $\Phi_d = 0$).
2. Amplitude scintillations are assumed to have no effect on the loop transfer function (ie either the AGC is capable of tracking the amplitude variations or a normalised discriminator is being used). Amplitude scintillations are accounted for as a factor F which scales the thermal noise variance (ie $\sigma_T^2 = \sigma_{T_{\text{no min al}}}^2 * F$ where $F \geq 1$).
3. No other phase noise sources are present.
4. The noise bandwidth of the carrier tracking loop never falls below 1Hz (a typical lower limit for GPS).

By equating the phase error threshold to the expression for phase error variance and taking account of the four assumptions above, an expression can be obtained which relates the phase scintillation parameters T and p to the scaling factor F and loop natural frequency ω_n . This can be represented as:

$$\sigma_{\Phi_e}^2(T, p, F, \omega_n) = \sigma_{\Phi_e}^2|_{\text{Threshold}}$$

In order to determine the optimum loop performance for a given loop order, the expression for the phase error variance can be minimised with respect to ω_n as follows:

$$\sigma_{\Phi_e}^2(T, p, F)|_{\min} = \sigma_{\Phi_e}^2|_{\text{Threshold}}$$

For a specific loop order, a threshold scaling factor F can be found as a function of the phase scintillation parameters T and p. In Figure 30, the threshold is plotted against T and p for a second order PLL. Similar thresholds can be obtained for first order and third order PLL's, although for reasons of loop stability the additional restriction of an upper limit on the noise bandwidth of 18Hz for third order PLLs must be applied. The lower plateau, which corresponds to a threshold fading level of 0dB, represents values of T and p for which the loop will be forced out of lock without amplitude scintillations. Scintillations in this region will therefore have very detrimental effects on loop performance, irrespective of the loop bandwidth. The upper plateau, corresponding to a threshold fading level of 32dB, represents the values of T and p for which an optimised loop will suffer negligible phase scintillation stress.

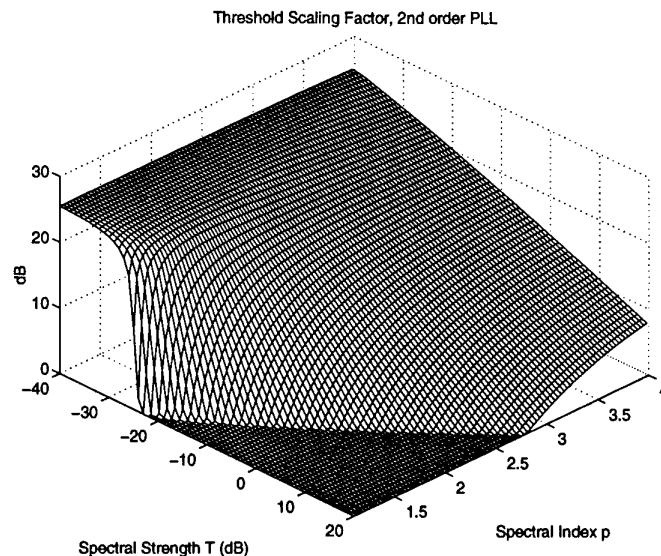


Figure 30: Threshold noise scaling factor as a function of the spectral index p and spectral strength T for a second order PLL. The loop has been optimised for minimum phase error variance at each value of T and p .

GPS receivers will in general choose the bandwidth and order of their tracking loops according to the actual or anticipated dynamic conditions, and not to the levels of phase and amplitude scintillation. Consequently, for typical GPS receiver tracking loop bandwidth's, the threshold curve is expected to be much worse. The next step in this analysis is to associate the threshold T & p values with probabilities of occurrence based on a scintillation model such as WBMOD.

The analysis so far has only been at a preliminary level. Further investigation will be needed into the following areas:

- An investigation into the errors associated with the linearising approximations.
- An analysis of the acquisition performance of receivers in the presence of scintillation activity.
- The impact of other non-linear elements such as the AGC.
- The impact of non-stationary scintillation statistics on loop performance.

5.6 Impact of Scintillations on Jamming Immunity

Simple jamming signals such as single tone CW, FM CW, FM and AM noise raise the noise floor of the GPS signal at the input to the carrier tracking loop. Although pulse jamming behaves in a similar way, it tends to be less effective because of the AGC and peak clipping circuits employed in the front ends of GPS receivers. A more thorough analysis of the susceptibility of GPS to simple jamming waveforms is given in [45].

A single tone CW jammer centred on the GPS carrier is spread to a wide-band signal after mixing with the receiver's locally generated replica PRN ranging code. The envelope of the resulting jammer power spectrum is given by the following expression [45]:

$$S_J(f) = \frac{P_{JR}}{f_c} \left(\frac{\sin\left(\frac{\pi(f-f_J)}{f_c}\right)}{\pi(f-f_J)/f_c} \right)^2,$$

where:

f_c = the chipping rate of the PRN code

= 1.023×10^6 for the C/A-Code

= 10.23×10^6 for the P(Y)-Code,

P_{JR} = The jammer power level at the receiver,

f_J = The frequency of the tone jammer.

f = Frequency,

For a CW jammer centred on the GPS L1 frequency, the power spectral density near L1 is given by:

$$S_{JL1}(f) = P_{JR}/f_c$$

For a thermal noise power spectral density of $N_o/2$ at the input to the carrier tracking loop, the total noise power spectral density from all additive noise sources at frequencies near to GPS L1 is:

$$N_o/2 + P_{JR}/f_c$$

Consequently, the equivalent carrier to noise density ratio is given by (Ward, pp 220 [5]):

$$C/N_{oJ} = \frac{A^2/2}{N_o/2 + P_{JR}/f_c} = \frac{1}{\frac{1}{C/N_o} + \frac{J/S}{f_c}},$$

where C/N_o is the un-jammed carrier to noise density ratio and J/S is the jammer to signal power ratio. The total variance from thermal noise and jamming sources is therefore (Ward, pp 158 [5]):

$$\sigma_{J+T}^2 = \frac{B_n}{C/N_{oJ}} \left[1 + \frac{1}{2TC/N_{oJ}} \right]$$

where B_n is the noise bandwidth of the carrier tracking loop. The total phase error variance resulting from all noise sources is thus:

$$\sigma^2 = \sigma_d^2 + \sigma_I^2 + \sigma_o^2 + \sigma_{J+T}^2$$

where σ_d^2 , σ_I^2 and σ_o^2 are the phase error variances associated with dynamics, ionospheric phase scintillations and other phase noise sources (eg oscillator phase noise) respectively. If a threshold variance of $(\pi/12)^2$ is assumed (based on the analysis given earlier), then a threshold value for σ_{J+T}^2 can be defined as follows:

$$\sigma_{J+T}^2|_{Th} = (\pi/12)^2 - \sigma_d^2 - \sigma_I^2 - \sigma_o^2$$

If only jamming, thermal noise and ionospheric scintillation effects are considered, this expression reduces to:

$$\sigma_{J+T}^2|_{Th} = (\pi/12)^2 - \sigma_I^2$$

Combining this with the expression for the thermal noise plus jammer variance gives:

$$C/N_{oJ}|_{Th} = \frac{B_n}{2\sigma_{J+T}^2|_{Th}} \left[1 + \sqrt{1 + \frac{2\sigma_{J+T}^2|_{Th}}{TB_n}} \right]$$

From the expression for the equivalent carrier to noise density ratio, the threshold jammer power level at the receiver is:

$$P_{JR}|_{Th} = f_c \left[\frac{A^2}{2C/N_{oJ}|_{Th}} - N_o/2 \right]$$

This can be converted into an equivalent transmitted jammer power level by applying the equation for the propagation of electromagnetic waves in free space [45]:

$$P_{JR} = P_{JT} \cdot G_{JT} \cdot G_{JR} \cdot \left(\frac{\lambda}{4\pi d} \right)^2$$

where:

- P_{JT} = Transmitted power level of the jammer,
- G_{JT} = Gain of the transmitting antenna (jammer),
- G_{JR} = Gain of the receiving antenna (GPS receiver),
- d = the range to the jammer,
- λ = Free space wavelength (0.190m: GPS L1, 0.244m: GPS L2).

The threshold transmitted jammer power level is therefore:

$$P_{JT}|_{Th} = \frac{(4\pi d)^2 P_{JR}|_{Th}}{\lambda^2 \cdot G_{JT} \cdot G_{JR}}$$

$$= \frac{(4\pi d)^2 f_c}{\lambda^2 \cdot G_{JT} \cdot G_{JR}} \left[\frac{A^2 \left((\pi/12)^2 - \sigma_I^2 \right)}{B_n \left[1 + \sqrt{1 + 2 \left((\pi/12)^2 - \sigma_I^2 \right) / (TB_n)} \right]} - N_o/2 \right]$$

The threshold jammer power level can be plotted as a function of the ionospheric phase scintillation parameters, T and p , for a specific range d if the following assumptions are made:

1. f_c is fixed (eg 1.023×10^6 for the C/A-Code),
2. λ is fixed (eg $0.190m$ for the C/A-Code),
3. G_{JT} and G_{JR} are fixed (eg 1 for isotropic radiators),
4. The GPS signal level is fixed (eg $A^2/2 = -160dBW$ for the C/A-Code),
5. Amplitude scintillation effects are ignored ($a(t)=A$ which is a constant),
6. No other sources of phase noise exist ($\sigma_o^2 = 0$),
7. The receiver is stationary ($\sigma_d^2 = 0$),
8. The loop order is fixed (eg a 2nd order loop).

The analysis would result in different threshold jammer power levels if any of these assumptions were changed.

In Figure 31, the threshold transmitted jammer power level is plotted as a function of the scintillation spectral parameters T and p for a range of 50km (based on the assumptions listed above). In panel (a) a 10Hz noise bandwidth was used, in panel (b) a 2Hz noise bandwidth was used. It is apparent from Figure 31 that the wider bandwidth receiver is more tolerant to phase scintillations, but less tolerant to jamming (ie it can tolerate larger values of T representing stronger scintillation activity, but its threshold jammer power level in the absence of scintillations is much lower). Consequently, an optimum bandwidth will exist as a function of T , p and jammer strength which will minimise the combination of these two error sources. Panel (a) represents a bandwidth which is typical of an unaided GPS receiver, while panel (b) represents a bandwidth typical of an INS aided receiver. Consequently, although INS aiding minimises the effects of jamming by allowing a reduction in the tracking loop bandwidth, it has the reverse effect on phase scintillations.

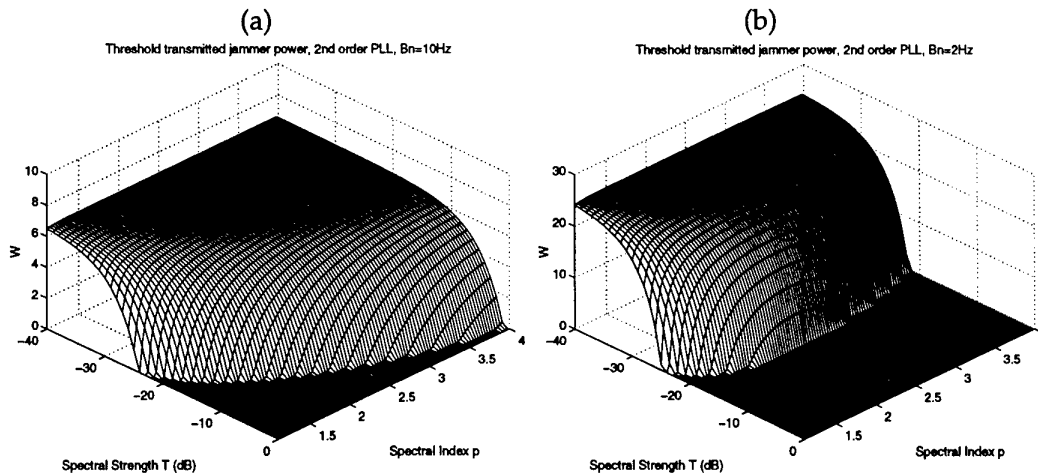


Figure 31: Threshold transmitted jammer power level for a 2nd order Costas PLL at a range of 50km as a function of the spectral strength (T) and spectral index (p) of phase scintillations. Panel (a) represents a bandwidth of 10Hz, panel (b) represents a bandwidth of 2Hz.

5.7 Impact of Scintillations on Navigational Accuracy

Although scintillations can have a significant impact on the performance of individual tracking loops, the overall navigational performance of a receiver will depend upon a number of factors, including:

- The number of satellites affected by the large-scale structure of the irregularities.
- The intensity and type of scintillation activity and their resultant effect on the individual tracking loops.
- The geometry and density of the satellite constellation and the distribution of the affected versus unaffected satellites.
- Masking angles and the gain pattern of the receiver antenna.
- Aiding by secondary navigation systems such as INS.
- The satellite selection algorithms used by the individual receivers.

It has already been demonstrated that scintillation activity can introduce perturbations into the GPS signals at a level that results in a significant increase in the phase-noise and/or pseudorange errors observed by the receivers. Moreover, it has also been shown that severe scintillations can produce perturbations large enough to cause the carrier tracking loops of a receiver to lose lock. Depending upon the extent of the large-scale structure of the ionospheric irregularities, therefore, the navigational accuracy will be degraded in accordance with the poorer GDOP that results from the now degraded constellation geometry.

In the analysis that follows it was assumed that the scintillation activity extended in two bands centred on the anomaly crests³ and covering a region of about 1600 km North-South (approximately 15° in latitude). In addition, the region of scintillation activity was assumed to be confined to the height range of 300 km to 600 km at all latitudes within these bands. It was also assumed that the scintillation activity was such that any signals passing through these structures could not be tracked by the GPS receivers. Initially, this may seem a rather harsh assumption. However, once a receiver has lost lock on the incoming signal it generally struggles to re-acquire it, at least for the duration of the scintillation activity.

Two scenarios were considered; i) a 100km wide irregularity in both the Northern and Southern latitude bands, and ii) a group of three 100km wide irregularities separated by about 400km in each band. These scenarios were based on observations of the width's of irregularity patches made by Ossakow et al [32] and of the separations of irregularity patches made by Tsunoda et al [47].

The effects of the irregularity patches on the available satellite geometry was found by cycling the constellation through 24 hours in 5 minute steps over a large number of geographic locations and determining the resultant Horizontal Dilution of Precision (HDOP). At each location, the centres of the irregularity patches were aligned with the longitude of the location. HDOP was then combined with a typical User Equivalent Range Error (UERE) to obtain 2 σ estimates of the horizontal accuracy. This procedure was repeated at locations separated by 0.5 degrees in both latitude and longitude over a region covering both Australia and South East Asia.

Figure 32 is a plot of the 90th percentile⁴ of the 2 σ horizontal accuracy (in metres) for a C/A-code GPS receiver in the presence of a single, 100km wide irregularity patch in each anomaly band. A constellation of 24 satellites is assumed and the mask angle of the antenna is set to 0°. The figure is scaled such that a horizontal accuracy worse than approximately 1000m is considered to be equivalent to an outage (ie. less than 4 satellites available). The dotted line in the centre of the page shows the approximate location of the geomagnetic equator and the two lines either side of the equator represent the extent of the anomaly region.

³ The large-scale ionospheric irregularities often extend across the magnetic equator from one anomaly crest to the other (assumed to be located at $\pm 12.5^\circ$ magnetic). However, the severest scintillation activity is usually confined to the regions around the anomaly peaks where the ionospheric gradients are greatest [34], [31].

⁴ The 90th percentile refers to the error which is exceeded only 10% of the time.

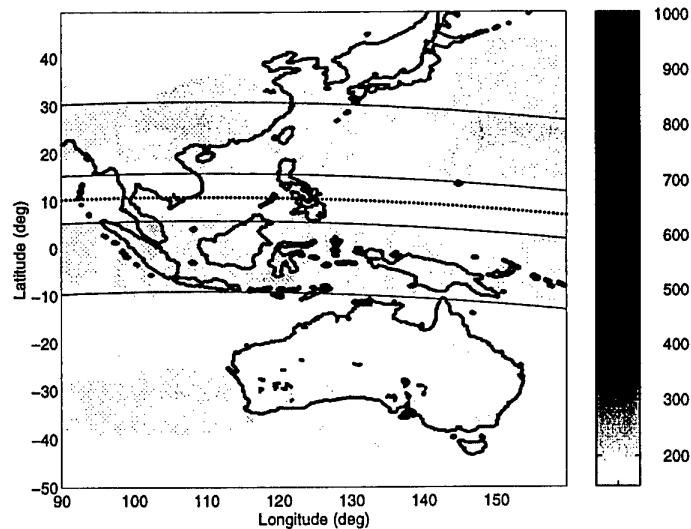


Figure 32: C/A-code navigational accuracy (m) at the 90th percentile in the presence of a pair of 1600km by 100km irregularities centred on the crests of the equatorial anomaly (24 satellites, 0° elevation mask).

It is clear from this figure that for an aircraft at moderate altitude (mask angle 0°), a fully operational GPS satellite constellation (24 satellites), and a single ionospheric disturbance of the type described above, that the overall impact on GPS navigation is relatively minor. In other words, the probability of outages is both small and restricted to specific regions of the world. If, however, the mask angle is increased (i.e. the aircraft is at a lower altitude or the receiver is ground based), the constellation is operating at less than its full complement of satellites (eg. the minimum operational constellation of 21), or the local terrain obscures the antennas view of the constellation, the impact becomes much more pronounced and significant degradations in accuracy can occur in the regions of severest scintillation activity (Figure 33). This is particularly pronounced in areas where the crests of the equatorial anomaly are significantly removed from the geographic equator. This is because the satellite geometry and coverage provided by the GPS constellation degrades as the latitude increases. In the AAI, the Northern anomaly crest is approximately 20° further removed from the geographic equator than the Southern anomaly crest. Consequently, the impact of scintillations on navigational accuracy is expected to be worse in the Northern hemisphere than in the Southern hemisphere. This situation is reversed on the opposite side of the Earth (in the American/Atlantic sector). However, even under these conditions, the probability of an outage is extremely small.

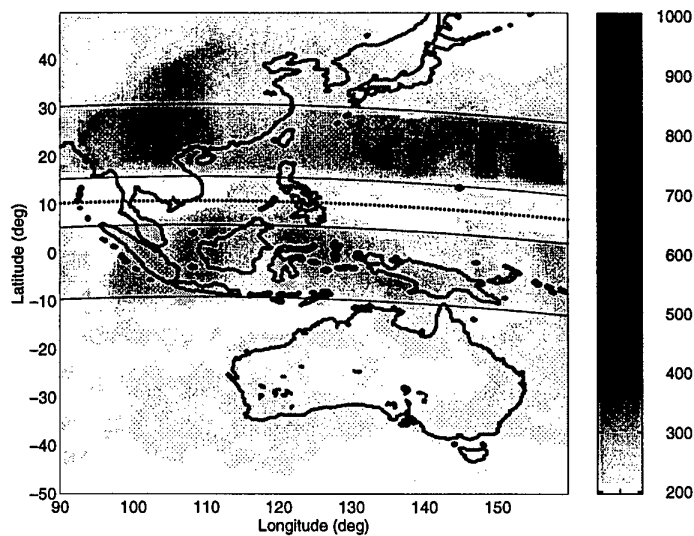


Figure 33: C/A-code navigational accuracy (m) at the 90th percentile in the presence one 1600km by 100km ionospheric irregularity centred on the crests of the equatorial anomaly (21 satellites, 5° mask)

The worst scintillation activity is typically confined to the hours following sunset and before midnight during the (local) winter months of the solar maximum. Considering the scintillation activity to occur at any time of the day, therefore, is equivalent to assuming that the scintillation activity can occur on any day of the year⁵. Consequently, the figures provide a measure of the accuracy levels that will be exceeded as a percentage of the time when the scintillation activity is present rather than as a percentage of the whole day. Again, however, the distribution is shown at the 90th percentile indicating that prudent mission planning may be sufficient to avoid significant impact on GPS dependent operations.

The effect of increasing the number and/or large-scale structure of the ionospheric disturbances, however, has a very significant impact on the accuracy and potential for outages. Figure 34 (a) shows the navigational accuracy (at the 90th percentile) in the presence of three 1600km long, 100km wide irregularity patches, centred on the anomaly regions and separated by 400km. A mask angle of 5° (typical) and a 24 satellite constellation is assumed. Figure 34 (b) shows the total time with less than four⁶ satellites over a 24 hr period under the same conditions.

⁵ The difference between the length of a solar and a sidereal day means that the effective time at which the scintillation activity will occur in sidereal (i.e. satellite) time shifts by about 4 minutes each day.

⁶ Four satellites are required for an accurate 3d position fix.

Clearly, the duration of the potential outages which are possible in the presence of this type of ionospheric activity merit more cautious mission planning, particularly if the constellation is not at its full strength, some of the satellites are obscured, or the mask angle is greater than 0° .

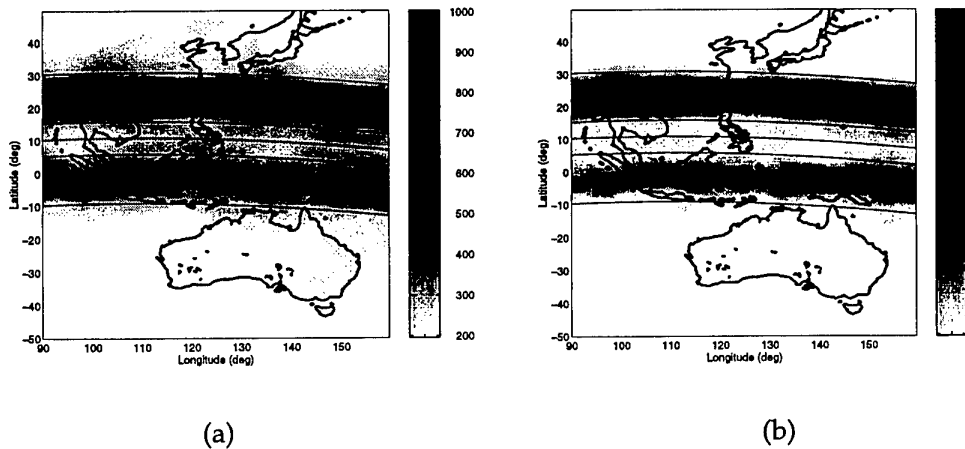


Figure 34: C/A-code navigational accuracy at the 90th percentile (a) and the total time with less than 4 satellites (b) in the presence of three ionospheric irregularities at 400 km intervals (24 satellites, 5° mask).

Scintillation activity which is not severe enough to cause loss of lock but is still capable of introducing range measurement errors is also likely to degrade navigational accuracy. However, this will only become a problem when the magnitude of the additional range measurement error approaches the largest error source contributing to UERE. For example, for a stand alone SPS C/A-Code receiver, the rms range error resulting from scintillations would need to exceed 33m in order to have a significant effect on navigational accuracy (ie comparable to the SA range error - Table 1). However, for carrier phase DGPS systems, this error need only be at the mm level in order to exceed the thermal noise and multipath errors in the carrier tracking loop.

This analysis represents a relatively crude attempt to determine the extent to which the large scale structure of the ionosphere effects navigational accuracy. The WBMOD model, when linked to an appropriate receiver model, has the capacity to provide information about the degradation in UERE and probability of loss of lock on each of a number of satellite links. By combining this information with the satellite geometry, more accurate predictions of the likely impact of scintillations on navigational accuracy can be made. Future research will be directed in this area.

6. Conclusions

The impact of the benign ionosphere on GPS equipment owned and operated by the ADO is considered to be minimal because the positional accuracy of receivers will be driven by operational requirements. Consequently, in situations where high accuracy is not needed, a single frequency C/A-Code receiver can be used. However, if higher levels of accuracy are required, dual frequency P(Y)-Code or DGPS techniques can be used. The benign ionosphere will, however, have an impact on the accuracy of carrier phase DGPS systems over long baselines, particularly at equatorial latitudes where TEC gradients can be large. Equatorial gradients can also reduce the accuracy of WADGPS if the separation between reference stations is too large.

With the probable introduction of an L5 channel for civilian users, suitably equipped stand-alone SPS receivers will be capable of removing the majority of the errors resulting from the benign ionosphere. Consequently, the effects of the benign ionosphere on GPS are likely to become even less important in the future.

Unlike the benign ionosphere, the disturbed ionosphere is capable of affecting all GPS systems including stand-alone and differential systems, single frequency and dual frequency receivers. Scintillations act on the tracking loops of a GPS receiver directly, and so their effects cannot be eliminated by simply processing the pseudorange observables. Strategies for mitigating their effects might involve the use of alternative tracking loop architectures, loop optimisation techniques, and careful mission planning using scintillation forecasting tools. The effects of scintillations on GPS include an increase in carrier phase measurement noise, carrier cycle slips, and, under extreme conditions, a complete loss of signal lock. All of these effects translate into degraded navigational accuracy and an increase in the jamming susceptibility of receivers.

The susceptibility of a receiver to scintillation activity is dependant on many factors, including the tracking loop bandwidth, the loop order, the characteristics of the scintillations, platform dynamics and the presence of INS aiding. Initial tests conducted on a GPS tracking loop simulator using scintillation data derived from a simple diffraction model suggests that wide bandwidth receivers are much more tolerant to scintillations than narrow bandwidth receivers. Also, the additional stresses experienced by tracking loops under dynamic conditions tend to increase a receiver's susceptibility to scintillations. However, in many cases a narrow bandwidth receiver in a highly dynamic environment is likely to be aided by INS. This will significantly reduce the dynamic stresses experienced by the receiver as well as allowing it to re-acquire very rapidly once the scintillation activity has passed.

Analysis of receiver tracking loops using signal processing models have provided expressions which link the spectral characteristics of scintillations to the performance of the loop. These expressions allow scintillation models such as WBMOD to be used to provide predictions of the magnitude of errors and the probability of loss of lock for

a tracking loop. Expressions are also derived which relate the scintillation spectral parameters to the jammer power level required to force a loop out of lock. These expressions show that a reduction in tracking loop bandwidth will reduce the effects of jamming and amplitude scintillations, but will increase the effects of phase scintillations. Consequently, an optimum bandwidth will exist which minimises tracking loop errors and therefore minimises the probability of loss of lock.

The overall impact on a receiver's navigational accuracy is highly dependent upon both the large scale and the small scale structure of the irregularities within the ionosphere. Initial results using a highly simplified model of the irregularity structures suggest that the presence of several large irregularities can cause outages in some regions of the world of up to 30-40% of the time that the phenomena are present. On the other hand, if the structures occur singly, are restricted primarily to the crests of the equatorial anomaly and the GPS constellation is operating with its full complement of satellites, the impact on navigation appears to be relatively minor, even if the disturbances are relatively severe.

The receivers which are most likely to be affected by scintillations are those that use carrier phase DGPS techniques. Many of these receivers may well become unusable in their most accurate positioning modes, even over extremely short baselines (100m or so) and in the presence of relatively minor scintillation activity.

It is clearly important to develop an improved understanding of the temporal and spatial distributions of both the large scale and the small scale structure of ionospheric irregularities. The small scale structure will allow us to determine the extent to which individual receivers are susceptible to scintillation activity, while the large scale structure will provide information about coverage which will allow the overall impact on navigation to be assessed.

7. Future Directions

The main thrust of future research will be in the following areas:

1. TSSD: Investigating the increased susceptibility of GPS receivers to electromagnetic interference in the presence of scintillations. The intention is to combine research into the impact of jamming on GPS with research into scintillation effects so that a unified picture of receiver susceptibility can be formed. The results of this work will be used to support operational studies into the performance of various GPS systems within the ADO.
2. WASD: The development of predictive models of scintillation activity within the AAI. These models will provide predictions of the occurrence and intensity of scintillation activity at a given geographic location and time. As part of this study, a number of GPS receivers are to be deployed in South East Asia to provide measurements of TEC and scintillation activity which can be used to validate and enhance existing scintillation models. These models will be useful in the evaluation

of scintillation effects on other spaced based assets such as communications systems and spaced based infrared systems.

3. TSSD: Investigating techniques to mitigate or minimise the impact of scintillations on GPS should it prove necessary. This may involve the use of alternative, more resilient tracking loop techniques, optimising the performance of existing tracking loops, and perhaps filtering carrier phase range measurements to minimise errors for carrier phase DGPS.

The flowchart in Figure 35 illustrates the relationship between the various research activities within DSTO which are associated with the study of scintillation effects on GPS. WASD are responsible for the development of suitable scintillation models which will provide statistics on the occurrence and intensity of scintillation activity in the region. Information from this model will be used to generate time domain data which, along with information on thermal noise and dynamics, will be passed to the GPS system simulator. Output from the simulator will include code and carrier phase pseudorange measurement errors and tracking state for a single satellite link. The impact of tracking loop bandwidth, loop order and alternative tracking loop techniques on the tolerance to scintillations can be readily tested on the simulator. A signal processing model of a generic tracking loop will be used to relate the statistical parameters of the scintillations with the expected range measurement errors and probabilities of loss of lock. Performance measures for a single receiver channel obtained through both simulation and modelling will be combined with information on the probability and distribution of scintillation activity and the geometry of the satellite constellation to determine the impact on navigational accuracy. All simulation data will be cross-compared with observations made using DSTO's new satellite navigation simulator.

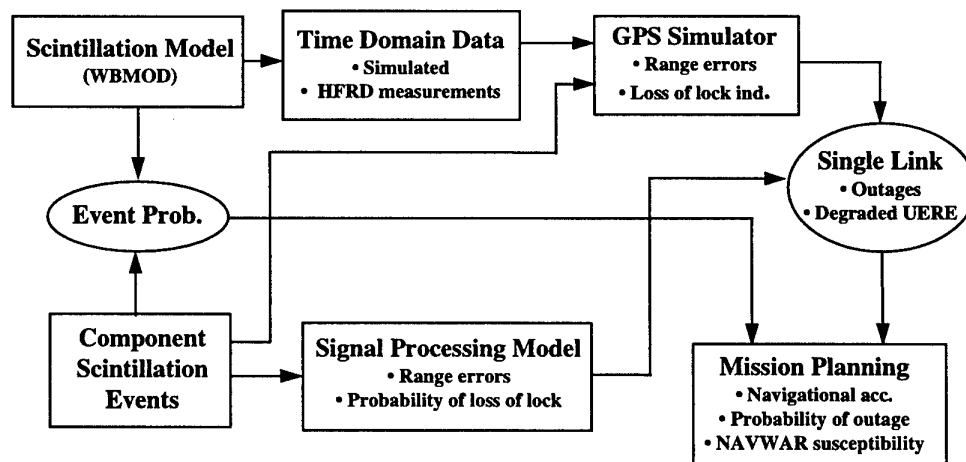


Figure 35: Flowchart illustrating the various activities associated with research into scintillation effects on GPS within TSSD/WASD.

8. Acknowledgments

The authors would like to thank Dr Chris Coleman and Dr Dick Thomas of WASD for their advice on ionospheric modelling and scintillation activity and Prof Douglas Gray of the Cooperative Research Centre for Sensor Signal and Information Processing (CSSIP) for his advice in the application of signal processing techniques to the analysis of tracking loop performance.

1. References

- [1] Klobuchar, J. A., "Ionospheric Time-Delay Algorithm for Single-Frequency GPS Users", IEEE Transactions on Aerospace and Electronic Systems, Vol. AES-23, No. 3, 1987.
- [2] Counselman, C., U.S. Patent numbers 4,667,203 and 4,894,662.
- [3] Ashjaee, J., Lorenz, R., "Precision GPS Surveying After Y-Code", Proceedings of ION GPS-92, Fifth International Technical Meeting of the Satellite Division of the Institute of Navigation, 1992.
- [4] Milliken, R. J., Zoller, C. J., "Principle of Operation of NAVSTAR and System Characteristics", Global Positioning System - Papers published in NAVIGATION, The Institute of Navigation, Vol. 1, 1980.
- [5] Kaplan, E. D., "Understanding GPS: Principles and Applications", Mobile Communications Series, Artech House, 1996.
- [6] Rishbeth, H., "Basic physics of the ionosphere: a tutorial review", Journal of the Institution of Electronic and Radio Engineers, Vol. 58, No. 6, 1988.
- [7] Kelly, M. C., "The Earth's Ionosphere; Plasma Physics and Electrodynamics", Vol. 43, International Geophysics Series, Academic Press Inc., 1989.
- [8] Davies, K., "Ionospheric Radio", Vol. 31, IEE Electromagnetic Waves Series, Peter Peregrinus Ltd., 1990.
- [9] Divis, D. A., "The Year Ahead for GPS Policy", GPS World, Jan. 1997.
- [10] News Release 095-97, Office of Assistant Secretary of Defense (Public Affairs), United States Department of Defense, Feb. 1997.
- [11] Llewellyn, S. K., Bent, R. B., "Documentation and Description of the Bent Ionospheric Model", Air Force Cambridge Research Laboratories Technical Report AFCRL-TR-73-0657, 1973.
- [12] Feess, W. A., Stephens, S. G., "Evaluation of GPS Ionospheric Time-Delay Model", IEEE Transactions on Aerospace and Electronic Systems, Vol. AES-23, No. 3, 1987.
- [13] Knight, M. F., Gray, D. A., "Maximum Likelihood Estimation of Ionospheric Total Electron Content Using GPS", ISSPA 96 - Fourth International Symposium on Signal Processing and its Applications, 1996.
- [14] Finn R. A., "The Effect of the Ionosphere on Satellite Position Fixing", PhD thesis, Jesus College, Cambridge, 1989.
- [15] Jorgensen, P. S., "An Assessment of Ionospheric Effects on the GPS User", Journal of the Institute of Navigation, Vol. 36, No. 2, 1989.
- [16] El-Arini, M. B., O'Donnell, P., Kellam, P., Klobuchar, J. A., Wisser, T. C., Doherty, P. H., "The FAA Wide Area Differential GPS (WADGPS) Static Ionospheric Experiment", The ION National Technical Meeting, 1993.
- [17] El-Arini, M. B., Hegarty, C. J., Fernow, J. P., Klobuchar, J. A., "Development of an Error Budget for a GPS Wide-Area Augmentation System (WAAS)", The ION National Technical Meeting, 1994.
- [18] Hakegard, O. P., "A Real Time Ionospheric Model for Use in a WADGPS System", The ION National Technical Meeting, 1994.

- [19] Casewell, I. E., Basker, G. A., Norse, E. T., Hein, G. W., Hekegard, O. P., "A European Wide Area DGPS Experiment: Overview and Initial Results", Proceedings of ION GPS-93, Sixth International Technical Meeting of the Satellite Division of the Institute of Navigation, 1993.
- [20] Bishop, G. J., Klobuchar, J. A., "Multipath effects on the determination of absolute ionospheric time delay from GPS signals", Radio Science, Volume 20, No. 3, 1985.
- [21] Wilson, B. D., Mannucci, A. J., "Instrumental Biases in Ionospheric Measurements Derived from GPS Data", Proceedings of ION GPS-93, Sixth International Technical Meeting of the Satellite Division of the Institute of Navigation, 1993.
- [22] Coco, D. S., Coker, C., Dahlke, S. R., Clynch, J. R., "Variability of GPS Satellite Differential Group Delay Biases", IEEE Transactions on Aerospace and Electronic Systems, Vol. 27, No. 6, 1991.
- [23] Lanyi, G. E., Roth, T., "A comparison of mapped and measured total ionospheric electron content using global positioning system and beacon satellite observations", Radio Science, Vol. 23, 1988.
- [24] Bishop, G. J., Coco, D. S., Kappler, P. H., Holland, E. A., "Studies and Performance of a New Technique for Mitigation of Pseudorange Multipath Effects in GPS Ground Stations", Proceedings of the 1994 National Technical Meeting of the Institute of Navigation, 1994.
- [25] Klobuchar, J. A., "Ionospheric Effects on GPS", Innovation, GPS World, April 1991.
- [26] Bishop, G. J., Bullett, T. W., Holland, E. A., "GPS Measurements of L-Band Scintillation and TEC in the Northern Polar Cap Ionosphere at Solar Maximum", Proceedings of the International Beacon Satellite Symposium, Aberystwyth, UK, 1994.
- [27] Klobuchar, J. A., "Global Positioning System: Theory and Applications Volume I", Progress in Astronautics and Aeronautics, Vol 163, pp 485-514, 1995.
- [28] Aarons, J. A., Basu, S., "Ionospheric Amplitude and Phase Fluctuations at the GPS Frequencies", Proceedings of ION GPS-94, Seventh International Technical Meeting of the Satellite Division of the Institute of Navigation, 1994.
- [29] Aarons, J. A., et al, "Gigahertz scintillations associated with equatorial patches", Radio Science, Vol. 18, No. 3, 1983.
- [30] Basu, S., MacKenzie, E., Basu, S., "Ionospheric constraints on VHF/UHF communications links during solar maximum and minimum periods", Radio Science, Vol. 23, No. 3, 1988.
- [31] Basu, S., Basu, S., "Equatorial scintillations - a review", Journal of Atmospheric and Terrestrial Physics, Vol. 43, No 5/6, 1981.
- [32] Ossakow, S. L., Chaturvedi, P. K., "Morphological studies of rising equatorial spread F bubbles", Journal of Geophysical Research, Vol. 83, 1978.
- [33] Spatz, D. E., Franke, S. J., Yeh, K. C., "Analysis and interpretation of spaced receiver scintillation data recorded at an equatorial station", Radio Science, Vol. 23, No. 3, 1988.
- [34] Aarons, J. A., et al, "Microwave equatorial scintillation intensity during solar maximum", Radio Science, Vol. 16, No. 5, 1981.
- [35] Wanninger, L., "Effects of the Equatorial Ionosphere on GPS", Innovation, GPS World, July 1993.
- [36] Titheridge, J. E., "The diffraction of satellite signals by isolated ionospheric irregularities", Journal of Atmospheric and Terrestrial Physics, Vol. 33, 1971.

- [37] Davies, K., Whitehead, J. D., "A radio lens in the ionosphere", *Journal of Atmospheric and Terrestrial Physics*, Vol. 39, 1977.
- [38] Bishop, G., et al, "GPS Applications to Global Ionospheric Monitoring: Requirements for a Ground-Based System", *Proceedings of ION GPS-92, Fifth International Technical Meeting of the Satellite Division of the Institute of Navigation*, 1992.
- [39] Fremouw, E. J., Livingston, R. C., Miller, D. A., "On the statistics of scintillating signals", *Journal of Atmospheric and Terrestrial Physics*, Vol. 42, 1980.
- [40] Secan, J. A., Bussey, R. M., Fremouw, E. J., "An improved model of equatorial scintillations", *Radio Science*, Vol. 30, No. 3, 1995.
- [41] "Handbook of Geophysics and the Space Environment", Air Force Geophysics Laboratory, USAF.
- [42] Van Dierendonck, A. J., "Global Positioning System: Theory and Applications Volume I", *Progress in Astronautics and Aeronautics*, Vol 163, pp 329-405, 1995.
- [43] Knight, M. F., Finn, A., "Ionospheric Scintillation Effects on GPS Performance", *Proceedings of ION GPS-96, Ninth International Technical Meeting of the Satellite Division of the Institute of Navigation*, 1996.
- [44] Bogusch, R. L., Guigliano, F. W., Knepp, D. L., "Frequency-Selective Scintillation Effects and Decision Feedback Equalization in High Data-Rate Satellite Links", *Proceedings of the IEEE*, Vol. 71, No. 6, 1983.
- [45] Knight, M. F., "Global Positioning System Receiver Interference Evaluation", DSTO Technical Report No. DSTO-TR-0445, 1996.
- [46] Rockwell International Corporation, Satellite Systems Division, "ICD-GPS-200, NAVSTAR GPS Space Segment / Navigation User Interfaces", 1987.
- [47] Tsunoda, R. T., Livingston, R. C., "Equatorial Plasma Bubbles: Vertically Elongated Wedges From the Bottomside F Layer", *Journal of Geophysical Research*, Vol. 87, No. A11, 1982.
- [48] Briggs, B. H., Parkin, I. A., "On the variation of radio star and satellite scintillations with zenith angle", *Journal of Atmospheric and Terrestrial Physics*, Vol. 25, 339-366, 1962.
- [49] Buckley, R., "Diffraction by a random phase screen with very large RMS phase deviation: 1. One-dimensional screen", *Australian Journal of Physics*, Vol. 24, 351-371, 1971a.
- [50] Buckley, R., "Diffraction by a random phase screen with very large RMS phase deviation: 2. Two-dimensional screen", *Australian Journal of Physics*, Vol. 24, 373-396, 1971b.
- [51] Crane, R. K., "Ionospheric scintillation", *Proceedings of the IEEE*, Vol. 65(2), 181-199, 1977.
- [52] Nakagami, M., "The m-distribution - A general formula of intensity distribution of rapid fading", in *Statistical Methods in Radio Wave Propagation*, W.C. Hoffman Ed., Symposium Publications Division, Pergamon Press, 1960.
- [53] Rino, C. L., "A power law phase screen model for ionospheric scintillation: 1. Weak scatter", *Radio Science*, Vol. 14, 1135-1145, 1979a.
- [54] Rino, C. L., "A power law phase screen model for ionospheric scintillation: 2. Strong scatter", *Radio Science*, Vol. 14, 1147-1155, 1979b.
- [55] Rino, C. L., "On the application of phase screen models to the interpretation of ionospheric scintillation data", *Radio Science*, Vol. 17, 855-867, 1982.
- [56] Rino, C. L., Fremouw, E. J., "The angle dependence of singly scattered wavefields", *Journal of Atmospheric and Terrestrial Physics*, Vol. 39, 859-868, 1977.

- [57] Rino, C. L., Owens, J., "Numerical simulations of intensity scintillation using the power law phase screen model", *Radio Science*, Vol. 19, 891-908, 1984.
- [58] Rumsey, V. H., "Scintillations due to a concentrated layer with a power-law turbulence spectrum", *Radio Science*, Vol. 10, 107-114, 1975.
- [59] Shkarofsky, I. P., "Generalised turbulence space-correlation and wave-number spectrum-function pairs", *Canadian Journal of Physics*, Vol. 46, 2135-2153, 1968.
- [60] Tatarski, V. I., "Wave propagation in a turbulent medium", McGraw-Hill, New York, 1961.
- [61] Taylor, L. S., "Scintillation of randomised electric fields", *Journal of Mathematical Physics*, Vol. 13, 590, 1972.
- [62] Umeki, R., Liu, C. H., Yeh, K. C., "Multifrequency spectra of ionospheric amplitude scintillations", *Journal of Geophysical Research*, Vol. 82, 2752-2760, 1977.
- [63] Whitney, J. E., Aarons, J. A., Allen, R. S., Seeman, D. R., "Estimation of the cumulative amplitude probability distribution function of ionospheric scintillations", *Radio Science*, Vol. 7, 1095-1104, 1972.
- [64] Whitter, L. A., "Radio wave propagation in structured ionization for satellite and radar applications", 1992.
- [65] Yeh, K. C., Liu, C., "Radio wave scintillations in the ionosphere", *Proceedings of the IEEE*, Vol 70(4), 1982.

Appendix A

GPS Dual Frequency Ionospheric Correction

Dual frequency GPS receivers remove ionospheric group delay errors by forming the following linear combination of the L1 and L2 P(Y)-Code observables [46]:

$$P = \frac{P2 - \gamma P1}{1 - \gamma},$$

where:

P = pseudorange observable corrected for the ionosphere,

P1 = pseudorange measured at the GPS L1 frequency,

P2 = pseudorange measured at the GPS L2 frequency,

$$\gamma = \left(\frac{f_{L1}}{f_{L2}} \right)^2 \approx 1.647,$$

f_{L1} = GPS L1 frequency (1575.42 MHz),

f_{L2} = GPS L2 frequency (1227.6 MHz).

The variances of the thermal noise and multipath errors on the resulting ionospheric free observable are much larger than on either of the two individual P(Y)-Code observables. The relationship between these variances is:

$$\begin{aligned} \sigma_P^2 &= \left(\frac{1}{1 - \gamma} \right)^2 \sigma_{P2}^2 + \left(\frac{\gamma}{1 - \gamma} \right)^2 \sigma_{P1}^2 \\ &\approx 2.39 \sigma_{P2}^2 + 6.48 \sigma_{P1}^2 \end{aligned}$$

where σ_{P1}^2 and σ_{P2}^2 are the noise variances of the P1 and P2 observables respectively and σ_P^2 is the noise variance of the ionospheric free observable. Numerical values of these variances are given in Appendix D.

Appendix B

Ionospheric delay at GPS Frequencies

The ionosphere is a dispersive medium¹ in which the refractive index n is defined by the following expression² [8]:

$$n = \sqrt{1 - \frac{2X(1-X)}{2(1-X) - Y^2 \sin^2 \theta \pm \sqrt{(Y^4 \sin^4 \theta + 4Y^2 \cos^2 \theta (1-X)^2)}}},$$

where:

$$X = \left(\frac{f_p}{f} \right)^2,$$

$$Y = \left(\frac{f_H}{f} \right),$$

$$f_p = \sqrt{\frac{Ne^2}{4\pi^2 \epsilon_0 m_e}} \quad \text{is the Plasma frequency,}$$

$$f_H = \frac{\mu_0 e H}{2\pi m_e} \quad \text{is the Gyro frequency,}$$

N = the number density of free electrons in the ionosphere,

f = the carrier frequency,

e and m_e = the electron charge and mass respectively,

ϵ_0 and μ_0 = the free space permittivity and permeability,

H = the Earth's magnetic field intensity, and

θ = the angle between the Earth's magnetic field lines and the direction of propagation of the carrier.

The plasma frequency, f_p , is the frequency of simple harmonic motion of an electron in a plasma and is typically less than about 20MHz in the ionosphere. The gyro frequency, f_H , is defined as the spiralling frequency of electrons in a magnetic field and is usually less than 1.4MHz in the Earth's magnetic field. As the carrier frequency, f , is much larger than either f_p or f_H at L-band frequencies, the X and Y terms become very small, and the Appleton-Hartree formula can be approximated as follows:

$$n \approx \sqrt{1 - \left(\frac{f_p}{f} \right)^2}.$$

¹ In a dispersive medium, the refractive index is a function of frequency.

² The Appleton-Hartree formula for the ionospheric refractive index.

The phase and group velocities (V_p, V_g) of an electromagnetic wave propagating in a dispersive medium are given by:

$$V_p = \frac{\omega}{k} \quad \text{and} \quad V_g = \frac{d\omega}{dk},$$

where $\omega = 2\pi f$ is the angular carrier frequency, $k = 2\pi/\lambda = 2\pi f/c$ is the wave number and c is the speed of light in a vacuum. Expanding these expressions by incorporating the L-band approximation for n gives:

$$V_p = \frac{\omega}{k} = \frac{c}{n} \approx \frac{c}{\sqrt{1 - \left(\frac{f_p}{f}\right)^2}},$$

$$V_g = \frac{d\omega}{dk} \approx \frac{1}{\frac{d}{d\omega} \left(\frac{2\pi f}{c} \sqrt{1 - \left(\frac{f_p}{f}\right)^2} \right)} = n c = c \sqrt{1 - \left(\frac{f_p}{f}\right)^2}.$$

These expressions may be approximated by the first two terms of their Binomial series expansions to give:

$$V_p \approx c \left(1 + 0.5 \left(\frac{f_p}{f} \right)^2 \right),$$

$$V_g \approx c \left(1 - 0.5 \left(\frac{f_p}{f} \right)^2 \right).$$

The total error in this approximation is less than about 1% at L-band frequencies. This result shows that at L-band, the phase velocity is increased and the group velocity reduced by equal amounts, given by $0.5c(f_p/f)^2$.

The phase advance and group delay (d_p, d_g seconds) resulting from propagation through the ionosphere can be found by integrating the inverse of the velocities along the ray path:

$$d_p = \int \frac{1}{V_p} ds = \int \frac{n}{c} ds = \frac{1}{c} \int \sqrt{1 - \left(\frac{f_p}{f}\right)^2} ds,$$

$$d_g = \int \frac{1}{V_g} ds = \int \frac{1}{nc} ds = \frac{1}{c} \int \frac{1}{\sqrt{1 - \left(\frac{fp}{f}\right)^2}} ds$$

The square root terms may again be approximated by the first two terms of their respective Binomial series expansions to give:

$$d_p \approx \frac{1}{c} \int \left(1 - 0.5 \left(\frac{fp}{f} \right)^2 \right) ds = S/c - \frac{1}{2cf^2} \int fp^2 ds = R - d_{\text{IONO}},$$

$$d_g \approx \frac{1}{c} \int \left(1 + 0.5 \left(\frac{fp}{f} \right)^2 \right) ds = S/c + \frac{1}{2cf^2} \int fp^2 ds = R + d_{\text{IONO}},$$

where S is the distance to the satellite. These equations consist of a free space delay term R and an ionospheric delay term d_{IONO} . The ionospheric delay term may be expanded by inserting the expression for fp to give:

$$d_{\text{IONO}} = \frac{1}{2cf^2} \int fp^2 ds = \frac{1}{2cf^2} \int \frac{Ne^2}{4\pi^2 \epsilon_0 m_e} ds = \frac{e^2}{8\pi^2 \epsilon_0 m_e c f^2} \int N ds \quad (\text{seconds}),$$

where $\int N ds$ is the Total Electron Content (TEC) along the line of sight to the satellite. Multiplying by c to convert to distance, and substituting in the values of e , m_e and ϵ_0 gives the equivalent delay term in metres:

$$d_{\text{IONO}} = \frac{40.3 * \text{TEC}}{f^2} \quad (\text{metres})$$

This is the expression used in GPS pseudorange equations to define the range error resulting from the ionosphere and, although it is an approximation to the true delay, at L-band frequencies it is very accurate.

Appendix C

GPS Single Frequency Ionospheric Model

The GPS single frequency ionospheric model [1] provides single frequency users with a correction which reduces the RMS ionospheric delay error by approximately 50% [1], [12]. The model is broadcast to all users as a collection of eight parameters contained within the GPS navigation message. These parameters (α_i , β_i for $i=1$ to 4) are the coefficients of two third order polynomials in magnetic latitude which define the amplitude and period of a half co-sinusoid representing vertical ionospheric delay. This is then converted to slant delay by applying an appropriate obliquity factor which is a function of elevation. The model parameters are updated at least once every 6 days [1] by the GPS Master Control station from a set of 370 coefficients. The choice of coefficients depends on the day of year (ie seasonal dependence) and on solar activity. Consequently, the model is a function of the local time, latitude, solar activity and season. The set of 370 coefficients are derived from the Bent ionospheric model [11] which is based largely on data from the Northern hemisphere. The model is given by:

$$\begin{aligned}
 T_{\text{IONO}} &= O(e)[A + B \cos(x)] \\
 &\approx O(e) \left(A + B \left[1 - \frac{x^2}{2} + \frac{x^4}{24} \right] \right) \quad \text{for } |x| < \pi/2 \\
 &= O(e) \cdot A \quad \text{for } |x| \geq \pi/2
 \end{aligned}$$

where:

T_{IONO} is the slant ionospheric delay at the L1 frequency (s),

$$x = \frac{2\pi(t - 50400)}{P} \quad \text{radians,}$$

t = the Local Time (s),

$P = \beta_1 + \beta_2 \phi_m + \beta_3 \phi_m^2 + \beta_4 \phi_m^3$ is a polynomial representing the cosine period (s),

$B = \alpha_1 + \alpha_2 \phi_m + \alpha_3 \phi_m^2 + \alpha_4 \phi_m^3$ is a polynomial representing amplitude (s),

$O(e)$ = An obliquity factor (see later),

$A = 5 \cdot 10^{-9}$ is a constant night time level (s),

ϕ_m = geomagnetic latitude (semi-circles)

The geomagnetic latitude, ϕ_m , is the projection of the ionospheric intercept point³ onto the Earth's surface in geomagnetic coordinates (referenced to the Earth's magnetic pole). The transformation which relates geographic latitudes to geomagnetic latitudes is approximately given by:

³ Assumed to be at a height of 350km [1].

$$\phi_m \approx \phi_i + 0.064 \cos(\lambda_i - 1.617) \quad (\text{semi-circles}),$$

where ϕ_i and λ_i are the corresponding geographic latitude and longitude of the ionospheric intercept point. These are given by:

$$\phi_i = \phi_u + \psi \cos(\alpha)$$

$$\lambda_i = \lambda_u + \frac{\psi \sin(\alpha)}{\cos(\phi_i)}$$

where:

$$\psi = \frac{0.0137}{e + 0.11} - 0.022 \quad \text{is the Earth Centred angle (semi-circles),}$$

α = Satellite Azimuth angle (semi-circles),

e = Satellite Elevation angle (semi-circles),

ϕ_u = User's geographic latitude (semi-circles),

λ_u = User's geographic longitude (semi-circles)

The obliquity factor is given by $O(e) = 1 + 16(0.53 - e)^3$ and converts the vertical ionospheric delay at the ionospheric intercept point to an equivalent slant delay. An obvious source of error lies in any mismatch between the uniform ionospheric model on which the obliquity factor is based and the actual ionosphere. This will lead to errors which grow as the elevation angle of the satellite decreases.

Appendix D

TEC Estimation

The accurate estimation of TEC using GPS is important for the following reasons:

1. To improve the ability of both stand alone and long range differential GPS receivers to remove ionospheric delay errors.
2. To provide data to validate and update ionospheric scintillation models. Such models can be used as mission planning tools to provide predictions of the locations and intensity of scintillation activity in a region. Predictive scintillation models have the potential to benefit both SPS and PPS users.
3. To provide real-time updates for WADGPS ionospheric models.

Independent estimates of TEC can be obtained from both the code and carrier phase pseudorange observables. Code TEC estimates suffer from high levels of thermal and multipath noise but are absolute (assuming hardware biases have been eliminated). Carrier phase TEC estimates are very low noise but are subject to an unknown initial cycle ambiguity and can suffer from cycle slips⁴. In general, both estimates are required in order to obtain a single, low noise and absolute measures of TEC.

Expressions for the code and carrier phase pseudorange observables at the L1 and L2 frequencies are as follows:

$$\text{L1 P(Y)-Code: } P1 = R + c(dt - dT) + d_{\text{TROPO}} + d_{\text{IONO_L1}} + b_{S1} + b_{R1} + n_{\text{TP1}} + n_{\text{MP1}}$$

$$\text{L2 P(Y)-Code: } P2 = R + c(dt - dT) + d_{\text{TROPO}} + d_{\text{IONO_L2}} + b_{S2} + b_{R2} + n_{\text{TP2}} + n_{\text{MP2}},$$

$$\text{L1 Phase: } \phi1 = R + c(dt - dT) + d_{\text{TROPO}} - d_{\text{IONO_L1}} + b_{S1} + b_{R1} + n_{\text{T}\phi1} + n_{\text{M}\phi1} + N_1\lambda_1,$$

$$\text{L2 Phase: } \phi2 = R + c(dt - dT) + d_{\text{TROPO}} - d_{\text{IONO_L2}} + b_{S2} + b_{R2} + n_{\text{T}\phi2} + n_{\text{M}\phi2} + N_2\lambda_2$$

where R is the true range to the satellite, c is the speed of light, dt is the satellite clock error (including SA), dT is the receiver clock error, d_{TROPO} is the tropospheric delay, d_{IONO} is the ionospheric delay, b_S and b_R are the satellite and receiver interchannel biases (hardware biases), n_T and n_M are the thermal and multipath errors and $N\lambda$ is the cycle ambiguity in the carrier measurement. The ionospheric delay, d_{IONO} , is proportional to TEC according to the following expression (Appendix B):

$$d_{\text{IONO}} = \frac{40.3 \cdot \text{TEC}}{f^2}$$

By differencing and scaling the code and carrier phase pseudorange observables, two independent estimates of TEC can be obtained as follows:

⁴ Steps of an integer number of cycles in the carrier phase caused by noise in the carrier tracking loops.

$$\text{Code: TEC} = \frac{(P2 - P1 - \Delta b_S - \Delta b_R + n_{T\Delta P} + n_{M\Delta P})}{40.3 * \left[\frac{1}{f_2^2} - \frac{1}{f_1^2} \right]}$$

$$\text{Carrier: TEC} = \frac{(\phi1 - \phi2 + \Delta b_S + \Delta b_R + n_{T\Delta\phi} + n_{M\Delta\phi} + \Delta N\lambda)}{40.3 * \left[\frac{1}{f_2^2} - \frac{1}{f_1^2} \right]}$$

where $\Delta b_R = b_{R2} - b_{R1}$ and $\Delta b_S = b_{S2} - b_{S1}$ are the interchannel biases, $n_{T\Delta}$ and $n_{M\Delta}$ are the differenced thermal and multipath noises respectively and $\Delta N\lambda = N_1\lambda_1 - N_2\lambda_2$ is the differenced carrier cycle ambiguity. By forming these linear combinations, the frequency independent terms including the true range R , the clock errors $c(dt-dT)$ and the tropospheric delay are eliminated. However, the interchannel biases, cycle ambiguities, thermal and multipath noises persist.

As the levels of thermal and multipath noise on the carrier are very much less than on the code (Appendix E), the code TEC is generally used only to obtain an estimate of the carrier cycle ambiguity, and then abandoned. The ambiguity estimate is obtained by fitting the carrier TEC to the code TEC over a segment of data for which carrier cycle slips have not occurred (ie the cycle ambiguity is constant over the segment). If a cycle slip occurs, a new ambiguity estimate must be obtained from data following the slip. In practice, the ambiguity estimate is obtained by simply averaging the double differenced carrier phase and the code phase observables as follows:

$$\Delta \hat{N}\lambda = \langle (\phi1 - \phi2) - (P2 - P1) \rangle$$

The resulting ambiguity estimates are contaminated by both interchannel biases and residual multipath errors. Interchannel biases are caused by differences in propagation delay of RF signals through the satellite and receiver RF channels. It is possible to significantly reduce these biases by calibrating a receiver and by applying current estimates of the satellite biases. Alternatively, interchannel bias estimation techniques such as those suggested by Wilson [21] and Lanyi & Roth [23] can be applied if a network of receivers is available. Residual multipath biases are caused by long period multipath errors. Periods as long as 1 hour can occur depending on the position of the multipath reflector and the elevation angle and trajectory of the satellite. As indicated in Appendix E, multipath errors are generally not predictable in an absolute sense unless the multipath environment remains constant for at least one day. Under these circumstances, multipath template techniques can be applied [24]. When such techniques cannot be applied, data segments should be selected which are long enough to average the effects of long period multipath errors.

The resulting carrier phase based TEC estimate is found by adding the ambiguity estimate to the carrier phase difference as follows:

$$\hat{T}EC = \frac{(\phi_1 - \phi_2 + \Delta\hat{N}\lambda)}{40.3 * \left[\frac{1}{f_2^2} - \frac{1}{f_1^2} \right]}$$

An example of TEC data obtained from a GPS receiver at Cocos Islands is given in Figure 9. Notice that the thermal noise on the code is far greater than on the carrier and is highly dependant on the satellite elevation angle (given in the lower panel). The ambiguity resolution technique applied to the data in Figure 9 is based on Maximum Likelihood estimation [13]. This technique weights the data in an optimum fashion according to the variance of the code measurements.

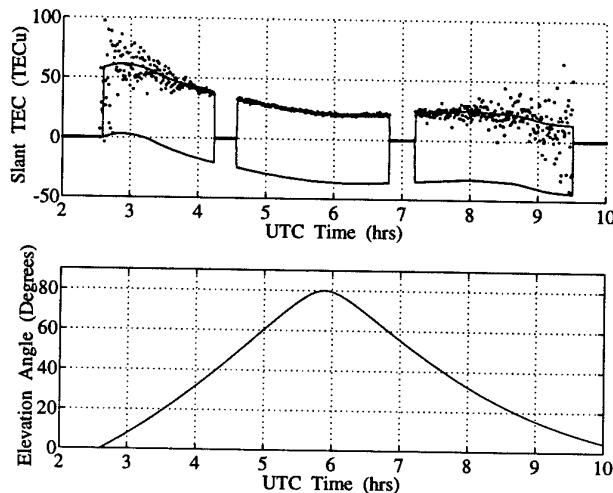


Figure D.1: Example of code based TEC (dots) and carrier phase based TEC (lower solid line) from Cocos Islands (day 100 of 1995). Unambiguous carrier phase TEC (upper solid line) is found by adding the cycle ambiguity to the carrier phase TEC estimate.

Two receiver types other than PPS P(Y)-Code receivers have been developed to directly measure TEC without access to the Y-Code. These are cross-correlation receiver (eg the Turbo Rogue ICS-4000Z) and the Ashtech P-W tracking receiver [3]. Cross-correlation receivers estimate the difference in pseudorange between the L1 and L2 P(Y)-Codes by correlating one channel with the other. The technique relies on the fact that the encrypted P(Y)-Codes on the two carriers are the same, apart from a delay imposed by the ionosphere. P-W tracking receivers correlate the L1 and L2 channels with a locally generated P-Code resulting in an L1 and L2 W-Code signal (ie the P-Code is stripped from the underlying P(Y)-Code). The W-Code signals are then low

pass filtered⁵ and cross-correlated to determine the differential delay. The advantages of the P-W tracking technique over direct cross-correlation are an improvement in the signal to noise ratio (SNR) and access to the individual L1 and L2 P-Code pseudoranges.

Both the cross-correlation and P-W tracking receivers are SPS receivers. Consequently, they can be operated by civilian users and installed in unsecured, remote locations such as S.E. Asia (the region of the equatorial anomaly). The principal disadvantage of these receiver types is that the code TEC estimates are considerably noisier than those obtained by direct P(Y)-Code correlation. This additional noise is mainly thermal noise resulting from a lower SNR in the tracking loops. The reduced SNR can also lead to an increase in the probability of cycle slips within the carrier tracking loops. Both of these effects make the problem of resolving the carrier cycle ambiguity more difficult. An additional complication in equatorial regions is the possibility of amplitude and phase fluctuations caused by scintillations. Amplitude scintillations can lead to further reductions in the SNR of the tracking loops while phase scintillations can add phase noise directly to the carrier tracking loops. Both effects increase code noise and the probability of cycle slips.

⁵ The W-Code bandwidth is 20 times smaller than the P-Code bandwidth.

Appendix E

Error Sources in GPS TEC Estimates

GPS based estimates of TEC are subject to a number of errors, including thermal noise, multipath errors and both satellite and receiver channel biases. Each of these is discussed briefly below:

E.1 Thermal Noise

The expression for the 1σ or RMS code tracking loop jitter for a Delay Locked Loop (DLL) discriminator is given by [5]:

$$\sigma_{\text{DLL}} = \Delta \sqrt{\frac{F \cdot d \cdot B_n}{C/N_0} \left[1 + \frac{2}{C/N_0 \cdot T(2-d)} \right]} \quad \text{m},$$

where:

- Δ = PRN code chip width (29.3m: P(Y)-Code, 293m: C/A-Code),
- d = Separation between the early and late gates (usually 1 chip),
- F = DLL discriminator correlation factor:
 - 0.5 for dedicated early/late correlators,
 - 1.0 for time shared early/late correlators,
- B_n = Code tracking loop bandwidth (Hz),
- C/N_0 = Carrier to noise power density ratio (Hz),
- T = Integration time of the pre-detection filters (\leq Navigation data bit length = 20ms).

The corresponding expression for a Costas type Phase Locked Loop (PLL) discriminator (a typical carrier tracking loop) is given by [5]:

$$\sigma_{\text{PLL}} = \frac{\lambda}{2\pi} \sqrt{\frac{B_n}{C/N_0} \left[1 + \frac{1}{2T \cdot C/N_0} \right]} \quad \text{m},$$

where:

- λ = Carrier wavelength (0.190m: L1, 0.244m: L2),
- B_n = Carrier tracking loop bandwidth (Hz)

Typical values of the code and carrier tracking loop bandwidth's under stationary, unaided conditions are 1Hz and 10Hz respectively. By employing techniques such as INS aiding, tracking loop bandwidth's can be significantly reduced with a consequent reduction in the levels of thermal noise.

The carrier to noise power density ratio of the GPS signal is given by:

$$C/N_0 = P_S + G - L_i - 10\log_{10}(kT_S),$$

where:

- P_S = Satellite Signal Power (W)
= -160 dBW (C/A-Code), -163 dBW (L1 P-Code), -166 dBW (L2 P-Code),
- kT_S = Thermal noise power density (W/Hz),
- k = Boltzman's constant (1.38×10^{-23} J/K),
- T_S = System Noise temperature = FT_0 (K),
- T_0 = Room temperature (290 K),
- F = Receiver noise Figure (equivalent to 2.5dB),
- G = Receiver antenna gain (dBi),
- L_i = Receiver implementation loss (typically 2dB)

Assuming $G=0$ dBi, $F=2.5$ dB and $L_i=2$ dB, the carrier to noise density ratios of the three GPS ranging codes are 39.5dB, 36.5dB and 33.5dB for the C/A-Code, L1 P(Y)-Code and L2 P(Y)-Code respectively. For a dedicated early-late code correlator with a 1 chip spacing and a pre-detection integration time of 20ms, the corresponding RMS thermal noise levels are as given in Table E.1.

Table E.1: RMS thermal noise levels of the GPS pseudorange observables.

C/A-Code	σ_{CA}	7.3 ns	2.2 m
L1 P-Code	σ_{P1}	1.0 ns	0.31 m
L2 P-Code	σ_{P2}	1.5 ns	0.45 m
L1 Carrier (from C/A-Code)	$\sigma_{\Phi 1}$	3.3 ps	1.0 mm
L2 Carrier (from L2 P-Code)	$\sigma_{\Phi 2}$	8.7 ps	2.6 mm

E.2 Multipath Noise

Multipath errors are the result of reflections of the GPS signals from surfaces near to the antenna. Many factors influence multipath including the proximity, number and orientation of reflective surfaces, reflection coefficients, satellite elevation angles, the antenna design and the frequency or bit rate of the signal. It is therefore extremely difficult to eliminate multipath by predicting its value in advance. However, it can be reduced by careful selection of the antenna site (eg away from significant reflectors), by the selection of antennas with low gain at low elevation angles and by the use of RF absorptive material.

Multipath errors affect both the amplitude and phase of the GPS code and carrier resulting in pseudorange and range rate errors. The carrier phase error is two orders of magnitude less than the code error because of the much shorter period of the carrier

(0.63 ns compared to 98ns for the P-Code). Carrier and code errors resulting from a single reflected signal can be found from the following set of equations [20]

E.2.1 Carrier Multipath

The maximum error on a carrier subject to multipath is given by the following expression:

$$\alpha_{\max} = \sin^{-1}\left(\frac{V_R}{V_D}\right),$$

where:

V_R = Reflected signal voltage,

V_D = Direct signal voltage.

This attains a maximum value of 90° ($\lambda/4$) when the direct signal voltage is equal to the reflected signal voltage. Under these conditions the multipath error is:

$$\alpha_{1\max} = \pm 0.048\text{m} \quad (\text{GPS L1})$$

$$\alpha_{2\max} = \pm 0.061\text{m} \quad (\text{GPS L2})$$

The maximum differential phase delay (from which carrier phase TEC is calculated) occurs when one phase error term is at its maximum positive value, and the other is at its maximum negative value. This is given by $|\alpha_{1\max}| + |\alpha_{2\max}| = 0.109\text{m}$. The equivalent maximum TEC error is found by dividing by $40.3 \left(\frac{1}{f_{L1}^2} - \frac{1}{f_{L2}^2} \right)$ to give an error of approximately 0.67 TECu.

E.2.2 Code (group) Multipath

The error in group delay in an early-late gate PRN code tracking loop is given by the root of the early-late gate error function as follows [20]:

$$D(\lambda) = [R(\lambda + \lambda_d) - R(\lambda - \lambda_d)] \cos(-\theta_m^*) + \Psi [R(\lambda + \lambda_d - \delta_m) - R(\lambda - \lambda_d - \delta_m)] \cos(\theta_m - \theta_m^*)$$

where:

$$\theta_m^* = \tan^{-1} \left(\frac{\Psi * R(\lambda - \delta_m) * \sin(\theta_m)}{R(\lambda) + \Psi * R(\lambda - \delta_m) * \cos(\theta_m)} \right),$$

$R(\lambda)$ = PRN code cross correlation function

$$= 1 - \left(\frac{|\lambda|}{T} \right) \quad \text{for } |\lambda| \leq T$$

$$= 0 \quad \text{for } |\lambda| > T$$

T = PRN code chip width,

λ = group delay error due to multipath,

λ_d = early/late gate delay (= $T/2$),

Ψ = ratio of reflected to direct signal voltage,

θ_m = multipath signal carrier phase relative to direct ray,

δ_m = time difference between direct and reflected ray.

The maximum group delay error due to multipath will occur when $\Psi=1$. This correspond to an error of $T/2$ seconds, which when translated into a range error gives:

$$\lambda_{1\max} = \pm 14.7\text{m} \quad (\text{P - Code})$$

$$\lambda_{2\max} = \pm 147\text{m} \quad (\text{C / A - Code})$$

The maximum differential P-Code delay (from which code TEC is calculated) occurs when one code error term is at its maximum positive value, and the other is at its maximum negative value. This is given by $2*|\lambda_{1\max}| = 29.4\text{m}$. The equivalent

maximum TEC error is found by dividing by $40.3 * \left(\frac{1}{f_{L1}^2} - \frac{1}{f_{L2}^2} \right)$ to give an error of approximately 180 TECu.

This analysis serves to demonstrate that the magnitude of multipath errors on the code is far greater than on the carrier. Indeed, the maximum code TEC error can exceed actual TEC measurements. These results are however extremely pessimistic as they are calculated for $\Psi=1$ and a worst case value of δ_m (ie assuming mirror like reflections from adjacent structures etc.). They also fail to take into account the gain pattern of the antenna and the change in polarisation from right hand circular at grazing angles to left hand elliptical above the Brewster angle. For the case of $\Psi=0.1$, the code errors are reduced by a factor of 10, while the carrier phase errors are reduced by a factor of about 16.

E.3 Interchannel Biases

Measurements of GPS pseudorange are corrupted by small instrumental biases introduced by the RF components of a satellite and receiver. As these biases are a function of the carrier frequency, they are not removed by simply differencing the L1 and L2 pseudorange measurements. Consequently, TEC, which is found by scaling the pseudorange difference appropriately, is corrupted by differential instrumental biases

between the L1 and L2 channels (referred to as the interchannel bias). Fortunately, interchannel biases are relatively stable with time and can be measured for a particular satellite and receiver, and thus removed.

The measurement of interchannel biases is, however, complicated by the presence of the ionosphere. The differential delay between the L1 and L2 P(Y)-Codes ($P1(t) - P2(t)$) can be represented as follows:

$$P1(t) - P2(t) = k * TEC + b_S + b_R + n_T(t) + n_M(t)$$

where k is a constant, TEC is the Total Electron Content, b_S is the satellite interchannel bias, b_R is the receiver interchannel bias, $n_T(t)$ and $n_M(t)$ represent thermal and multipath noise respectively. A number of researchers have estimated b_S and b_R by modelling TEC over a region and making use of data from a number of receiver sites [21], [22], [23]. This approach requires that at least some of the receivers be calibrated by alternative means in order to reduce the number of degrees of freedom. Calibration to remove receiver interchannel biases is only possible with receivers specifically designed for this purpose such as the Allen Osborne Turbo Rogue and the Ashtech VII. Such receivers incorporate a calibrated signal source which is used to feed L1 and L2 signals directly into the receiver's RF front end.

Failure to account for interchannel biases can lead to large errors in GPS based estimates of TEC. Such errors can often exceed the true line of sight TEC value, particularly at night when it is possible for negative values to be calculated. Typical maximum errors are ± 9 TECu for satellite interchannel biases and ± 30 TECu for receiver biases [21].

Appendix F

Fresnel-Kirchoff Diffraction Model

The scintillation model used in this study is essentially that of Titheridge [36] and Davies [37] and is based on the solution of the Fresnel-Kirchoff integrals for an assembly of field aligned irregularities. The irregularities are assumed to produce Gaussian variations in TEC in directions normal to the earth's magnetic field lines, but no variations along the field lines. For convenience, the phase perturbations are assumed to be concentrated within a thin phase screen situated at a typical F2 layer peak height. In reality, such perturbations would result from the cumulative effect of numerous small irregularities located along the ray path.

The perturbation in phase of an emergent wave resulting from a single Gaussian irregularity is given by:

$$\Phi(x, f) = \Phi_0 \cdot \exp\left[-(x - x_0)^2 / d^2\right],$$

where x is the horizontal distance from the centre of the irregularity, d is the scale size and f is the GPS carrier frequency. The peak phase variation, Φ_0 , is related to the peak TEC variation, ΔTEC , through the expression:

$$\Phi_0 = k \cdot \Delta\text{TEC}_0 / f \quad (\text{radians}),$$

where k is a constant.

The peak phase variations can either be positive, which corresponds to an enhancement in TEC (a defocusing type irregularity), or negative which corresponds to a depletion in TEC (a focusing type irregularity). Both types of irregularity have been shown to exist in the ionosphere [47]. The radio wave is also assumed to experience no attenuation as it passes through the phase screen. Consequently, any amplitude fluctuations are caused entirely by the effects of mutual interference across the wavefront as it propagate towards the ground.

At the ground and relative to the undisturbed wave, the in-phase and quadrature components of a vertically propagating plane wave¹ are given by:

$$I = 1 - 2 \int_{ir} \sin(P_0 + \Phi/2) \sin(\Phi/2) dx / \sqrt{r\lambda}$$

$$Q = 2 \int_{ir} \cos(P_0 + \Phi/2) \sin(\Phi/2) dx / \sqrt{r\lambda}$$

¹ In this analysis it is assumed that the GPS satellites are at sufficiently high altitudes to make the simplifying assumption that the all incident waves are plane.

where $P_0 = -\pi/4 - 2\pi(r-h)/\lambda$, h is the screen height and r joins the elements dx on the phase screen to a point on the ground (see Figure F.1 below).

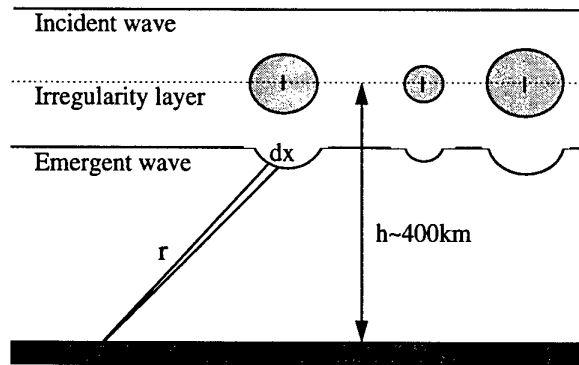


Figure F.1: Geometry of the thin screen diffraction model

The integrals are calculated over the region of the irregularities in the plane of the phase screen. The resulting phase and amplitude variations are obtained from the I and Q components as follows:

$$\text{Phase} = \tan^{-1}(Q/I)$$

$$\text{Amplitude} = \sqrt{Q^2 + I^2}$$

For irregularities much larger than the first Fresnel zone radius, z_F , diffraction effects are minimal and a geometric optics solution can be employed. As a result, phase variations on the ground will closely resemble those in the ionosphere and amplitude variations will be negligible. On the other hand, for scale sizes of the order of the Fresnel zone radius or smaller, or for very large plasma density gradients, rapid variations in both amplitude and phase will occur. Irregularities smaller than z_F produce diffraction effects (also called ringing), whereas those containing large density gradients produce significant refraction and hence interference effects. Both cause rapid variations in the phase and amplitude of the GPS signals on the ground. For a Gaussian shaped irregularity, the threshold conditions for diffraction and interference are [36]:

$$\text{Diffraction: } d < z_F = \sqrt{\frac{\lambda z_1 z_2}{z_1 + z_2}} \approx \sqrt{\lambda z_2}$$

$$\text{Interference: } d < \sqrt{\frac{\Phi_0 h}{37f}}$$

where Φ_0 is the peak phase variation, z_1 and z_2 are the distances between the ionospheric irregularity layer and the satellite and receiver respectively. For $h=400\text{km}$,

a peak TEC variation of 1 TECu (approximately 1% of a typical equatorial TEC value during solar maximum), typical upper limits on the scale sizes of irregularities likely to cause these effects are:

Diffraction: 300m (L2), 275m (L1)

Interference: 220m (L2), 190m (L1)

This analysis also assumes vertical propagation and an irregularity which is overhead. For E region irregularities ($h \sim 100$ km), the equivalent dimensions are approximately half.

It is expected that irregularities of the order of the Fresnel Zone radius or slightly smaller will produce the most significant scintillation effects for GPS. Larger irregularities are unlikely to produce fully developed diffraction effects and would require very large peak densities in order to produce interference effects. Irregularities smaller than the Fresnel zone radius will produce very low intensity diffraction effects and so will also have negligible impact on the GPS signal.

The phase and amplitude fluctuations derived from this model are a function of position in an East-West direction. It is assumed that because the irregularities are field aligned, fluctuations do not exist in a North-South direction. Consequently, the temporal variations in phase and amplitude experienced by GPS will depend on the East-West components of the velocities of the irregularities, the GPS platform and the satellites. Typical irregularity velocities in an Easterly direction are of the order of 100 to 200 m/s [33].

Appendix G

Synthetic Scintillation Time Series Model

An overview of the Synthetic Scintillation Time Series model (SSTS) that has been developed, together with preliminary results, will now be given. A detailed description of this model will be given in a later report.

The objective of the SSTS model is to generate time series of ionospheric scintillation data, *i.e.* time series of amplitude and phase perturbations experienced by radio signals traversing the ionosphere under disturbed conditions. These data may then be applied to GPS system models to test the operation of various GPS receiver architectures under adverse ionospheric conditions. The basic approach used in the SSTS model to generate the required data is to characterise the signal statistically (*i.e.* appropriate probability density functions (PDF), power spectra, etc.) and then produce realisations of the data which conform to that statistical description. WBMOD, the model of global scintillation activity described earlier, is used to generate various parameters describing the scintillation and ionospheric irregularities required by SSTS for given conditions. In this manner a complete environmental model of scintillation specified.

There are several important considerations in developing a model of scintillation time series and these are: (1) The amplitude and phase data must have appropriate PDFs, (2) Amplitude and phase data must be appropriately correlated *e.g.* large phase variations are observed when deep amplitude fading occurs, (3) The data must have appropriate power spectra, (4) Require a propagation theory of the radio waves through turbulent media, and (5) As previously mentioned, relate the model to the environment though the supply of various required parameters from WBMOD. Each of these points will be considered in turn.

The probability density functions describing the scintillation perturbations of radio signals traversing the disturbed ionosphere are Nakagami-m (amplitude) and Gaussian (phase) [39], [63] & [51]. Respectively, these are given by:

$$P_N(r) = \frac{2m^m \cdot r^{2m-1}}{\Gamma(m) \cdot \langle r^2 \rangle^m} e^{-m \cdot r^2 / \langle r^2 \rangle} ,$$

$$P_G(\phi) = \frac{1}{\sqrt{2\pi\sigma_\phi^2}} e^{-\phi^2 / 2\sigma_\phi^2} ,$$

where Γ is the gamma function, r and ϕ are the amplitude and phase of the signal, and σ_ϕ is the standard deviation of the phase fluctuations or the phase scintillation index. The m -parameter in the Nakagami-m distribution is related to the S_4 index by $m = 1/S_4^2$. For large values of m (small S_4) the Nakagami-m distribution approaches

the Gaussian distribution. As S_4 increases, the Nakagami-m distribution tends toward the Rayleigh distribution and becomes Rayleigh at a value for S_4 of 1.0.

In order to fully describe the statistics of scintillating signals, a joint PDF of amplitude and phase is required. The reason for this is that one would expect the amplitude and phase fluctuations to be correlated to some degree. The reason for this is that as the amplitude fades, the phase becomes more variable; indeed if the amplitude falls to zero the phase becomes meaningless and may take on any value. Thus, when large amplitude fading is observed so too are large phase variations. It is important for this behaviour to be included in the generation of synthetic scintillation time series because it is much harder for a receiver to maintain lock on a signal when the amplitude exhibits deep fading simultaneously with large rates of change in the phase.

Various schemes have been tried describe the joint statistics of scintillating signals which are based on using Gaussian and log-normal distributions for the amplitude [39]. However, these are quite complicated as well as not describing the amplitude PDF as well as the Nakagami-m distribution which was designed specifically to describe intensity fading [52]. Due to the complexity of the joint statistics, a joint PDF incorporating the Nakagami-m distribution for the amplitude has not been developed. The method that has been developed to include the joint statistics will not be described here except to say that analytical techniques are not used, instead it is based on Monte-Carlo methods. The technique will be described in a subsequent report. The user is required to specify an appropriate level of correlation, r , between the amplitude and phase. It is anticipated that data from the network of scintillation receivers to be installed in the South East Asian region will be used to determine the degree of correlation.

The power spectra of the scintillating signals is determined through an analysis of the propagation of the radio wave through the disturbed ionosphere. The parabolic equation method (PEM) [65] is used to describe the propagation of the radio waves both through the turbulent media and free-space to the receiver, while the effect of the turbulent media on the radio waves is determined from phase screen diffraction theory [48], [49], [50], [53], [54], [55], [57] & [65]. For a single thin phase screen the following expressions for the spatial power spectrum of the log-amplitude, χ , and phase departure, ϕ , of the radio waves at the receiver may be derived [65]:

$$\begin{aligned}\Phi_{\chi}(\vec{\kappa}_{\perp}) &= 2\pi L_s \lambda^2 r_e^2 \sin^2(\kappa_{\perp}^2 z/2k) \Phi_{\Delta N}(\vec{\kappa}_{\perp}, 0), \\ \Phi_{\phi}(\vec{\kappa}_{\perp}) &= 2\pi L_s \lambda^2 r_e^2 \cos^2(\kappa_{\perp}^2 z/2k) \Phi_{\Delta N}(\vec{\kappa}_{\perp}, 0),\end{aligned}$$

where L_s is the 'slant' thickness of the phase screen (*i.e.* the irregularity layer), z is the distance from the phase screen to the receiver, r_e is the classical radius of the electron, λ and κ are the wavelength and wave number of the radio waves, and $\Phi_{\Delta N}$ is the 3-dimensional spatial spectrum of the ionospheric irregularities.

In order to proceed it is necessary to relate L_s to the thickness of the irregularity layer, L , and z to the height of the phase screen, h . The curvature of the Earth's surface must be considered for this analysis. Figure F.1 displays the geometry of the situation.

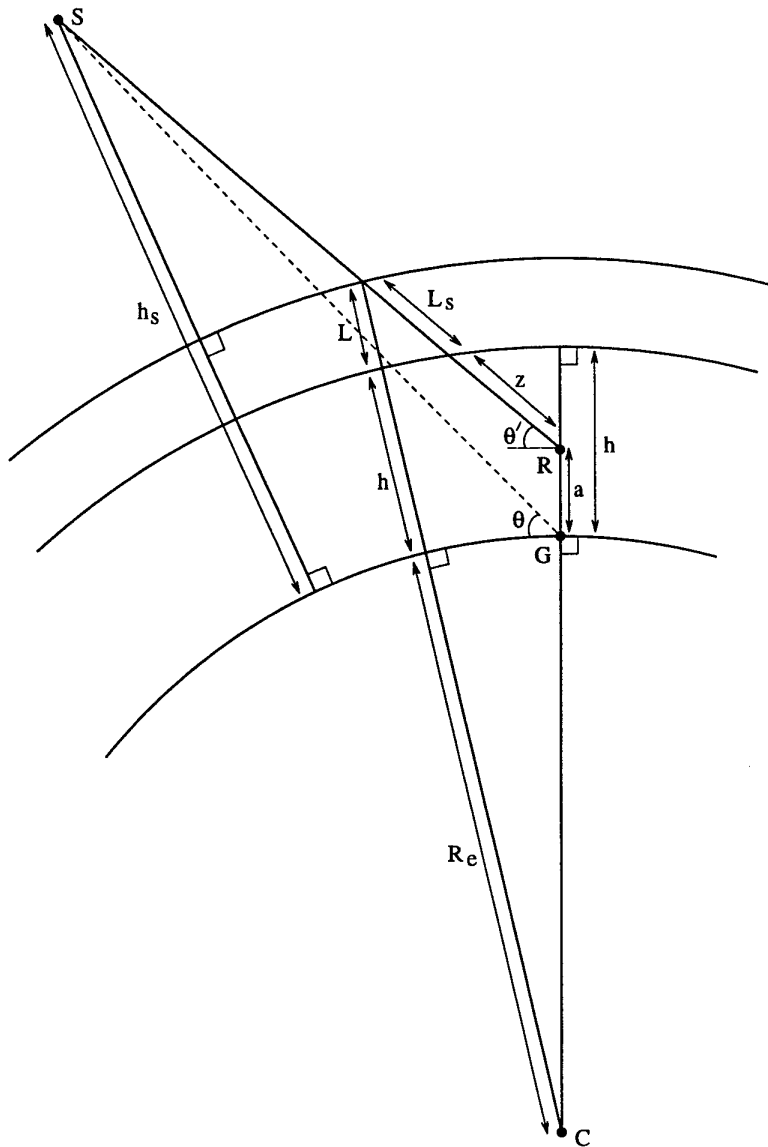


Figure G.1: Geometry of the signal propagation path where 'S' is the satellite, 'C' is the centre of the Earth, 'R' the receiver, and 'G' the point on the ground directly below the receiver.

From this figure it is possible to show that

$$z = \sqrt{[(h + R_e)^2 - (a + R_e)^2 \cos^2 \theta']} - (a + R_e) \sin \theta', \text{ and}$$

$$L_s = \sqrt{[(L + h + R_e)^2 - (a + R_e)^2 \cos^2 \theta']} - \sqrt{[(h + R_e)^2 - (a + R_e)^2 \cos^2 \theta']},$$

where R_e is the radius of the Earth, a is the altitude of the receiver, and θ' is the elevation of the satellite as seen from the receiver. From simple trigonometry it may be shown that θ' is related to the elevation of the satellite θ , by:

$$\tan \theta' = \tan \theta - \frac{a \sec \theta}{\sqrt{[(h_s + R_e)^2 - R \cos^2 \theta]} - R \sin \theta},$$

where h_s is the height of the satellite.

An appropriate expression for $\Phi_{\Delta N}$ is now required. The basic requirements for the 3D-spatial spectrum is that it must have a breaking (or outer) scale, below which (the inertial range) the spectrum drops off as a power law. From Tatarski [60] we have the following:

$$\Phi_N(\vec{\kappa}) = \frac{\sigma_N^2 l_0^3 \Gamma(p/2)}{\pi^{3/2} \Gamma((p-3)/2) (1 + l_0^2 \kappa^2)^{p/2}},$$

where σ_N is the RMS fluctuations of electron number density $\Delta N(\mathbf{r})$ about the background N_0 , l_0 is the structure outer scale, and p is the spectral index below the outer scale. An appropriate value for σ_N may be obtained from the following equation (Rino, 1979a, 1979b; Rino and Owen, 1984):

$$\sigma_N^2 = \frac{C_S l_0^{(2-p)} \Gamma(p/2 - 1)}{8\pi^{3/2} \Gamma((p+1)/2)},$$

where C_S is the irregularity strength defined at a wave number of 1 radian/m and is a function of altitude. From WBMOD one may obtain a value of the irregularity strength defined at a scale of 1km, C_k , at the altitude of interest (*i.e.* the height of the phase screen) and convert this appropriately to a value of C_S . Alternatively, σ_N may be ignored in the calculation of $\Phi_N(\vec{\kappa})$ and instead appropriately scale the final frequency power spectra such that the spectral strength at a frequency of 1 Hz, T , is that supplied by WBMOD.

The above expression for $\Phi_N(\vec{\kappa})$ does not include an inner (or freezing) scale below which, in the sub-inertial range, the power spectrum falls off more rapidly. Witter [64], introduced a freezing scale by modifying Tatarski's result as follows:

$$\Phi_N(\vec{\kappa}) = \frac{\sigma_N^2 l_0^3 \Gamma(p/2)}{\pi^{3/2} \Gamma((p-3)/2) (1 + l_0^2 \kappa^2)^{p/2} (1 + l_0'^2 \kappa^2)^{(p-p')/2}},$$

where l_0' is the freezing scale ($l_0' < l_0$), and p' is the power law drop-off in the sub-inertial range ($|p' > p|$).

An alternative power-law irregularity spectrum with a freezing scale and a sub-inertial range is that introduced by Shkarofsky (1968) (see also Yeh and Liu, 1982):

$$\Phi_N(\vec{\kappa}) = \frac{\sigma_N^2 (\kappa_0 l_0')^{(p-3)/2} l_0'^3 K_{p/2} \left(l_0' \sqrt{\kappa^2 + \kappa_0^2} \right)}{(2\pi)^{3/2} K_{(p-3)/2} (\kappa_0 l_0') \left(l_0' \sqrt{\kappa^2 + \kappa_0^2} \right)^{p/2}},$$

where $\kappa_0 = l_0/2\pi$ and $\kappa_0 l_0' \ll 1$, and $K_n(x)$ is the n^{th} -order modified Bessel function of the second kind of argument x . Note that in this expression the sub-inertial range is not a power law falloff with spectral index p' , but an exponential drop-off. Thus only one spectral index, being that for the inertial range, is required together with the inner and outer scale sizes to describe the power spectrum.

The current version of WBMOD (13.04) only supplies the power law index in the inertial range and the outer scale. Thus, for current version of the SSTS model, Equation 7 is used in the subsequent modelling of the spatial spectrum of the irregularities. However, one should keep in mind Equations 9 and 10; the introduction of these will be considered at a later date.

The frequency spectrum of the signal at the receiver is obtained from the signal spatial spectrum through the following equation [62] & [65]:

$$\Phi_{\chi,\phi}(f) = \frac{1}{v_t} \int_{-\infty}^{\infty} \Phi_{\chi,\phi}(\kappa_x = 2\pi f/v_t, \kappa_y) d\kappa_y,$$

where v_t is the relative velocity of the irregularities transverse to the radio propagation path. The coordinate frame has been chosen such that v_t is in the x direction in the x - z plane (the propagation path being in the z direction). The value of v_t is found from the velocity of the irregularities relative to the radio propagation path which is given by $\mathbf{v} = \mathbf{v}_d + \mathbf{v}_p$ where \mathbf{v}_d is the drift velocity of the irregularities and \mathbf{v}_p is the velocity of the ionospheric pierce point of the radio path due to the

motion of the satellite and the velocity of the receiver. For the GPS case the component of \mathbf{v}_p due to the satellite motion is negligible and only the receiver velocity is required to be considered.

It should be noted that in the analysis so far, that only the case of isotropic irregularities has been considered. Generalisation to the anisotropic case follows by replacing κ^2 with $\alpha_u^2 \kappa_u^2 + \alpha_v^2 \kappa_v^2 + \alpha_w^2 \kappa_w^2$, where $\alpha_u, \alpha_v, \alpha_w$, are dimensionless scaling factors along each axis. The anisotropy of the irregularities in electron density are governed by the geomagnetic field thus a series of rotations is required to transform the (u,v,w) frame of the irregularities to the (x,y,z) frame used in the calculation of the frequency power spectra. A detailed discussion on this is given by Rino and Fremow [56].

As mentioned previously, a single thin phase screen and an assumption of single scattering of the radio waves, was used to calculate the power spectrum of the signal propagating through the turbulent medium. This is fine for weak scattering, but we are interested in the strong scattering case, as it is under these conditions the receiver will be stressed. Expressions for the amplitude power spectrum have been derived for the strong scattering case and these employ thick multiply scattering phase screens [Gochelashvily and Shishov, 1971], [61] & [58]. The multiple scattering phase screen models describe the statistics of strongly scintillating signals much better than the single scattering approach, thus the multiple scattering approach is the better theory to use. However the power spectra in the two regimes do not vary to a great degree; the effect of strong scintillation activity is to cause some de-correlation of the signal time series which leads to an enhanced contribution of the high frequency components of the power spectrum. The intensity probability density function, on the other hand, does not vary considerably from the low to high scattering regimes but this has already been incorporated into the SSTS model separately; the phase screen analysis is only used to generate the correct power spectra. Thus, considering that the only effect of using a single thin phase screen is the underestimation of the contribution of the high frequency component of the scintillation time series, the use of this theory is justified as a first approach, especially considering it is computationally less intensive. The next stage of this work, however, will be to include a multiple scattering approach for the calculation of the power spectra.

This completes the specifications of the SSTS model. As previously mentioned, WBMOD is used to supply the quantities of the various parameters required by SSTS. These are: S_4 , σ_ϕ , r , L , h , p , l_0 , C_k , and \mathbf{v}_d . The altitude, dynamics and operating frequency of the receiver, which are also required, are supplied by the user for a given trial. In addition, WBMOD requires various input parameters to be supplied; these are the receiver and satellite locations (latitude, longitude and altitude), the date and local solar time at the receiver, the frequency of the carrier wave (in this case the GPS frequencies), the duration over which the receiver requires phase stability, the percentile at which the scintillation levels are to be generated, and the geomagnetic activity index (K_p) and smoothed Zurich sunspot number (R_{12}). All of these parameters

except for the last two are determined by the trial scenario. The K_p index and R_{12} may be input as real or predicted values, both of which are supplied by the Ionospheric Predictions Service (IPS).

DISTRIBUTION LIST

Ionospheric Effects on Global Positioning System (U)

Mark F. Knight
Anthony Finn
Manuel Cervera

AUSTRALIA

DEFENCE ORGANISATION

Task Sponsors

Director General Land Development
SO2 (Land)
Director General Aerospace Development
SYS1

S&T Program

Chief Defence Scientist
FAS Science Policy
AS Science Corporate Management
Director General Science Policy Development
Counsellor Defence Science, London (Doc Data Sheet)
Counsellor Defence Science, Washington (Doc Data Sheet)
Scientific Adviser to MRDC Thailand (Doc Data Sheet)
Director General Scientific Advisers and Trials/Scientific Adviser Policy and
Command (shared copy)
Navy Scientific Adviser (Doc Data Sheet and distribution list only)
Scientific Adviser - Army (Doc Data Sheet and distribution list only)
Air Force Scientific Adviser
Director Trials

Aeronautical and Maritime Research Laboratory
Director

Electronics and Surveillance Research Laboratory
Director

Chief of Tactical Surveillance Systems Division
Research Leader Tactical Sensors
Head Sensor Applications
Task Manager & Author: Dr Anthony Finn (3 copies)
Author: Mark F. Knight (3 copies)
Author: Manuel Cervera (3 copies)

Chief Wide Area Surveillance Division
Head Ionospheric Effects Group
Dr Dick Thomas, WASD

Dr Micheal Evans, WSD

Mr Ralph Abbot, LSOD

DSTO Library

Library Fishermens Bend

Library Maribyrnong

Library Salisbury (2 copies)

Australian Archives

Library, MOD, Pyrmont (Doc Data sheet only)

Capability Development Division

Director General Maritime Development (Doc Data Sheet only)

Director General C3I Development (Doc Data Sheet only)

Navy

SO (Science), Director of Naval Warfare, Maritime Headquarters Annex,
Garden Island, NSW 2000. (Doc Data Sheet and distribution list only)

LCDR Andrew Williams, Directorate of Naval Warfare

MHD c/- RAN Hydrographic Office

Phillip Randall, RAN Hydrographic Office

Army

ABCA Office, G-1-34, Russell Offices, Canberra (4 copies)

SO (Science), DJFHQ(L), MILPO Enoggera, Queensland 4051 (Doc Data Sheet
only)

NAPOC QWG Engineer NBCD c/- DENGERS-A, HQ Engineer Centre Liverpool
Military Area, NSW 2174 (Doc Data Sheet only)

Air Force

Assistant Chief of the Air Staff - Materiel

Space and Joint Systems Project Manager, DESPROJ-AF

Intelligence Program

DGSTA Defence Intelligence Organisation

Corporate Support Program (libraries)

OIC TRS, Defence Regional Library, Canberra

Officer in Charge, Document Exchange Centre (DEC), 1 copy

*US Defence Technical Information Centre, 2 copies

*UK Defence Research Information Center, 2 copies

*Canada Defence Scientific Information Service, 1 copy

*NZ Defence Information Centre, 1 copy

National Library of Australia, 1 copy

UNIVERSITIES AND COLLEGES

Australian Defence Force Academy

Library

Head of Aerospace and Mechanical Engineering

Deakin University, Serials Section (M list), Deakin University Library, Geelong,
3217

Senior Librarian, Hargrave Library, Monash University

Librarian, Flinders University

OTHER ORGANISATIONS

NASA (Canberra)

AGPS

State Library of South Australia

Parliamentary Library, South Australia

OUTSIDE AUSTRALIA

ABSTRACTING AND INFORMATION ORGANISATIONS

INSPEC: Acquisitions Section Institution of Electrical Engineers

Library, Chemical Abstracts Reference Service

Engineering Societies Library, US

Materials Information, Cambridge Scientific Abstracts, US

Documents Librarian, The Center for Research Libraries, US

INFORMATION EXCHANGE AGREEMENT PARTNERS

Acquisitions Unit, Science Reference and Information Service, UK

Library - Exchange Desk, National Institute of Standards and Technology, US

National Aerospace Laboratory, Japan

National Aerospace Laboratory, Netherlands

SPARES (5 copies)

DEFENCE SCIENCE AND TECHNOLOGY ORGANISATION DOCUMENT CONTROL DATA					
				1. PRIVACY MARKING/CAVEAT (OF DOCUMENT)	
2. TITLE Ionospheric Effects on Global Positioning System Receivers			3. SECURITY CLASSIFICATION (FOR UNCLASSIFIED REPORTS THAT ARE LIMITED RELEASE USE (L) NEXT TO DOCUMENT CLASSIFICATION) Document (U) Title (U) Abstract (U)		
4. AUTHOR(S) Mark F. Knight Anthony Finn Manuel Cervera			5. CORPORATE AUTHOR Electronics and Surveillance Research Laboratory PO Box 1500 Salisbury SA 5108 Australia		
6a. DSTO NUMBER DSTO-RR-0121		6b. AR NUMBER AR-010-444		7. DOCUMENT DATE February 1998	
8. FILE NUMBER Z 7215\2\7		9. TASK NUMBER ADL 94/373 ADA 96/005		10. TASK SPONSOR DGLD DGAD	
				11. NO. OF PAGES 94	
				12. NO. OF REFERENCES 65	
13. DOWNGRADING/DELIMITING INSTRUCTIONS			14. RELEASE AUTHORITY Chief, Tactical Surveillance Systems Division		
15. SECONDARY RELEASE STATEMENT OF THIS DOCUMENT <i>Approved for public release</i>					
OVERSEAS ENQUIRIES OUTSIDE STATED LIMITATIONS SHOULD BE REFERRED THROUGH DOCUMENT EXCHANGE CENTRE, DIS NETWORK OFFICE, DEPT OF DEFENCE, CAMPBELL PARK OFFICES, CANBERRA ACT 2600					
16. DELIBERATE ANNOUNCEMENT No Limitations					
17. CASUAL ANNOUNCEMENT Yes					
18. DEFTTEST DESCRIPTORS NAVSTAR global positioning system, Global positioning system, Ionospheric disturbances, Ionospheric scintillations, Satellite navigation systems					
19. ABSTRACT This report presents the results of a study conducted under tasks ADL 94/373 and ADA 96/005 into the effects of the ionosphere on Global Positioning System (GPS) receivers. The report focuses on the effects of the disturbed ionosphere on GPS as this phenomenon has the capacity to degrade the accuracy and reliability of both civilian and military GPS receivers. The impact of ionospheric disturbances on the susceptibility of GPS in a potentially hostile electromagnetic environment is also discussed.					